

General Disclaimer

One or more of the Following Statements may affect this Document

- This document has been reproduced from the best copy furnished by the organizational source. It is being released in the interest of making available as much information as possible.
- This document may contain data, which exceeds the sheet parameters. It was furnished in this condition by the organizational source and is the best copy available.
- This document may contain tone-on-tone or color graphs, charts and/or pictures, which have been reproduced in black and white.
- This document is paginated as submitted by the original source.
- Portions of this document are not fully legible due to the historical nature of some of the material. However, it is the best reproduction available from the original submission.



NASA CR-141863
ERIM 109600-15-F

Final Report

ATMOSPHERIC EFFECTS IN MULTISPECTRAL REMOTE SENSOR DATA

ROBERT E. TURNER
Infrared and Optics Division

MAY 1975

(NASA-CR-141863) ATMOSPHERIC EFFECTS IN
MULTISPECTRAL REMOTE SENSOR DATA Final
Technical Report, 15 May 1974 - 14 Mar. 1975
(Environmental Research Inst. of Michigan)
120 p HC \$5.25 CSCL 04A

N75-26474

Unclassified
26647

CSCL 04A G3/4

Prepared for
NATIONAL AERONAUTICS AND SPACE ADMINISTRATION

Johnson Space Center
Earth Observations Division
Houston, Texas 77058
Contract No. NAS9-14123, Task VIII
Technical Monitor: Dr. A. Potter/TF3



**ENVIRONMENTAL
RESEARCH INSTITUTE OF MICHIGAN**

TECHNICAL REPORT STANDARD TITLE PAGE

1. Report No. NASA CR-ERIM 109600-15-F	2. Government Accession No.	3. Recipient's Catalog No.	
4. Title and Subtitle ATMOSPHERIC EFFECTS IN MULTISPECTRAL REMOTE SENSOR DATA		5. Report Date May . 1975	
		6. Performing Organization Code	
7. Author(s) Robert E. Turner		8. Performing Organization Report No. 109600-15-F	
9. Performing Organization Name and Address Environmental Research Institute of Michigan Infrared and Optics Division P.O. Box 618 Ann Arbor, Michigan 48107		10. Work Unit No. Task VIII	
		11. Contract or Grant No. NAS9-14123	
12. Sponsoring Agency Name and Address National Aeronautics and Space Administration Johnson Space Center Earth Observations Division Houston, Texas 77058		13. Type of Report and Period Covered Final Technical Report 15 May 1974 - 14 March 1975	
		14. Sponsoring Agency Code	
15. Supplementary Notes Dr. Andrew Potter/TF3 is Technical Monitor for NASA.			
16. Abstract The atmosphere can play an important role in diminishing the classification accuracy in multispectral remote sensing. There are several atmospheric effects which must be considered in a complete analysis of the classification problem.. This report treats the problem of radiometric variations as a result of a change in geometric and environmental factors. First, the case of spatially varying atmospheres is considered, and second, the effect of background on target via atmospheric scattering is analyzed for realistic conditions. Emphasis is placed upon a simulation of LANDSAT spectral data for agricultural investigations over the United States. The effect of the target-background interaction is thoroughly analyzed in terms of various atmospheric states, geometric parameters, and target-background materials. Results clearly demonstrate that variable atmospheres can alter the classification accuracy and that the presence of various backgrounds can change the effective target radiance by a significant amount. A failure to include these effects in multispectral data analysis will result in a decrease in the classification accuracy.			
17. Key Words Aerosol Scattering Radiative Transfer Classification Accuracy Variable Atmospheres Remote Sensing		18. Distribution Statement Initial distribution is listed at the end of this document.	
19. Security Classif. (of this report) Unclassified	20. Security Classif. (of this page) Unclassified	21. No. of Pages 120	22. Price

PREFACE

This report describes part of a continuing research program in remote sensing of the environment. The research is being conducted for NASA's Lyndon B. Johnson Space Center, Houston, Texas, by the Environmental Research Institute of Michigan (ERIM), formerly the Willow Run Laboratories, Institute of Science and Technology, The University of Michigan. The main objective of this program is to develop remote sensing as a practical tool for obtaining extensive environmental information quickly and economically.

Remote sensing of the environment involves the transfer of radiation from a target on the Earth's surface through the atmosphere to a sensor located at a point either within or above the atmosphere. The atmospheric medium can alter the radiation by absorption and scattering. In this report we examine the effects due to the spatial variation of the atmosphere and also due to influence of background on target as a result of scattering. Results are presented in terms of classification accuracy for variable atmospheres and in terms of percent change in target radiance for the target-background interaction problem.

The research described in this report was performed under Contract NAS9-14123, Task VIII, and covers the period from 15 May 1974 through 14 March 1975. Dr. Andrew Potter served as Technical Monitor. The program was directed by R. R. Legault, Vice President of ERIM, J. D. Erickson, Head of ERIM's Information Systems and Analysis Department, and R. F. Nalepka, Principal Investigator and Head of ERIM's Multispectral Analysis Section. The ERIM number of this report is 109600-15-F.

The author wishes to acknowledge the direction provided by R. R. Legault and J. D. Erickson. Helpful suggestions by R. F. Nalepka were also appreciated. The extensive amount of computer programming was done by P. F. Lambeck and L. R. Ziegler. The author also thanks D. Dickerson and L. Parker for their secretarial assistance in the preparation of this report.

CONTENTS

PREFACE	2
FIGURES	5
TABLES	9
1. SUMMARY	10
2. INTRODUCTION.	12
3. VARIABLE ATMOSPHERES.	15
3.1 Optical Parameters	
3.1.1 Attenuation Coefficients	
3.1.2 Optical Depth	
3.1.3 Scattering Phase Functions	
3.2 Radiometric Quantities	
3.3 Correction Algorithm	
3.4 Variation of Parameters	
3.5 Classification Accuracy	
4. TARGET-BACKGROUND INTERACTION	67
4.1 The General Equation	
4.2 Multi-Dimensional Radiative Transfer	
4.2.1 The Transfer Equation	
4.2.2 General Solution	
4.2.3 Green's Function	
4.2.4 Single Scattering	
4.2.5 Surface Path Radiance	
4.3 Simulation of Satellite Data	
4.3.1 Reflectance Patterns	
4.3.2 Simulation of ERTS Data	
5. INTERACTION CORRECTION ALGORITHM.	102
5.1 General Surfaces	
5.2 Lambertian Surfaces	
6. CONCLUSIONS AND RECOMMENDATIONS	107
REFERENCES.	111
DISTRIBUTION LIST	112

FIGURES

1. Variation of Visual Range With Extinction Coefficient	17
2. ERIM Radiative Transfer Model	22
3. Dependence of Direct Solar and Diffuse Downward Irradiance on Optical Thickness and Surface Albedo	24
4. Dependence of Diffuse Downward Irradiance on Surface Albedo for Optically Thin and Thick Atmospheres	25
5. Total Downward Irradiance as a Function of Transmittance for Various Surfaces	26
6. Dependence of Path Radiance on Total Irradiance for Various Transmittances and Surface Albedos	27
7. Visual Range Vs. Transmittance for Four Wavelengths	29
8. Dependence of Total Spectral Radiance on Target Reflectance and Optical Thickness for a Background Albedo of 0.4	30
9. Dependence of Total Spectral Radiance on Surface Albedo and Optical Thickness for a Target Reflectance of 0.2	31
10. Dependence of Total Radiance on Total Irradiance for Various Transmittances and Surface Albedos	32
11. Dependence of Total Radiance on Path Radiance for Various Transmittances and Surface Albedos	34
12. Optical Thickness Experimental Array	38
13. Histograms of L_I (Calculated) / L_I (Actual) For a "Symmetric" Atmosphere With a Visual Range of 10 km	40
14. Histograms of L_I (Calculated) / L_I (Actual) For a "Symmetric" Atmosphere With a Visual Range of 10 km	41
15a. Actual Radiance Surface for "Symmetric" Atmosphere	42
15b. Optical Thickness Surface for "Symmetric" Atmosphere	42
16a. Ratio Surface for "Symmetric" Atmosphere With One Sensor	43
16b. Ratio Surface for "Symmetric" Atmosphere With Nine Sensors	43
17a. Ratio Surface for "Symmetric" Atmosphere With Five Sensors	44

FIGURES (Cont'd)

17b. Ratio Surface for "Symmetric" Atmosphere With Five Sensors.	44
18. Ratio Surface for "Symmetric" Atmosphere With 25 Sensors.	45
19. Histograms of L_I (Calculated)/ L_I (Actual) For a "Symmetric" Atmosphere With a Visual Range of 23 km	47
20. Histograms of L_I (Calculated)/ L_I (Actual) For a "Symmetric" Atmosphere.	48
21a. Actual Radiance Surface For "Asymmetric" Atmosphere	49
21b. Optical Thickness Surface For "Asymmetric" Atmosphere	49
22. Histograms of L_I (Calculated)/ L_I (Actual) For an "Asymmetric" Atmosphere.	50
23. Histograms of L_I (Calculated)/ L_I (Actual) For an "Asymmetric" Atmosphere.	51
24. Histograms of L_I (Calculated)/ L_I (Actual) For an "Asymmetric" Atmosphere.	52
25. Histograms of L_I (Calculated)/ L_I (Actual) For an "Asymmetric" Atmosphere.	53
26a. Ratio Surface for "Asymmetric" Atmosphere With One Sensor	54
26b. Ratio Surface for "Asymmetric" Atmosphere With Nine Sensors	54
27a. Ratio Surface for "Asymmetric" Surface With Five Sensors.	55
27b. Ratio Surface for "Asymmetric" Surface With Five Sensors.	55
28. Ratio Surface for "Asymmetric" Surface With 25 Sensors.	56
29. Pattern of Simulated Corn and Soybean Fields, Case 1.	60
30. Pattern of Simulated Corn and Soybean Fields, Case 2a	62
31. Pattern of Simulated Corn and Soybean Fields, Case 2b	63
32. Pattern of Simulated Corn and Soybean Fields, Case 3a	64
33. Pattern of Simulated Corn and Soybean Fields, Case 3b	65

FIGURES (Cont'd)

34. Number of Fields Versus Classification Accuracy.	66
35. Radiance Components in a Scattering Atmosphere	68
36. Geometry for Singly Scattered Surface Radiation.	75
37. Radiance Components for a Finite Aperture.	77
38. Variation of Single Scattering Integrand With Distance from Point of View.	79
39. Fraction of the Surface Path Radiance as a Function of Distance from Origin for a Uniform Surface Reflectance.	80
40. Angular Dependence of Single-Scattering Phase Functions in Any Azimuthal Plane.	81
41. Field Configuration 1.	85
42. Field Configuration 2.	86
43. Ratio of Surface Path Radiance to Atmospheric Path Radiance as a Function of a Variable Black-White Background and a Black Target . .	87
44. Ratio of Surface Path Radiance to Atmospheric Path Radiance as a Function of Wavelength for a Variable Black-White Background and a Black Target	88
45. Total Spectral Radiance as a Function of a Variable Wheat-Grass Background for a Wheat Target and a Grass Target	90
46. Variation of Wheat Radiance for a Black, Wheat, and Grass Back- ground	91
47. Per Cent Change in Total Radiance for a Wheat Target Surrounded by Rings of Wheat and Grass.	92
48. Per Cent Change in Radiance Between a Wheat Field Surrounded by Grass and an All Wheat Area for Four Solar Zenith Angles	94
49. Total Radiance Vs. Surface Path Radiance for Wheat-Wheat to Wheat-Grass Transition	95
50. Change in Loam Radiance Caused by Surrounding Grass.	96

FIGURES (Cont'd)

TABLES

1. Parameters for Multi-Gaussian Optical Thickness Surface. 38

1

SUMMARY

There has been a continuing question in multispectral remote sensing data analysis as to the extent that the atmosphere affects the classification of various materials on the Earth's surface. In previous studies we have developed a radiative-transfer model and have used that model to examine the variation in simulated multispectral data. The model was a simplified yet practical model which included the effects of absorptive and non-absorptive haze conditions. The main limitation of the model, as far as remote sensing data analysis is concerned, was its one-dimensional nature, i.e., no spatial variations in the horizontal plane were considered.

In the present treatment we have extended the model to include non-uniform atmospheres and have examined the influence of the resulting changes in radiance on the accuracy of classification of various classes of objects. Various atmospheric gradients of optical thickness were considered throughout a LANDSAT frame and fields were produced artificially by random sampling from real data. Classification accuracy was then determined for each field and analyzed as a function of visual range. The results indicate that as the visual range atmospheric gradient increases the classification accuracy decreases. An atmospheric correction algorithm is also presented which can be used to eliminate the systematic variations attributable to the atmosphere.

Potentially, a more important effect is the influence of background materials on the target as a result of atmospheric scattering. In particular,

we would like to know what effect the proximity of various background elements has on the spectral character of the target. If there is a strong influence, then the probability of misclassification could increase significantly. A detailed three-dimensional treatment of this problem has been carried out and the influence of background on target has been analyzed for various environmental conditions. In particular, we found that for dark targets and bright backgrounds the per cent change in the target radiance can be quite large, i.e., 50-70%. We also examined this effect in terms of sun angle and visibility and found that the maximum variability occurs in the normal range of operational parameters. The gradual change in target radiance is given in terms of varying amounts of background material, thus simulating a variety of possible geometric background field configurations. An algorithm which can be used to remove this effect from actual multispectral data is also described.

INTRODUCTION

In remote sensing of features on Earth's surface the main purpose of multispectral data analysis is to discriminate among various materials and to recognize classes of objects. There are many effects which must be included in such investigations. There is never a 100 per cent classification because of various noise factors in the system. Some of these factors are: intrinsic variations within a class at a particular time, such as the natural variability in a wheat field at a particular point in the growing season; mixtures of various materials in the same area; intrinsic temporal variations of a material; intrinsic goniometric properties; climatic and weather changes; atmospheric effects; and detector noise. Many of these effects can be dealt with in a statistical manner, and using statistical decision theory one can arrive at a signature or class identification.

The remote sensing of terrain features means that we are necessarily receiving radiation which has passed through part or all of the Earth's atmosphere. As a result, it has long been suspected that the atmosphere can cause significant changes in signatures and thereby reduce the accuracy of classification. In the current investigation, we shall consider primarily two atmospheric effects; changes in classification accuracy for spatially varying atmospheres, and the target-background interaction, i.e., the influence of background elements on the target as a result of atmospheric scattering.

A rigorous mathematical treatment of radiative-transfer in a spatially varying atmosphere is an intriguing but extremely difficult problem. Nevertheless, under certain circumstances, simplifying assumptions can be made and a reasonably accurate practical solution can be found. In this study we shall analyze various atmospheric conditions using a simplified radiative-transfer model to simulate multispectral data for different classes of materials. We can then vary the atmospheric state and see what the resulting change is in the classification accuracy.

It turns out that the second atmospheric effect, i.e., the target-background interaction is in many cases more important as far as changes in spectral radiances are concerned, than variable atmospheres. We want to know for example, the change in spectral radiance for a target surrounded by various patterns of background materials. Also, we want to know under what conditions this effect is most important.

In the mathematical derivations of the basic equations very few approximations are made. The most important ones are: 1) a uniform atmosphere, and 2) single scattering. Multiple scattering is included in the determination of "pure" atmospheric path radiance and in the downward diffuse irradiance. A somewhat rigorous treatment is necessary because we do not want to introduce anomalous mathematical uncertainties. We do want whatever variations occur to reflect intrinsic changes in the environmental conditions and not be the result of mathematical approximations. In the actual analysis we have made other assumptions however, in order to simplify the computational analysis. For example, we assume a checkerboard pattern of uniform square fields each being a Lambert reflector. The general mathematical model, however, is capable of using any complex pattern and a surface with any goniometric property.

A further question arises; can we develop an algorithm so as to remove this effect from real data? The answer is yes, providing that we have some knowledge of the atmosphere and the surface pattern of fields. In the last section we devise an algorithm which can be used in the analysis of actual multispectral data.

Having solved these problems it would now be appropriate to consider both the variable atmospheric state and the interaction problem simultaneously in order to determine classification accuracy.

VARIABLE ATMOSPHERES

In this section we shall examine the variation of radiometric quantities in terms of the parameters used in the radiative-transfer model. Making use of these parameters we will then construct hypothetical variable atmospheric states for which we will implement the atmospheric correction algorithm. The percent classification will be calculated for the various atmospheric conditions.

3.1 OPTICAL PARAMETERS

In order to construct variable atmospheres we will first define the basic optical parameters which are used in the radiative-transfer model.

3.1.1 ATTENUATION COEFFICIENTS

The attenuation of a collimated beam of radiation is expressed by the following equation:

$$I_\lambda(x) = I_\lambda(0) e^{-K_\lambda x} \quad (1)$$

when $I_\lambda(x)$ and $I_\lambda(0)$ are the spectral intensities of the beam at distance x and at the origin respectively and K_λ is called the spectral extinction coefficient. This is a measure of the total removal of radiation from the initial beam as a result of both scattering and absorption in the medium.

In 1924, Koschmieder [1] defined a distance (visual range) such that the limiting contrast between an object and its background (pure atmosphere) is 0.02. This definition provides us with the following useful formula which relates

[1] H. Koschmieder, Beitr. Phys. freien Atm., Vol. 12, 19,24 pp. 33-53, 171-181.

visual range to the volume extinction coefficient at a wavelength of 0.55 μm :

$$V(\text{km}) = \frac{3.912}{\kappa_{\lambda_0} (\text{km}^{-1})} \quad (2)$$

where $\lambda_0 = 0.55$. This relationship holds over a wide range of distances and is illustrated in Fig. 1.

For realistic atmospheres we must consider not only the gaseous component but also the semi-permanent suspension of particulates, referred to as the aerosol component. Thus, we have

$$\kappa_{\lambda}(z) = \kappa_{\lambda}^R(z) + \kappa_{\lambda}^A(z) \quad (3)$$

where $\kappa_{\lambda}^R(z)$ is the well-known Rayleigh coefficient at altitude z and $\kappa_{\lambda}^A(z)$ is the corresponding aerosol coefficient. Besides the volume extinction coefficients we also have volume absorption and volume scattering coefficients, i.e.,

$$\kappa_{\lambda}(z) = \alpha_{\lambda}(z) + \beta_{\lambda}(z) \quad (4)$$

where the absorption coefficient $\alpha_{\lambda}(z)$ and the scattering coefficient $\beta_{\lambda}(z)$ for the gaseous component is known by experiment and the corresponding aerosol coefficients are determined by Mie theory, i.e.,

$$\alpha_{\lambda}^A(z) = \int_0^{\infty} n(r, z) \sigma_{\lambda}^a(r) dr \quad (5)$$

and

$$\beta_{\lambda}^A(z) = \int_0^{\infty} n(r, z) \sigma_{\lambda}^s(r) dr \quad (6)$$

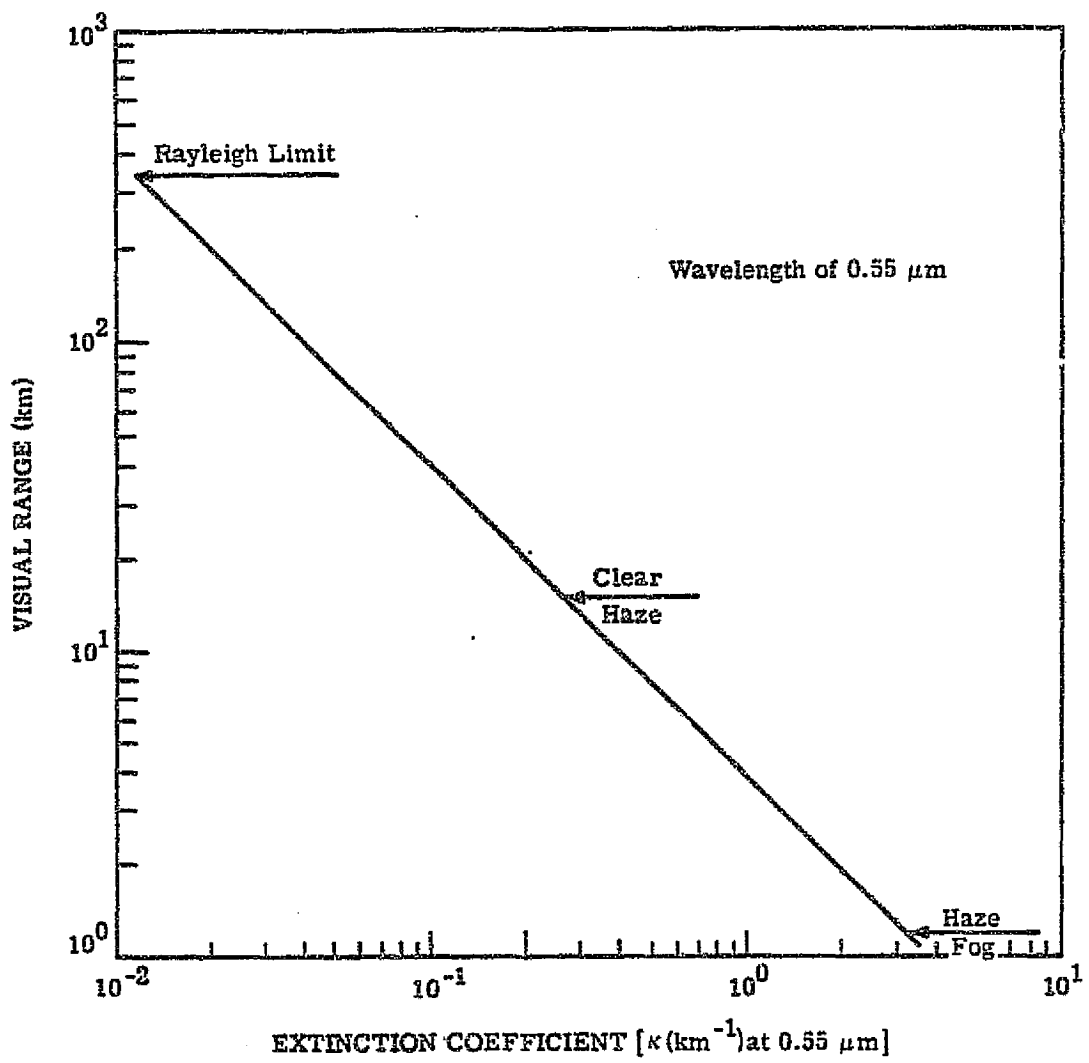


FIGURE 1. VARIATION OF VISUAL RANGE WITH EXTINCTION COEFFICIENT

where $n(r,z)$ is the particle size distribution function for particles of radius r and $\sigma_{\lambda}^a(r)$ and $\sigma_{\lambda}^s(r)$ are the absorption and scattering cross sections for uniform spherical particles. Details of the properties of these coefficients were determined for realistic atmospheres by Turner [2].

3.1.2 OPTICAL DEPTH

A more convenient parameter to use in radiative-transfer theory than the attenuation coefficient is the optical depth τ . This is a dimensionless quantity which is a measure of the turbidity of the atmosphere. Mathematically, it is expressed as follows:

$$\tau_{\lambda} = \int_h^{\infty} \kappa_{\lambda}(z) dz \quad (7)$$

where τ_{λ} is the spectral optical depth at altitude h . Using this definition, the optical depth of the entire atmosphere, called the optical thickness $\tau_{0\lambda}$, is given by

$$\tau_{0\lambda} = \int_0^{\infty} \kappa_{\lambda}(z) dz \quad (8)$$

Typical values of $\tau_{0\lambda}$ in the visible part of the electromagnetic spectrum range from ~ 0.03 for clear atmospheres to ~ 3 for very hazy atmospheres.

From a practical standpoint, the spectral optical thickness $\tau_{0\lambda}$ is an easily measurable quantity. Using a spectrometer or some multispectral radiometric device one can measure the spectral irradiance of the direct sunlight, $E_d(\lambda)$ for a specific solar zenith angle θ_o ($=\cos^{-1}\mu_o$) and determine

[2] R. E. Turner, Radiative Transfer in Real Atmospheres, Report No. 190100-24-T, Environmental Research Institute of Michigan, Ann Arbor, 1974.

the optical thickness from the following formula:

$$\tau_{o\lambda} = \mu_o \ln \frac{\mu_o E_o(\lambda)}{E_d(\lambda)} \quad (9)$$

where $E_o(\lambda)$ is the known extraterrestrial value of the solar irradiance.

Making use of data obtained from light scattering experiments in the atmosphere, Elterman [3] constructed model atmospheres for various hazes. His data relate the optical depth for any altitude to the wavelength and visibility.

3.1.3 SCATTERING PHASE FUNCTIONS

Another quantity of importance in radiative-transfer analysis is the single-scattering phase function $\beta_\lambda(r, \theta, \phi)$. It describes the angular scattering characteristics of a particle of radius r and can be thought of as a probability density. It is normalized such that the integral of the phase function over all angles is unity, i.e.,

$$\frac{1}{4\pi} \int_0^{2\pi} \int_{-1}^1 \beta_\lambda(r, \theta, \phi) d(\cos\theta) d\phi = 1 \quad (10)$$

For particles which are small as compared to the wavelength of the incident radiation the angular variation in $\beta_\lambda(r, \theta, \phi)$ is almost like that for dipole scattering, i.e., $\sim 1 + \cos^2\chi$, where χ is the scattering angle. For large particles, however, the scattering is predominantly in the forward direction. Deirmendjian [4] has calculated the phase function integrated over various particle size distribution in order to obtain the so-called polydisperse

[3] L. Elterman, Vertical-Attenuation Model with Eight Surface Meteorological Ranges 2 to 13 Kilometers, Report No. AFCRL-70-0200, Air Force Cambridge Research Laboratories, Office of Aerospace Research, Bedford, Mass., 1970.

[4] D. Deirmendjian, Electromagnetic Scattering on Spherical Polydispersions, Elsevier, New York, 1969, p. 78.

scattering phase function. We have also run computer programs to determine the scattering phase functions and attenuation coefficients for various atmospheric states characterized by particle sizes and compositions. A detailed treatment of these optical parameters is beyond the scope of this report, but can be found in the author's previous report [2].

3.2 RADIOMETRIC QUANTITIES

The general solution of the radiative-transfer equation is the following:

$$L = L_o T + L_p \quad (11)$$

where L_o is the spectral radiance at the surface, T is the spectral transmittance from the surface to the sensor, and L_p is the spectral path radiance, i.e., that radiance which results from all multiply-scattered radiation along the path from the target to the sensor. The radiative-transfer model developed at ERIM allows one to calculate all of the quantities in Eq. (11) for various values of the independent variables on which the radiometric quantities depend. The explicit dependence is as follows:

$$L = L(\lambda, \tau_o, z, \theta, \phi, \theta_o, \rho, \bar{\rho}) \quad (12)$$

$$L_o = L_o(\lambda, \tau_o, \theta, \phi, \theta_o, \rho, \bar{\rho}) \quad (13)$$

$$T = T(\lambda, \tau_o, z, \theta) \quad (14)$$

$$L_p = L_p(\lambda, \tau_o, z, \theta, \phi, \theta_o, \rho, \bar{\rho}) \quad (15)$$

[2] R. E. Turner, Radiative Transfer in Real Atmospheres, Report No. 190100-24-T, Environmental Research Institute of Michigan, Ann Arbor, 1974.

where λ is the wavelength, τ_o the optical thickness, θ the nadir view angle, ϕ the azimuthal angle between the view plane and solar plane, θ_o the solar zenith angle, z the altitude of the sensor, ρ the target reflectance, and $\bar{\rho}$ the background albedo. In addition, for the case of perfectly diffuse (Lambertian) surfaces the surface radiance is given by

$$L_o = \frac{\rho}{\pi} E \quad (16)$$

where

$$E = E(\lambda, \tau_o, \theta_o, \rho, \bar{\rho}) \quad (17)$$

is the total downward spectral irradiance on the target. By specifying various input parameters the radiometric quantities can be calculated.

Figure 2 illustrates the input-output characteristics of the basic radiative-transfer model developed at ERIM.

Of all radiometric quantities the easiest to measure is probably the direct solar irradiance. This measurement gives us the optical thickness of the atmosphere, which in turn allows us to calculate the transmittance, i.e.,

$$T_o = e^{-\tau_o}$$

where T_o is the vertical transmittance of the entire atmosphere. The path radiance is usually more difficult to measure accurately. The ideal way to determine it is to measure the radiance of an absolutely black infinitesimal target. Then, since the reflectance ρ is zero, we have, according to Eq. (11)

$$L = L_p \quad (18)$$

Although there do exist surface materials which have very low reflectances, there is still some significant amount of radiation from the target.

In order to understand the relationship of these various quantities we shall plot a series of graphs.

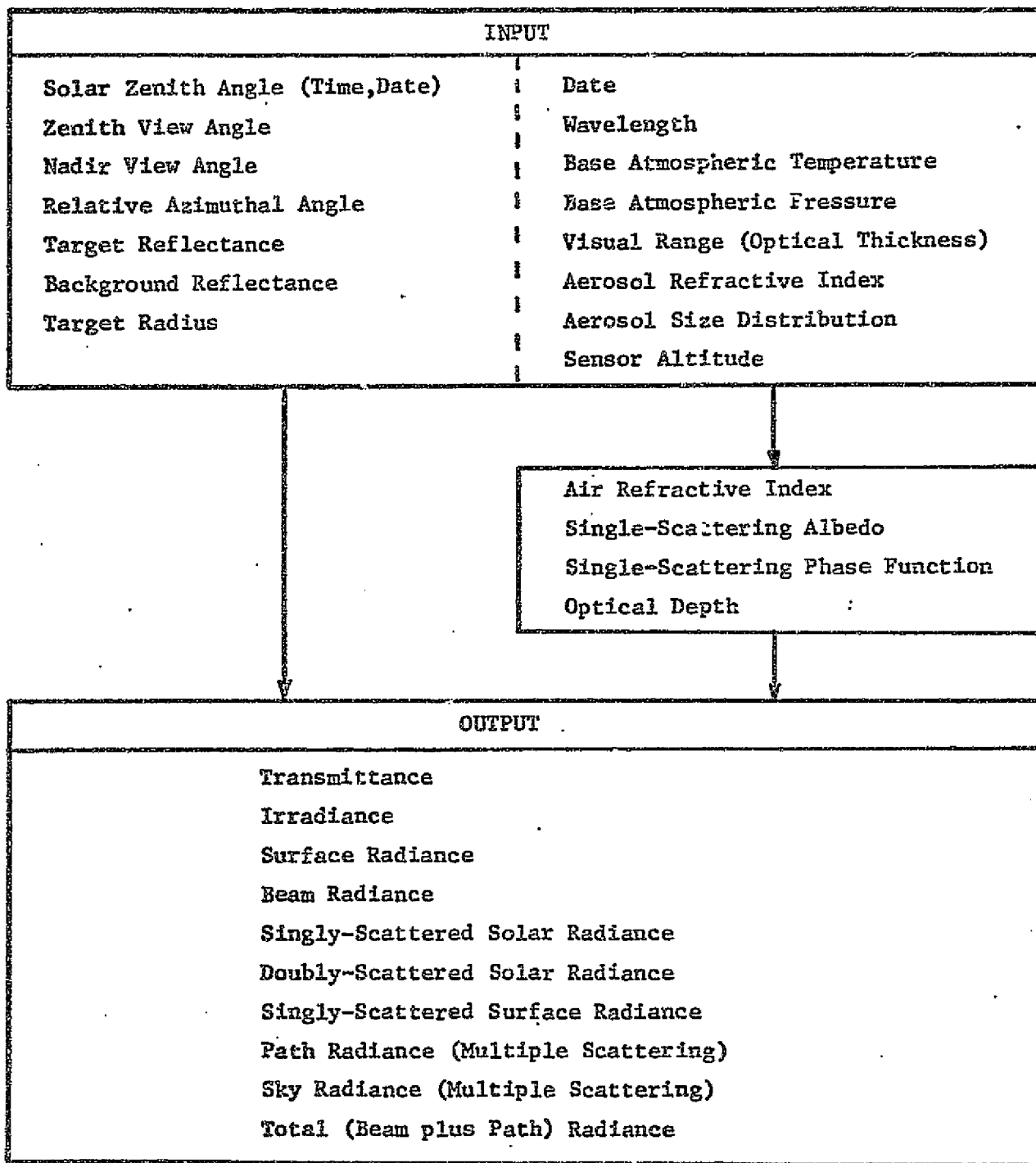


FIGURE 2. ERIM RADIATIVE TRANSFER MODEL

Figure 3 illustrates the radiation of the direct solar and downward diffuse irradiances as a function of the atmospheric optical thickness and surface albedo. The direct irradiance decreases exponentially and is independent of surface conditions since it just represents the amount of radiation which is not lost from the solar input. For an optical thickness of zero (no atmosphere) there is, by definition, no diffuse component, but as τ_0 increases, some of the energy lost by the direct beam goes into the diffuse downward component. It is interesting to note, however, that a white surface only raises the diffuse downward irradiance by about 30% over that for a black surface in the case of a thick atmosphere. For a thin atmosphere, however, the white surface produces an irradiance almost three times that for a black surface. This effect is illustrated in Fig. 4. The physical principles can be understood better by looking at the total downward irradiance as a function of transmittance T_0 . This variation is depicted in Fig. 5. For darker surfaces the irradiance decreases with increasing turbidity because less radiation is able to reach the surface. On the other hand, for brighter surfaces, more radiation is reflected and is essentially trapped under the ever thickening turbid atmosphere.

All of the radiometric quantities are interrelated, sometimes in a rather complicated way. Figure 6 illustrates the dependence of both radiance on irradiance for various transmittances and surface albedos. It is interesting to note that both of these quantities depend upon surface albedo linearly. Also, for larger values of transmittance we see a very large change in path radiance but a corresponding very small change in irradiance.

FIGURE 3

Dependence of Direct Solar and Diffuse Downward Irradiance on Optical Thickness and Surface Albedo. Wavelength = 0.55 μm , Solar Zenith Angle = 0°.

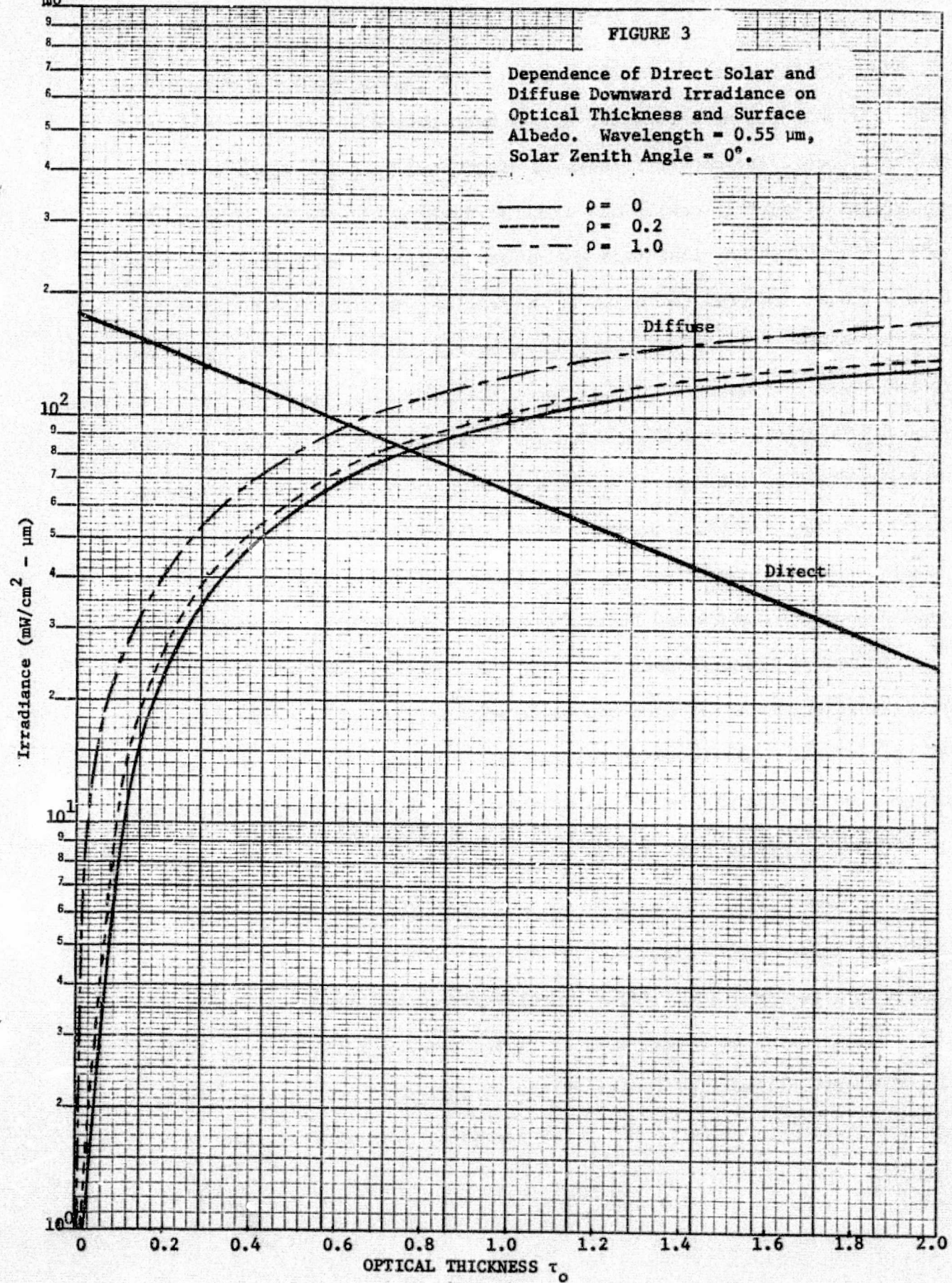
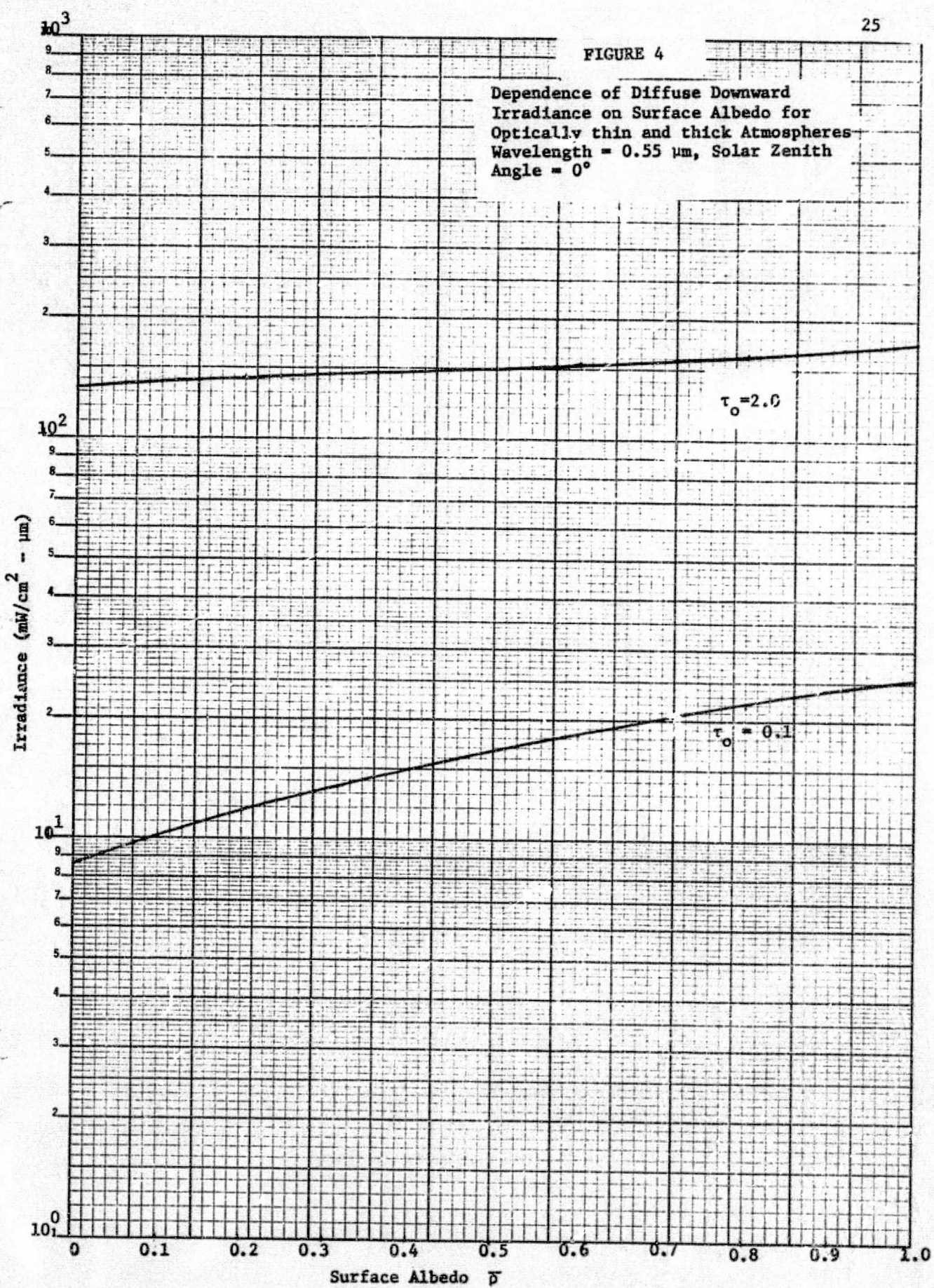


FIGURE 4

Dependence of Diffuse Downward Irradiance on Surface Albedo for Optically thin and thick Atmospheres
 Wavelength = $0.55 \mu\text{m}$, Solar Zenith Angle = 0°



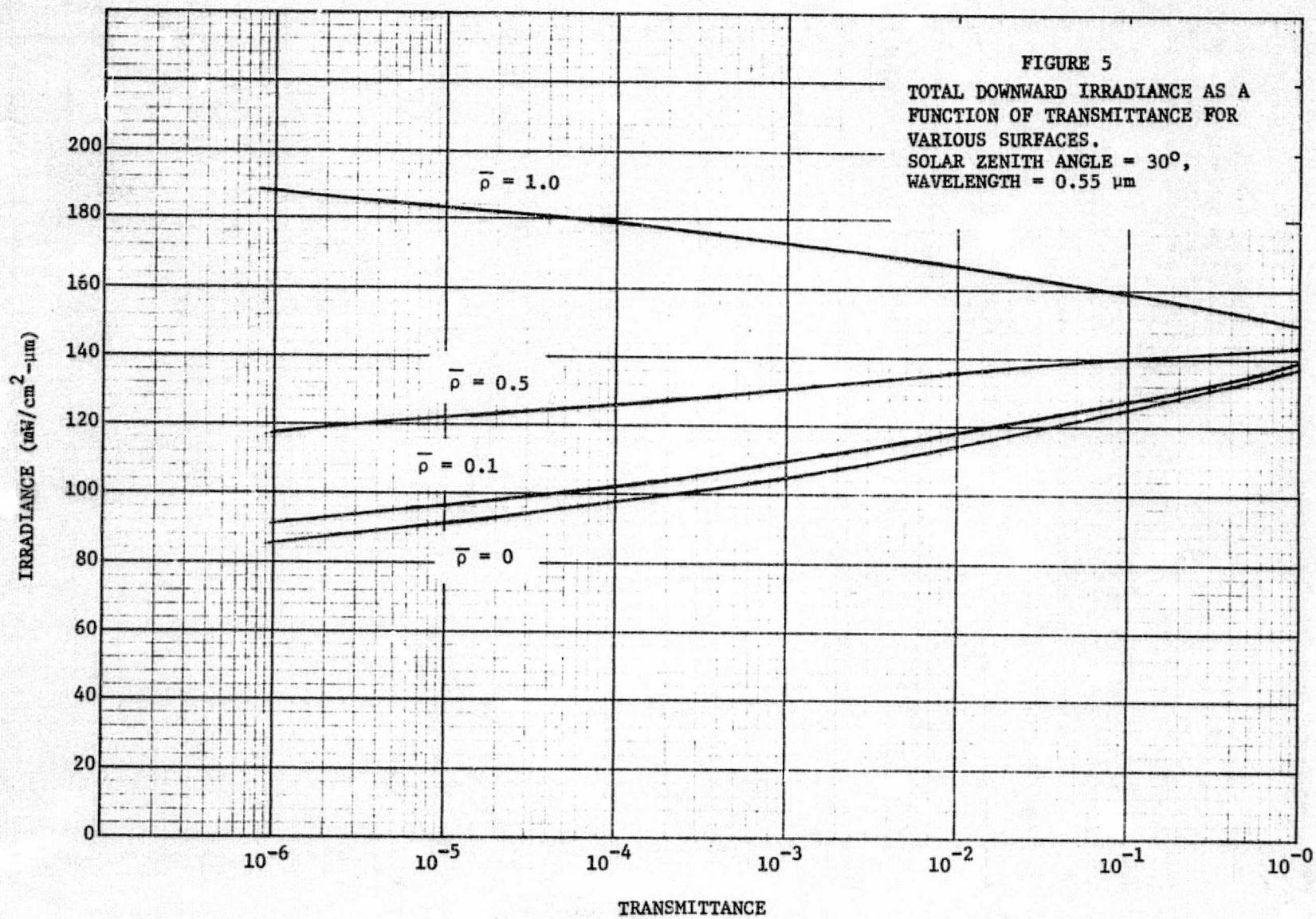
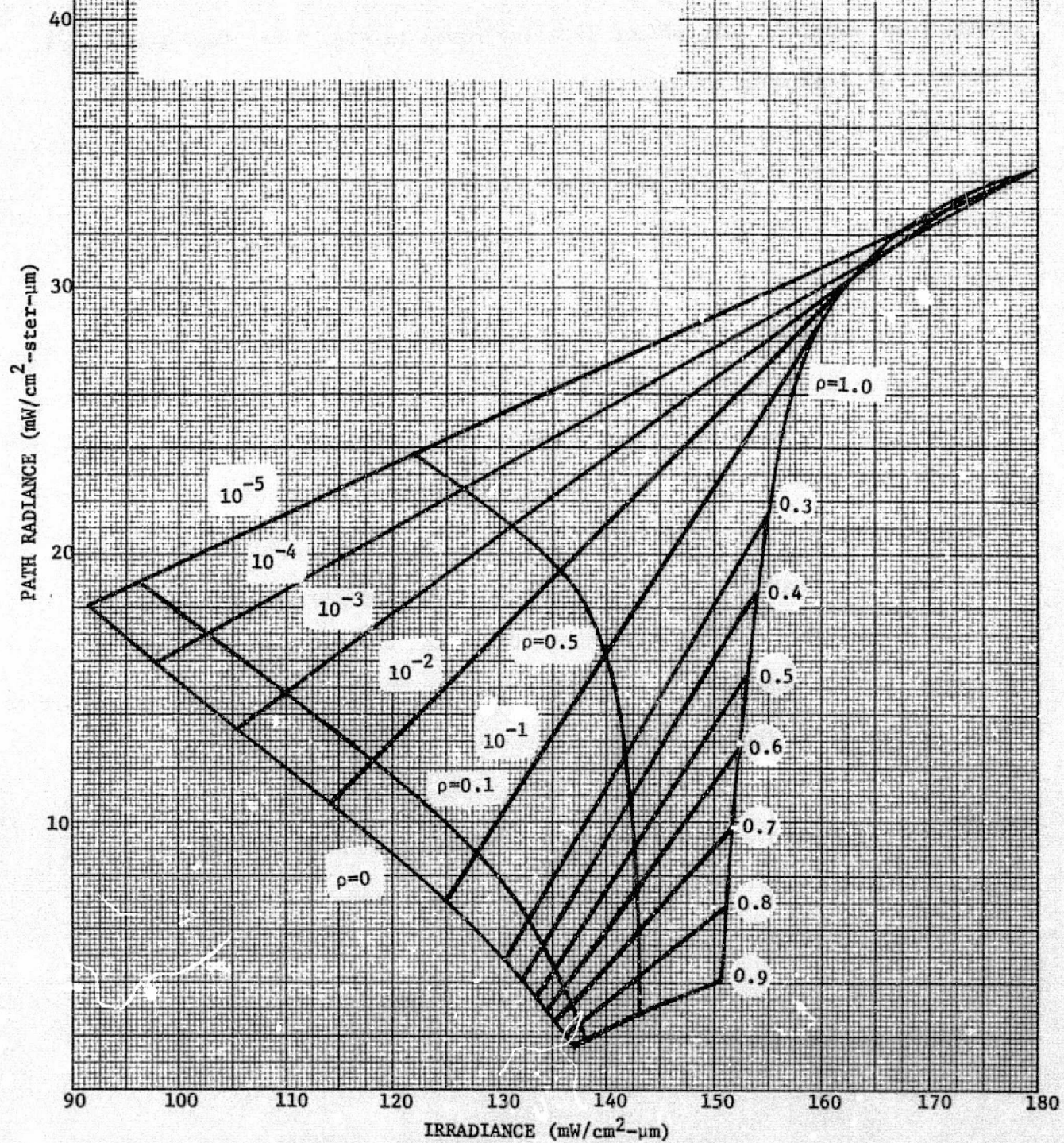


FIGURE 6

DEPENDENCE OF PATH RADIANCE ON TOTAL IRRADIANCE FOR VARIOUS TRANSMITTANCES AND SURFACE ALBEDOS. SOLAR ZENITH ANGLE = 30° , NADIR VIEW ANGLE = 0° , WAVELENGTH = $0.55 \mu\text{m}$



For practical cases of transmittances which are usually encountered we can relate them to visual ranges. This is shown in Fig. 7.

We should now examine the total radiance. If we let the background albedo be held constant and vary the target reflectance, then the total radiance increases in a linear way as depicted in Fig. 8. Likewise, holding the target reflectance constant, we can see the effect of a variation in the background albedo. This effect is illustrated in Fig. 9 for four atmospheric states. It should be noted from both of these graphs that there exists a wide range of atmospheric states and a very small range of reflectances which can give approximately the same total radiance, i.e., given a certain reflectance, we can have almost any atmospheric state and the total radiance remains the same.

We can examine the dependence of total radiance on the irradiance. This relationship is illustrated in Fig. 10. The dependence of each on reflectance is linear but for specific transmittances the dependence is definitely non-linear. For example, for a surface with a reflectance of 50% the radiance decreases with increasing transmittance up to a point, but then the radiance increases rapidly with a small increase in transmittance. If, however, the surface reflectance is very high, say 100%, then the radiance increases as the transmittance increases. These effects are due to the fact that darker surfaces will get darker as the haze decreases but brighter surfaces will get even brighter. It should also be noted that if the total radiance is measured from a sensor aboard a satellite and the transmittance is determined, then a unique value for the reflectance exists. This is true however, only for $\rho = \bar{\rho}$. Nevertheless, the same procedure can be followed for more general conditions in which $\rho \neq \bar{\rho}$. It is a mathematically well-determined problem since the irradiance is also a measurable quantity.

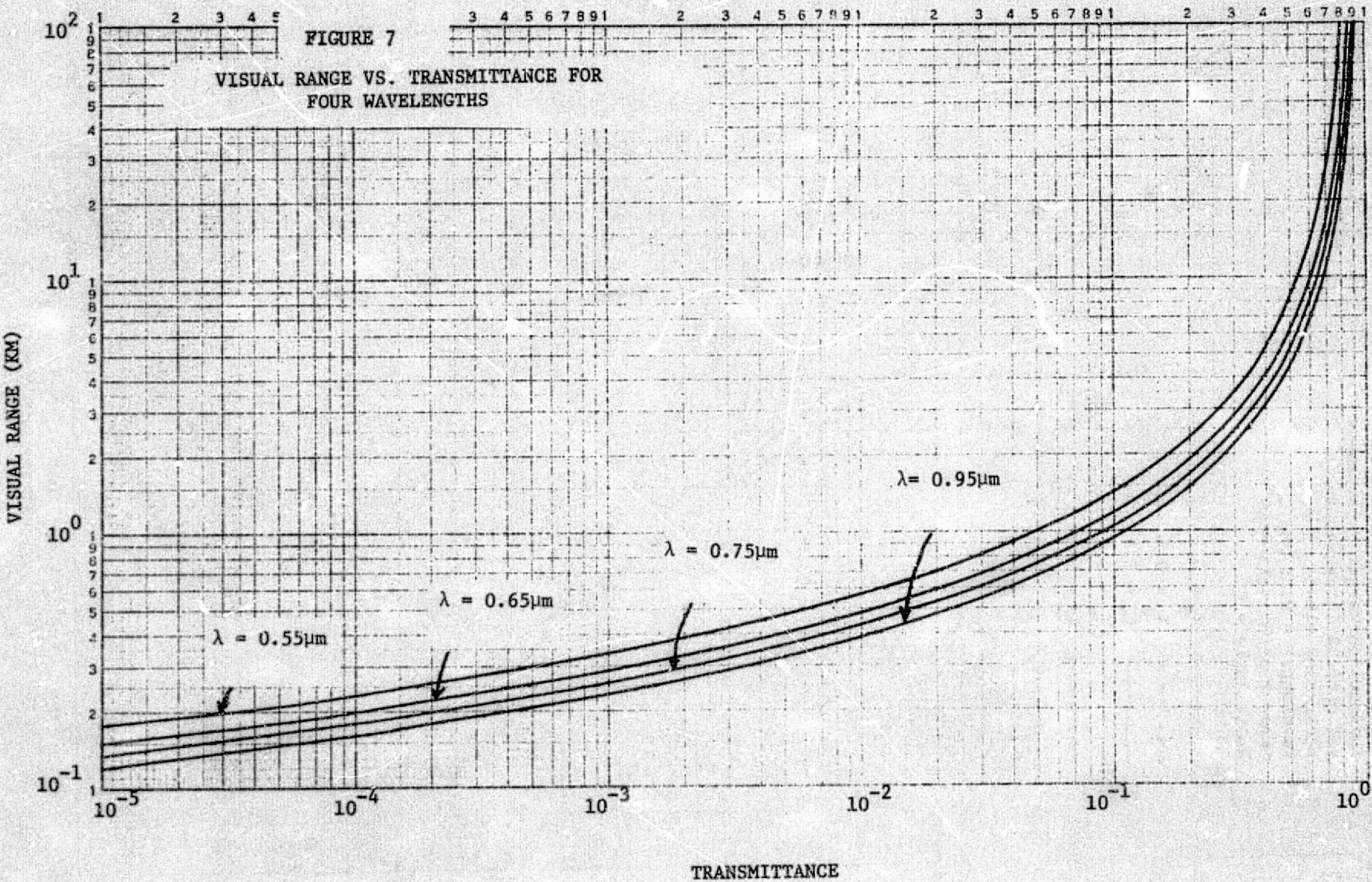


FIGURE 8

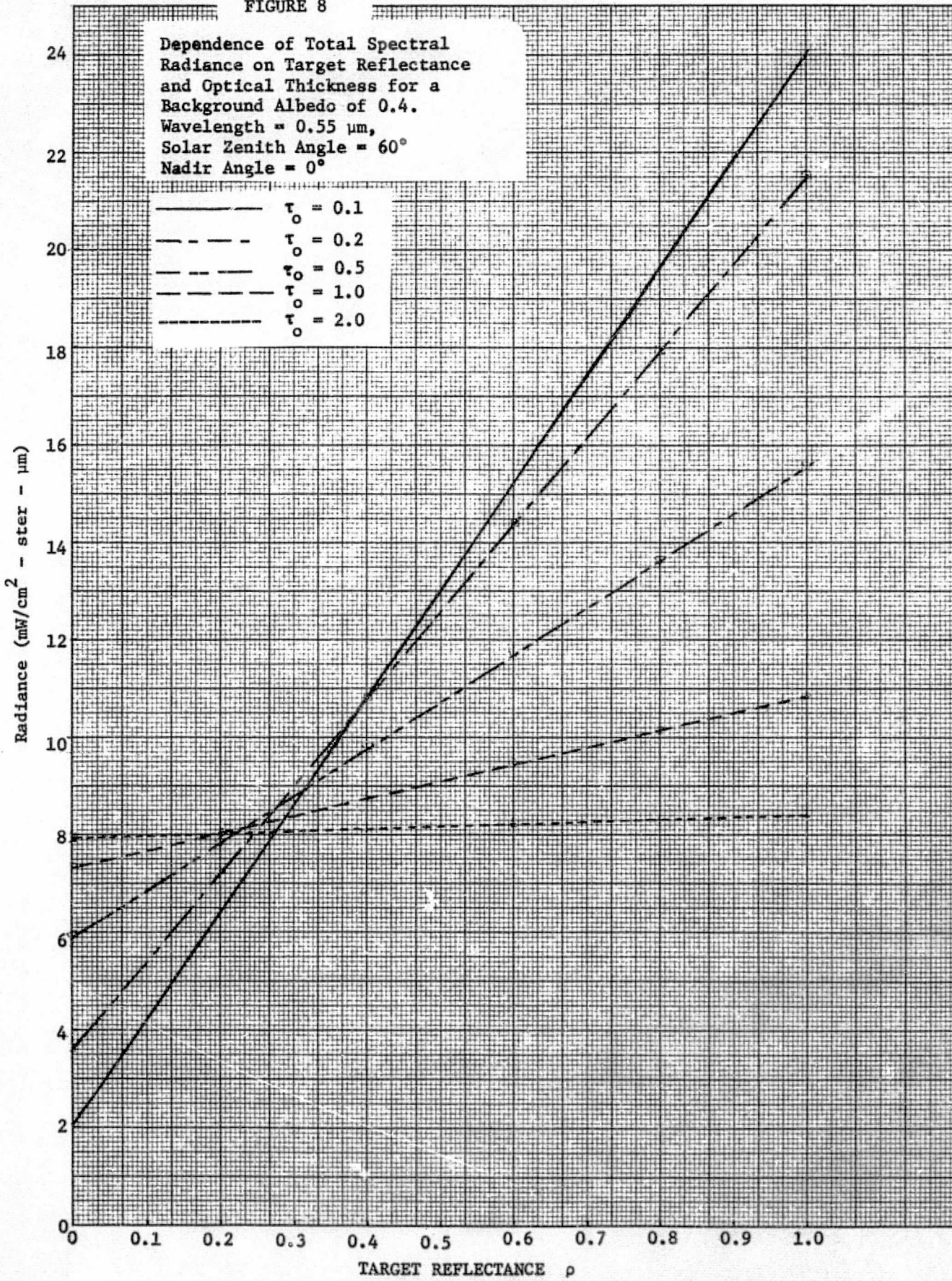
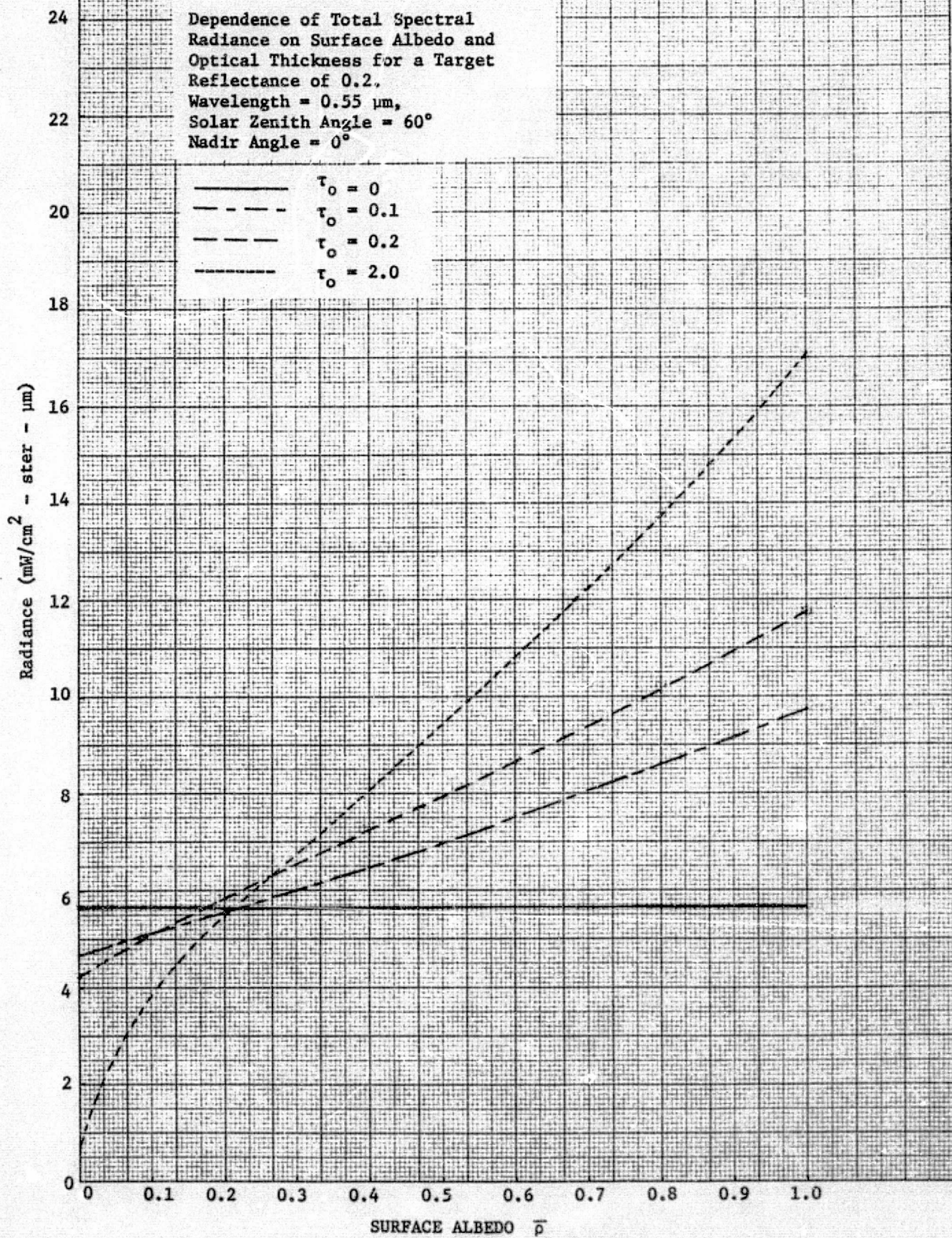
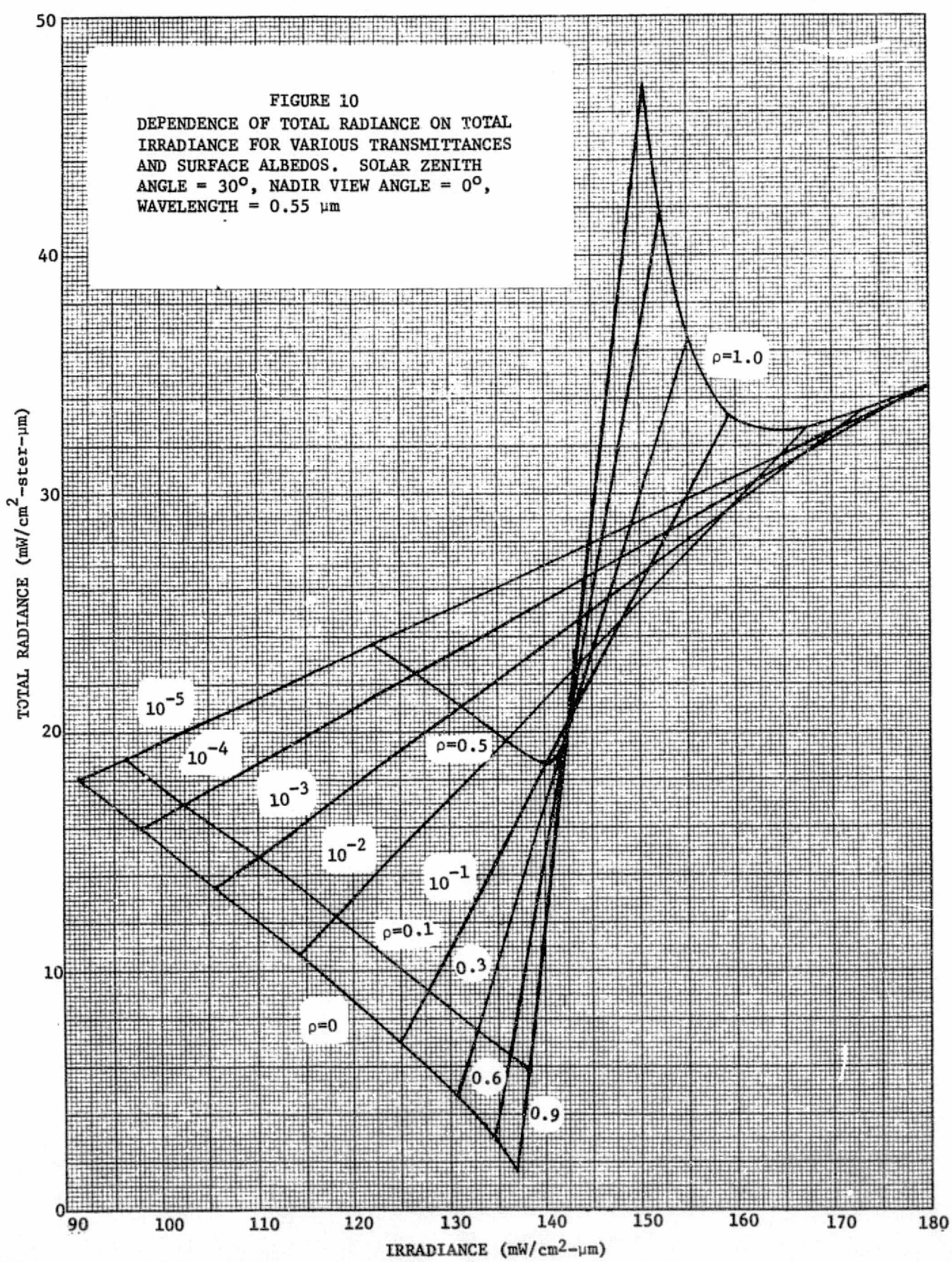


FIGURE 9





Finally, we can analyze the relationship between total radiance and path radiance (Fig. 11). Thus, for dark surfaces a hazy atmosphere produces a higher total radiance and path radiance than for clear atmospheres. For bright surfaces, however, the total radiance for hazy atmospheres is less than that for clear atmospheres. This effect is demonstrated by looking at ERTS photography (Turner et al., [5]).

It is assumed that in any analysis of multispectral data the wavelength, altitude, and geometric conditions are known. The unknown variables are optical thickness τ_o , target reflectance ρ , and background albedo $\bar{\rho}$. The values of these variables can be determined, however, by simultaneous measurement of the quantities L , L_p , T , and E . Thus, for uniform surfaces the state of the atmosphere and surface reflectances can be determined by analyzing multispectral data and auxiliary data. It is not always practical to measure the auxiliary data, however, and also the usual surface pattern is not uniform. The more complex case of a non-uniform surface will be treated in a later section.

3.3 CORRECTION ALGORITHM

We shall now consider a method which will allow us to eliminate the variable effects of the atmosphere. For simplicity, we shall investigate the case of satellite remote sensing, i.e., at an altitude where the optical depth is zero. The basic equation for total radiance is then

$$L(o, \mu, \phi) = L_o(\tau_o, \mu, \phi)T(o, \mu) + L_p(o, \mu, \phi) \quad (19)$$

[5] R. E. Turner, W. A. Malila, R. F. Nalepka, F. J. Thomson, Influence of the Atmosphere on Remotely Sensed Data, Proceedings of Society of Photo-Optical Instrumentation Engineers, 1975.

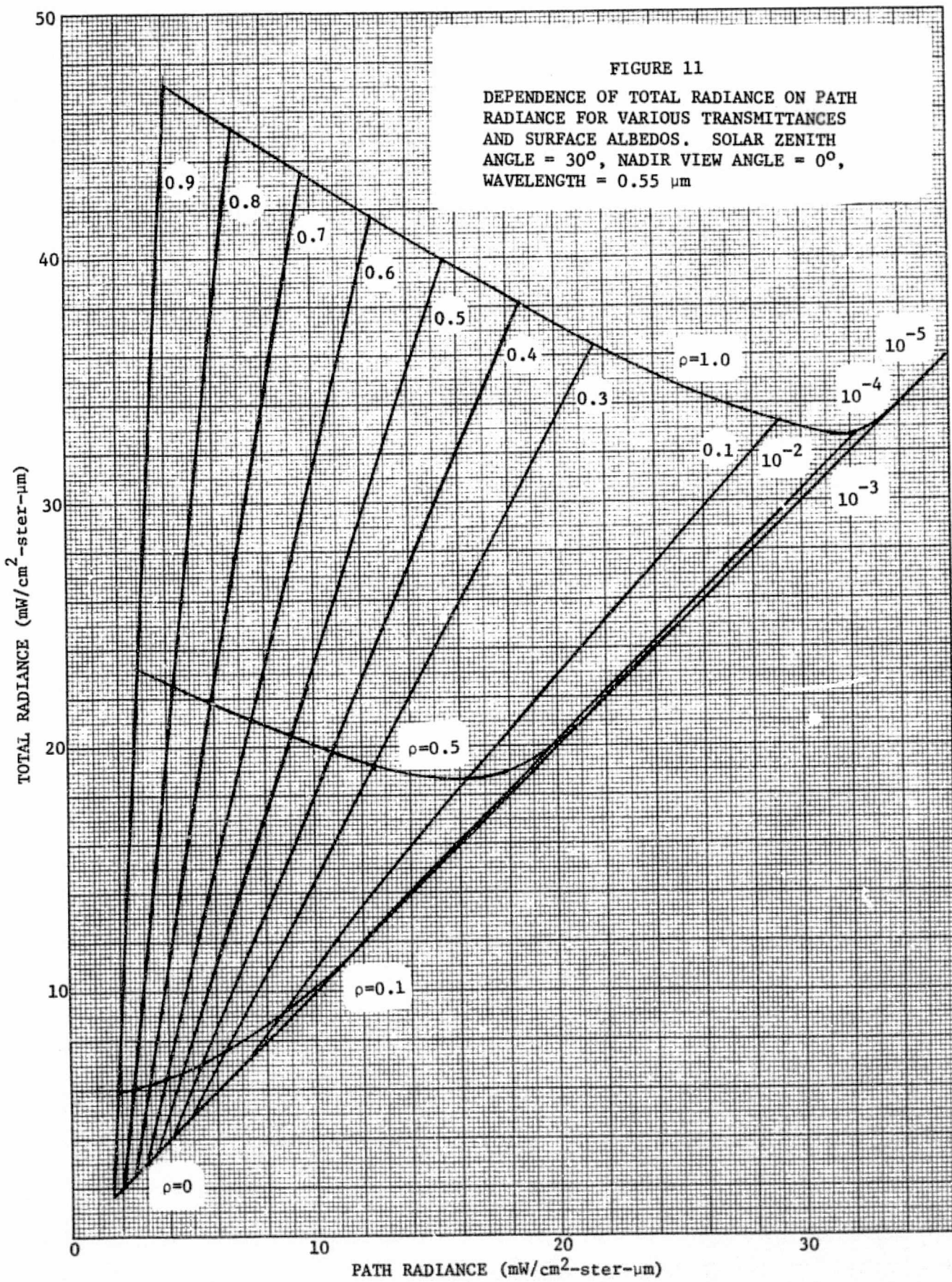


FIGURE 11
DEPENDENCE OF TOTAL RADIANCE ON PATH
RADIANCE FOR VARIOUS TRANSMITTANCES
AND SURFACE ALBEDOS. SOLAR ZENITH
ANGLE = 30° , NADIR VIEW ANGLE = 0° ,
WAVELENGTH = $0.55 \mu\text{m}$

where the zero means $\tau = 0$. The surface radiance is given by

$$L_o(\tau_o, \mu, \phi) = \int_0^{\infty} \int_{-\pi}^{\pi} \mu' \rho(\mu, \phi, \mu', \phi') [L_{\text{sun}}(\tau_o, -\mu', \phi') + L_{\text{sky}}(\tau_o, -\mu', \phi')] d\mu' d\phi' \quad (20)$$

where the direct solar radiance is

$$L_{\text{sun}}(\tau_o, -\mu, \phi) = E_o e^{-\tau_o/\mu} \delta(\mu - \mu_o) \delta(\phi - \phi_o) \quad (21)$$

and the second part of Eq. (20) is defined as the diffuse sky radiance

$L_D(\mu, \phi)$. Hence, we have

$$L_o(\tau_o, \mu, \phi) = \mu_o E_o e^{-\tau_o/\mu_o} \rho(\mu, \phi, -\mu_o, \phi_o) \quad (22)$$

for a general surface. We can now define an intrinsic radiance $L_I(\mu, \phi)$ as being that radiance which we would get if no atmosphere were present, i.e.,

$$L_I(\mu, \phi) = \mu_o E_o \rho(\mu, \phi, -\mu_o, \phi_o) \quad (23)$$

Thus, Eq. (19) becomes

$$L(o, \mu, \phi) = L_I(\mu, \phi) T(o, \mu_o) T(o, \mu) + L_D(\mu, \phi) T(o, \mu) + L_p(o, \mu, \phi) \quad (24)$$

The intrinsic radiance can therefore be put in the form

$$L_I(\mu, \phi) = R(\mu, \mu_o) L(o, \mu, \phi) - S(\mu, \mu_o, \phi) \quad (25)$$

where $L_I(\mu, \phi)$ is the "corrected" radiance and $L(o, \mu, \phi)$ is the measured value obtained by remote sensing. The correction functions $R(\mu, \mu_o)$ and $S(\mu, \mu_o, \phi)$ are either determined experimentally or by model calculations. If we assume Lambertian surfaces then the correction functions can be calculated easily.

In this case

$$L_D(\mu, \phi) = \frac{\rho}{\pi} E_- \quad (26)$$

where E_{\perp} is the downward diffuse irradiance on the target. The intrinsic radiance in this case becomes

$$L_I(\mu, \phi) = \frac{\rho}{\pi} \mu_o E_o \quad (27)$$

Now, we also have

$$\tilde{E}_{\perp} = \tilde{E}_{\perp} - \mu_o E_o T(\mu_o) \quad (28)$$

where \tilde{E}_{\perp} is the total downward irradiance on the target. Using these relationships on Eq. (24) we get

$$R(\mu, \mu_o) = \frac{1}{T(\mu_o)[T(\mu)-1] + \tilde{E}_{\perp}/\mu_o E_o} \quad (29)$$

$$S(\mu, \mu_o, \phi) = R(\mu, \mu_o) L_p(o, \mu, \phi) \quad (30)$$

where all quantities in Eqs. (29) and (30) are easily measurable except the path radiance.

Standard procedures were developed (Turner & Spencer [6], Horvath et.al., [7]) for the correction of multispectral satellite data for atmospheric variations involving sun angle, surface albedo, and atmospheric transmittance. The methods are not as general as the procedure described above but do provide the user with a simple algorithm which can be used to quantify the atmospheric variations.

3.4 VARIATION OF PARAMETERS

In order to understand the variation in multispectral data as a result of a variable atmosphere we will construct an atmospheric state and calculate radiance at various points of the scene. These will then represent the actual,

[6] R.E. Turner & M.M. Spencer, Atmospheric Model for Correction of Spacecraft Data, Proceedings of the 8th Int. Conf. on Remote Sensing of Env., Ann Arbor, 1972

[7] R. Horvath, M. Spencer, & R. Turner, Atmospheric Correction & Simulation of Space Acquired Remote Sensor Data: 0.4-1.0 μm Spectral Range, Report 10657-5-F, WRL, Institute of Science & Tech. Univ of Mich. 1972.

measured radiance for a specific atmospheric condition. Then, selecting a smaller number of points which would simulate auxiliary measurements of optical thickness, we use these data points to construct an approximate surface and then calculate new radiance. Comparing the actual with the calculated then provides us with a measure of the atmospheric variability.

As we have seen, for a given visual range the optical thickness may vary around some mean value $\bar{\tau}_o$. Let us therefore consider a 21×21 element frame of data with a spatially constant surface albedo and allow the optical thickness to have maxima and minima at N points in the scene, i.e.,

$$\tau_o(x,y) = \bar{\tau}_o + \sum_{i=1}^N \sigma_i e^{-[a_i(x-x_i)^2 + b_i(y-y_i)^2]} \quad (31)$$

where the σ_i is the value of the increase or decrease in the mean optical thickness at the i^{th} point and the a_i, b_i are the widths of the Gaussian distributions. Using the radiative-transfer model we can calculate the actual radiances for this surface at any point (x,y) . Then, choosing n sample points corresponding to optical thickness measurements we determine the corresponding $\tau_o(x_j, y_j)$, ($j=1, \dots, n$) and using regression analysis determine the best surface through the n points. As n increases the radiances as calculated by using the regression surface should approach those determined by the exact calculation.

Case I: Four Point Atmosphere

As an illustration of this method let us consider the simplified case of circular contours at four points in a 21×21 frame. Thus $a_i = b_i = a$ for all i . We shall consider two visibilities with fluctuations in the optical thickness surface consistent with Eq. (31). The parameters are given in Table 1.

TABLE 1. PARAMETERS FOR MULTI-GAUSSIAN OPTICAL THICKNESS SURFACE

V = 10 km ($\bar{\tau}_o = 0.611$)				V = 23 km ($\bar{\tau}_o = 0.379$)			
i	x _i	y _i	σ_i	x _i	y _i	σ_i	
1	6	6	0.072	6	6	0.038	
2	6	16	0.241	6	16	0.125	
3	16	6	-0.241	16	6	-0.125	
4	16	16	-0.072	16	16	-0.038	

The smaller absolute quantities correspond to a 15 per cent fluctuation in the aerosol optical thickness and the larger absolute quantities refer to a 50 per cent fluctuation. Using these parameters in Eq. (31) we calculated an "actual" radiance L_a for each of the 441 points of the frame. Then selecting $n(<441)$ points according to the arrays shown in Fig. 12 we used regression analysis to determine the best surface through the n points. Using this surface we then calculated radiances L_c for each of the 441 points.

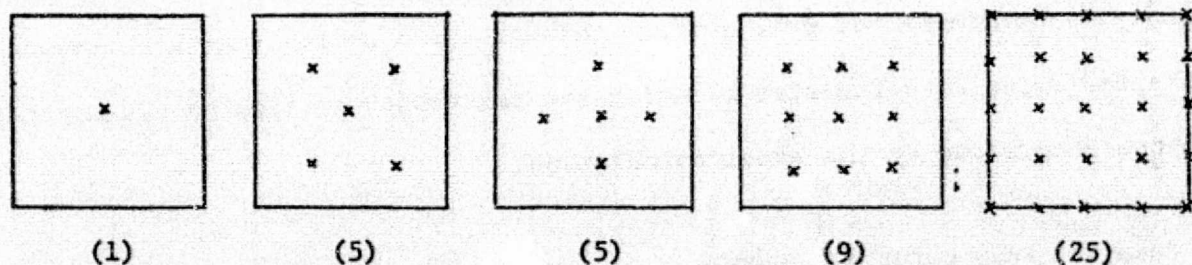


FIG. 12. OPTICAL THICKNESS EXPERIMENTAL ARRAY

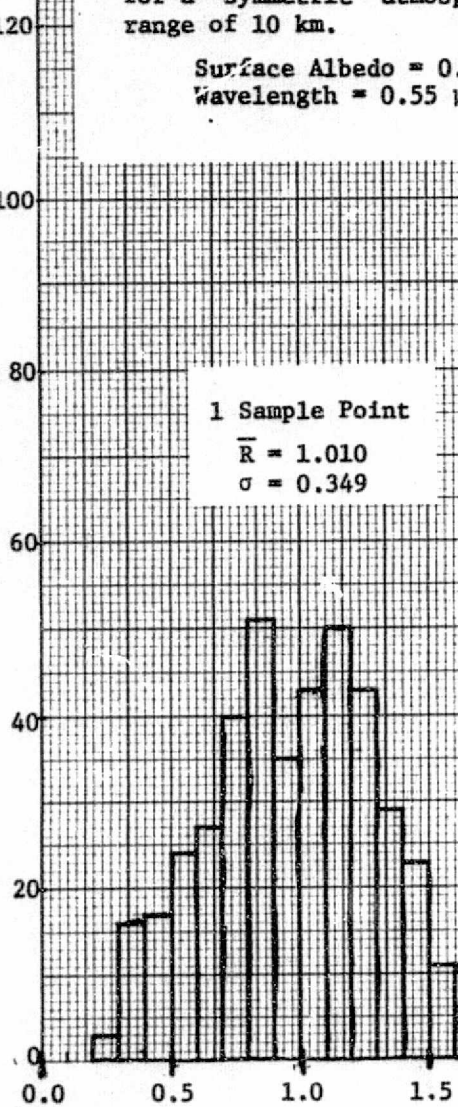
If the τ_o regression surface corresponded exactly to the known τ_o surface all the radiances should be the same. In reality there is a spread. For the 1, 9, and 25 sample cases we plot histograms in Fig. 13. As can be seen there is a considerable improvement as the number of "experimental" sample points increases. Figure 14 illustrates the difference between the two arrays involving five sensors. Figure 15a illustrates the spatial variation in the actual radiance based upon the actual τ_o surface (Fig. 15b) according to Eqn. 31. The large peak occurs in the lower left corner and the big valley is in the upper right corner. For $n=1$, i.e., only one sample point in the center of the frame the regression surface is a plane. Hence, a contour plot of L_c/L_a should merely reflect the variation of the τ_o surface. This is demonstrated in Fig. 16a. For the two cases of five sensors, however, the ratio varies somewhat as is illustrated in Figs. 17a and 17b. The regression surfaces in these cases are quadratic in the x direction but linear in y. For the nine sensor array there is some improvement as shown in Fig. 16b. Finally, the 25 sensor case is depicted in Fig. 18. Here the regression surface is a plane instead of a two-dimensional quadratic. This undoubtedly arises because of the symmetry introduced by our original choice of a multi-Gaussian surface. Hence, the improvement is less than in the nine sensor case. This means that one really should use regression analysis for much higher order algebraic surfaces or for multi-Gaussian regression surfaces. Such analysis is now continuing. As proof of the concept that an increase in the number of sensors does not lead to improvement for quadratic surfaces we used 49 sensor points. Here the result was still another plane surface with a result similar to that for the $n = 25$ case. Additional runs were

FIGURE 13

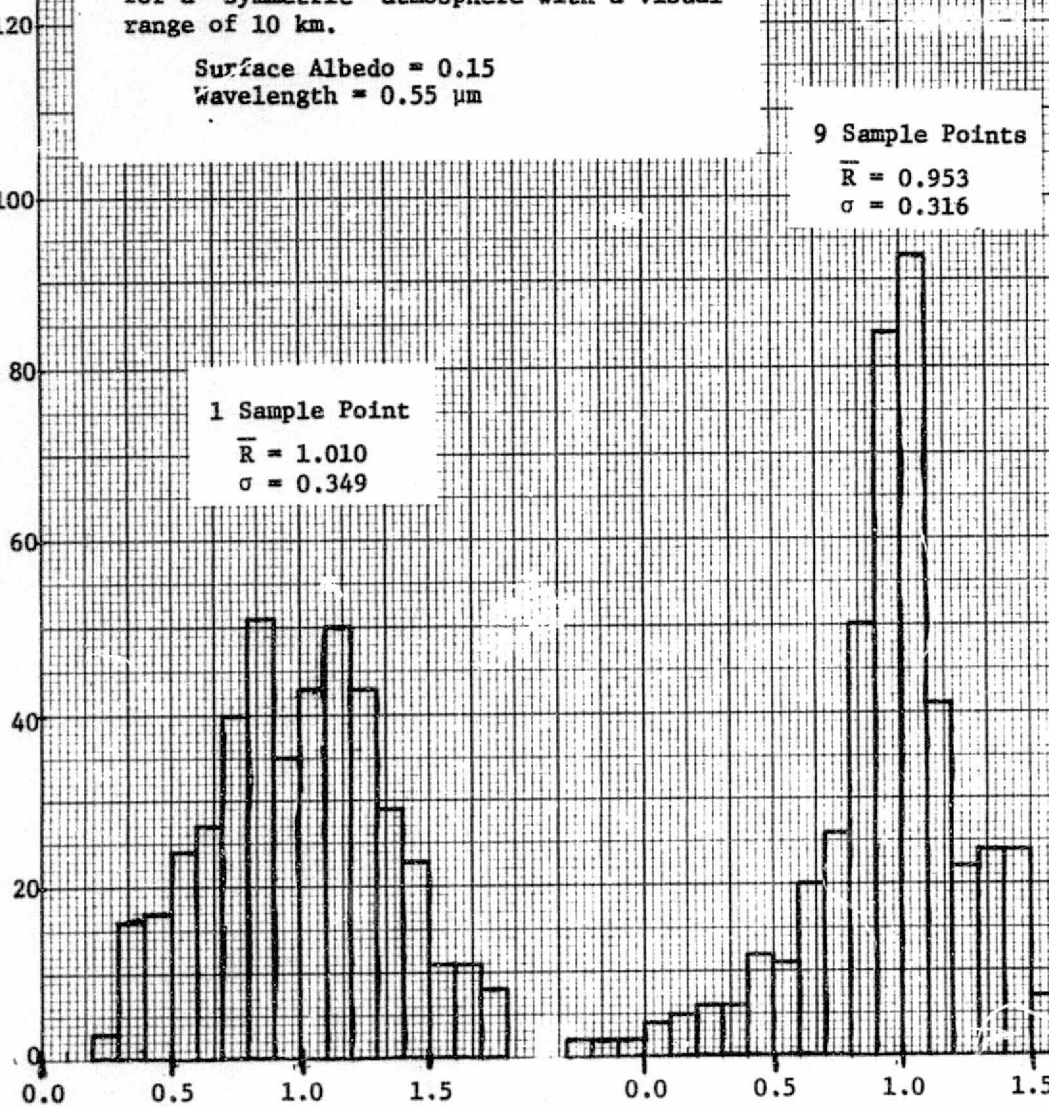
Histograms of $L_I(\text{calculated})/L_I(\text{actual})$
for a "symmetric" atmosphere with a visual
range of 10 km.

Surface Albedo = 0.15
Wavelength = 0.55 μm

1 Sample Point
 $\bar{R} = 1.010$
 $\sigma = 0.349$



9 Sample Points
 $\bar{R} = 0.953$
 $\sigma = 0.316$



25 Sample Points
 $\bar{R} = 1.014$
 $\sigma = 0.216$

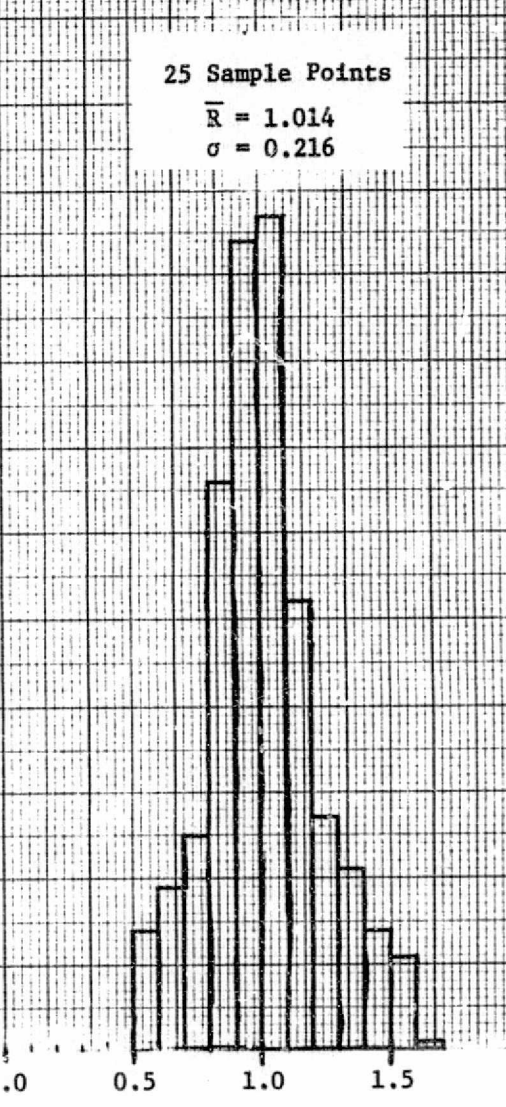
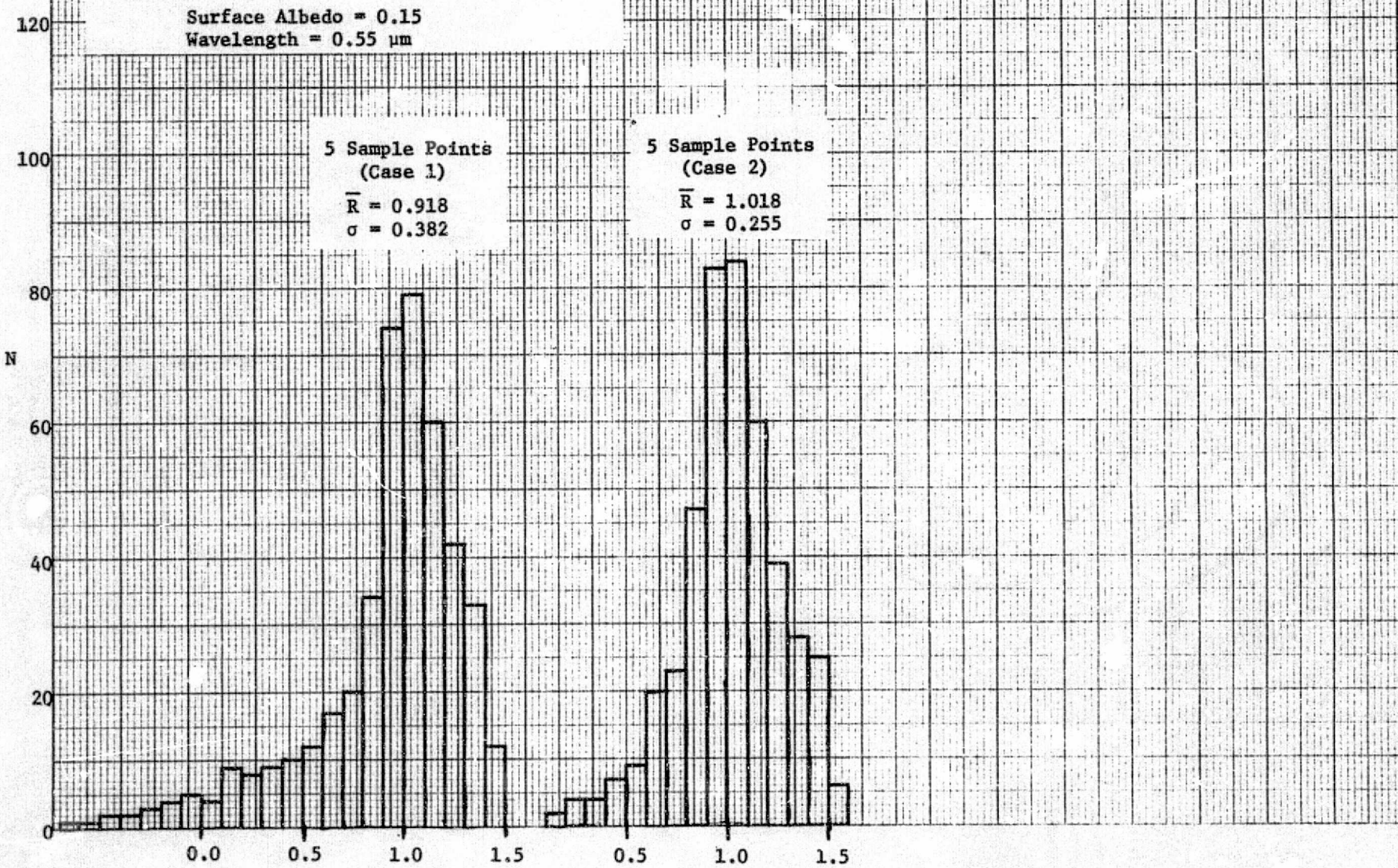


FIGURE 14

Histograms of $L_I(\text{calculated})/L_I(\text{actual})$
for a "symmetric" atmosphere with a
visual range of 10 km.

Surface Albedo = 0.15
Wavelength = 0.55 μm



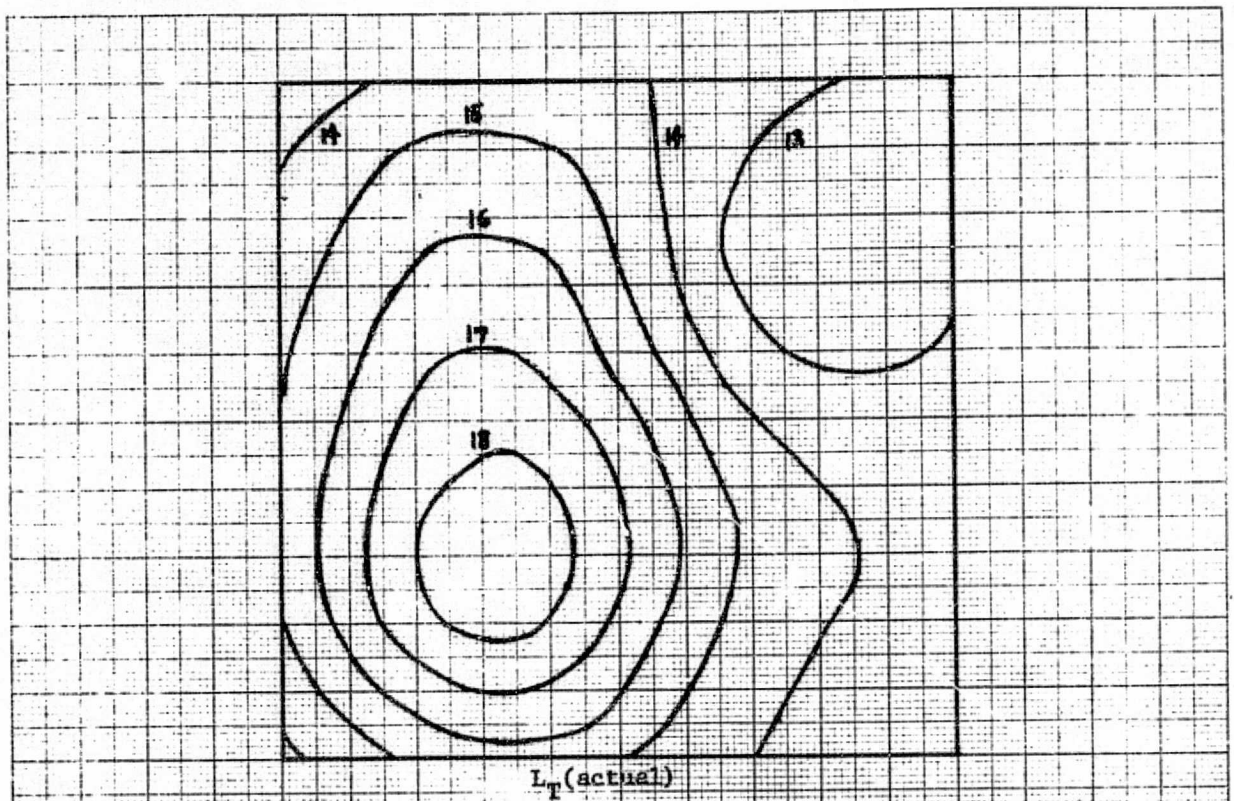


FIGURE 15a. Actual Radiance Surface for
"symmetric" atmosphere
 $V=10$ km, $\bar{\rho}=0.15$, $\lambda=0.55 \mu\text{m}$

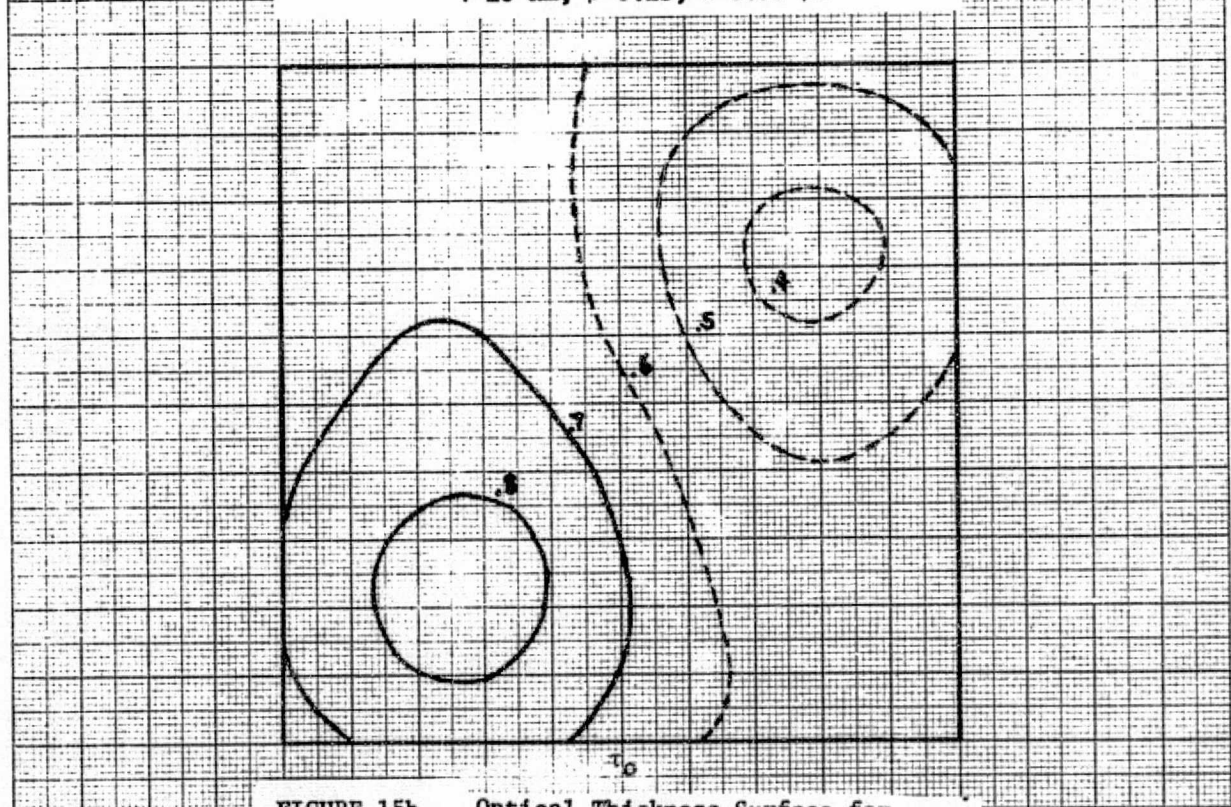


FIGURE 15b. Optical Thickness Surface for
"Symmetric" Atmosphere
 $V=10$ km, $\lambda=0.55 \mu\text{m}$

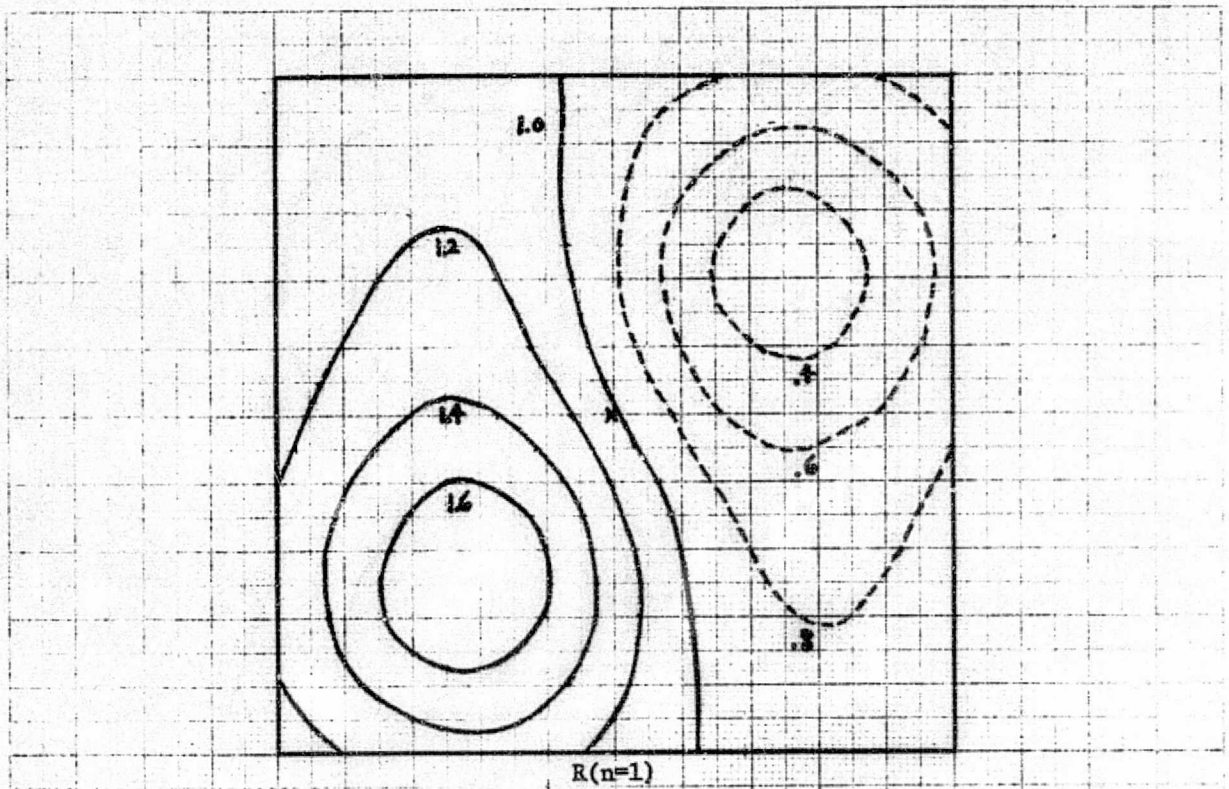


FIGURE 16a. Ratio Surface for "Symmetric"
Atmosphere with One Sensor
 $V=10$ km

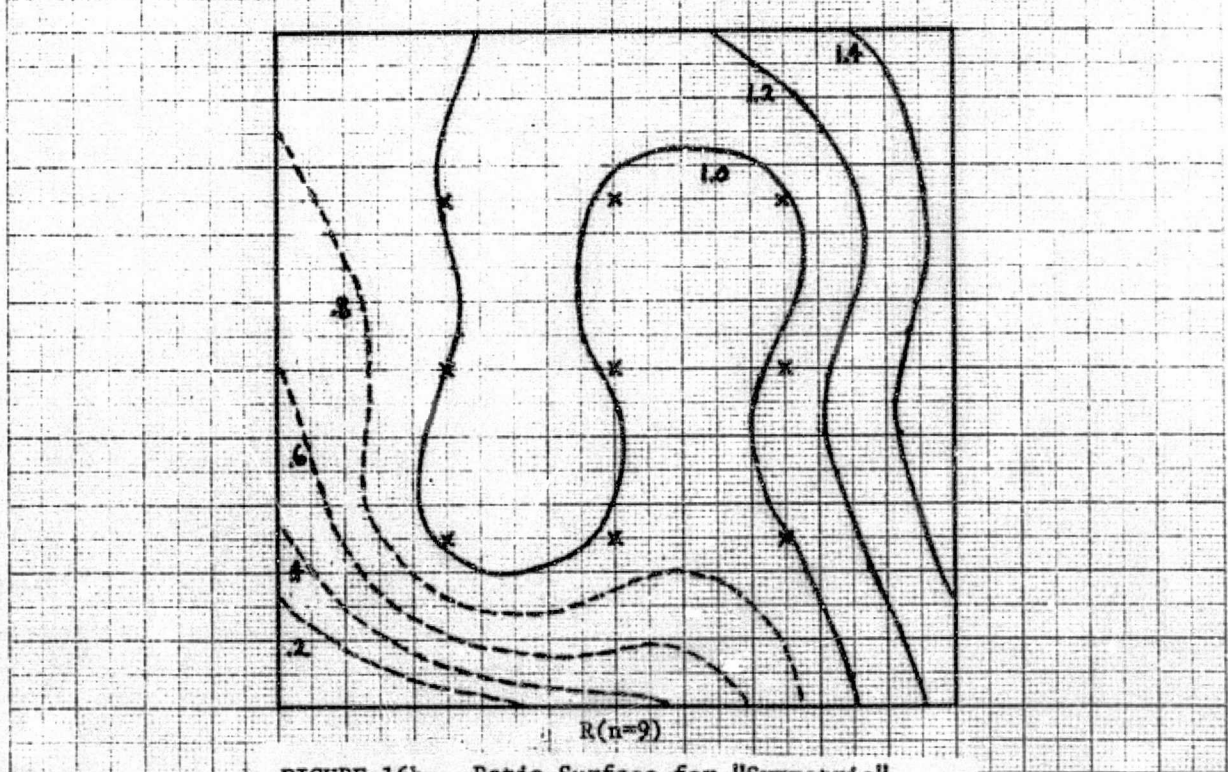


FIGURE 16b. Ratio Surface for "Symmetric"
Atmosphere with Nine Sensors
 $V=10$ km

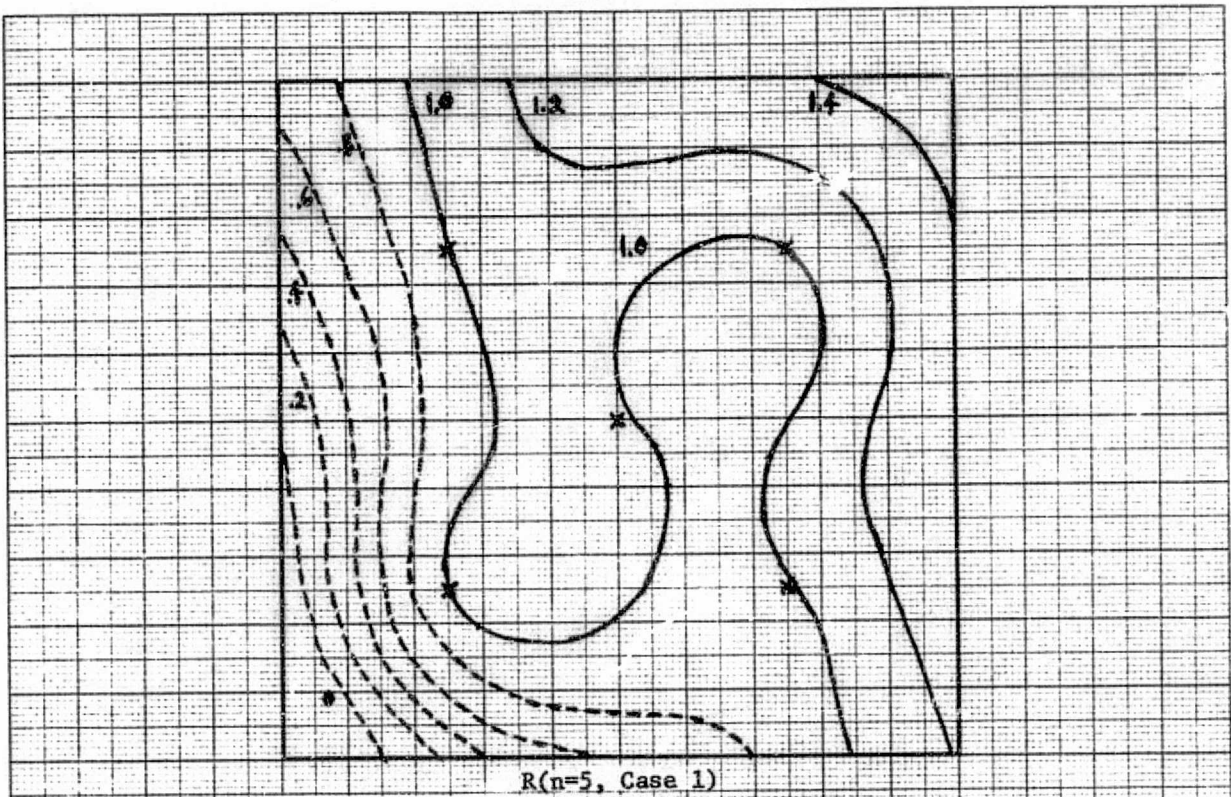


FIGURE 17a. Ratio Surface for "Symmetric"
Atmosphere with Five Sensors
 $V=10$ km

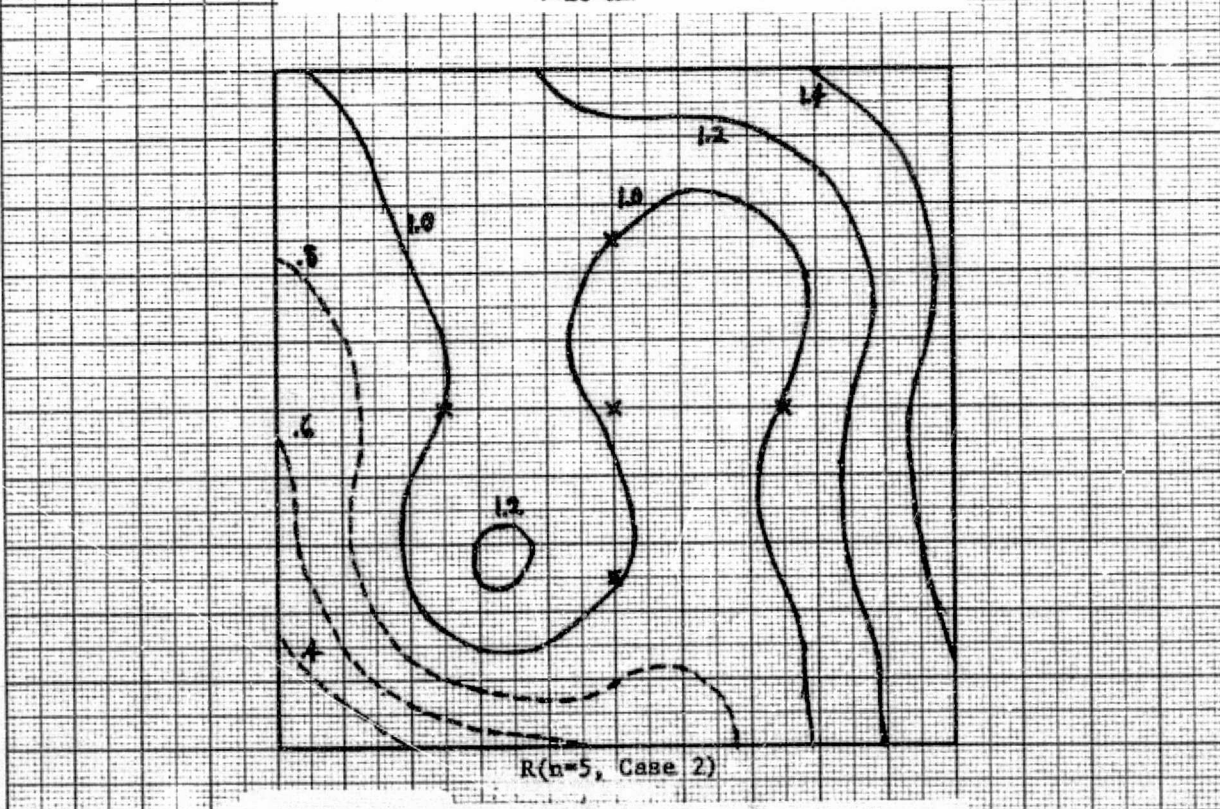


FIGURE 17b. Ratio Surface for "Symmetric"
Atmosphere with Five Sensors
 $V=10$ km

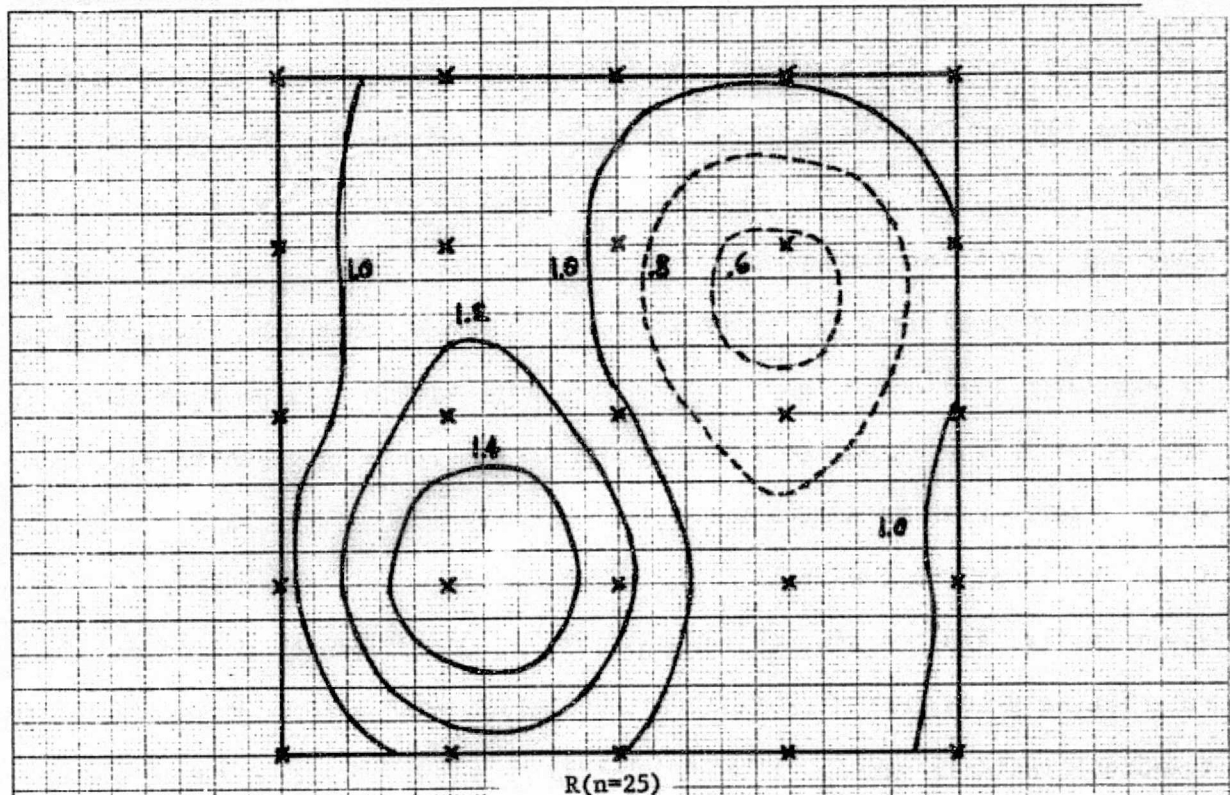


FIGURE 18. Ratio Surface for "Symmetric"
Atmosphere with 25 Sensors
 $V=10 \text{ km}$

made, this time using a visual range of 23 km. The results are depicted in Figs. 19 and 20. As before, the number of points cluster around a ratio of one.

Case II: Two Point Atmosphere

We now consider a different atmospheric state, this time characterized by one large peak and a large valley at points within a frame such that the symmetry is broken. An illustration of this case is given in Fig. 21b where a large peak is in the upper left section of the frame and a valley is in the lower right section. The corresponding radiance surface is shown in Fig. 21a. Again, selecting 1, 5, 9, and 25 sensor points and calculating a regression surface, we determined the calculated radiance-to-actual radiance ratio. This is plotted in Figs. 22 and 23 for a visual range of 10 km and in Figs. 24 and 25 for a visual range of 23 km. Here we see a definite improvement as the number of sensors increases because the regression surface more nearly matches the actual surface. In this case that occurs because we have less symmetry than in the four point atmosphere. This is also obvious from the contour plots of Figs. 26a, 26b, 27a, 27b, and 28. For $n = 1$ there is a plane regression surface and hence the ratios follow the contour of the τ_o surface. For $n = 5, 9$, and 25 however, the surface is approaching unity as we are finding a better approximation to the actual τ_o surface.

Hence, what has been demonstrated so far is that there is considerable improvement in the determination of intrinsic radiances if enough sensor points are included in a scene and if there is a lack of symmetry. Lack

FIGURE 19

Histograms of $L_I(\text{calculated})/L_I(\text{actual})$
for a "Symmetric" Atmosphere with a
Visual Range of 23 km.

Surface Albedo = 0.15
Wavelength = 0.55 μm

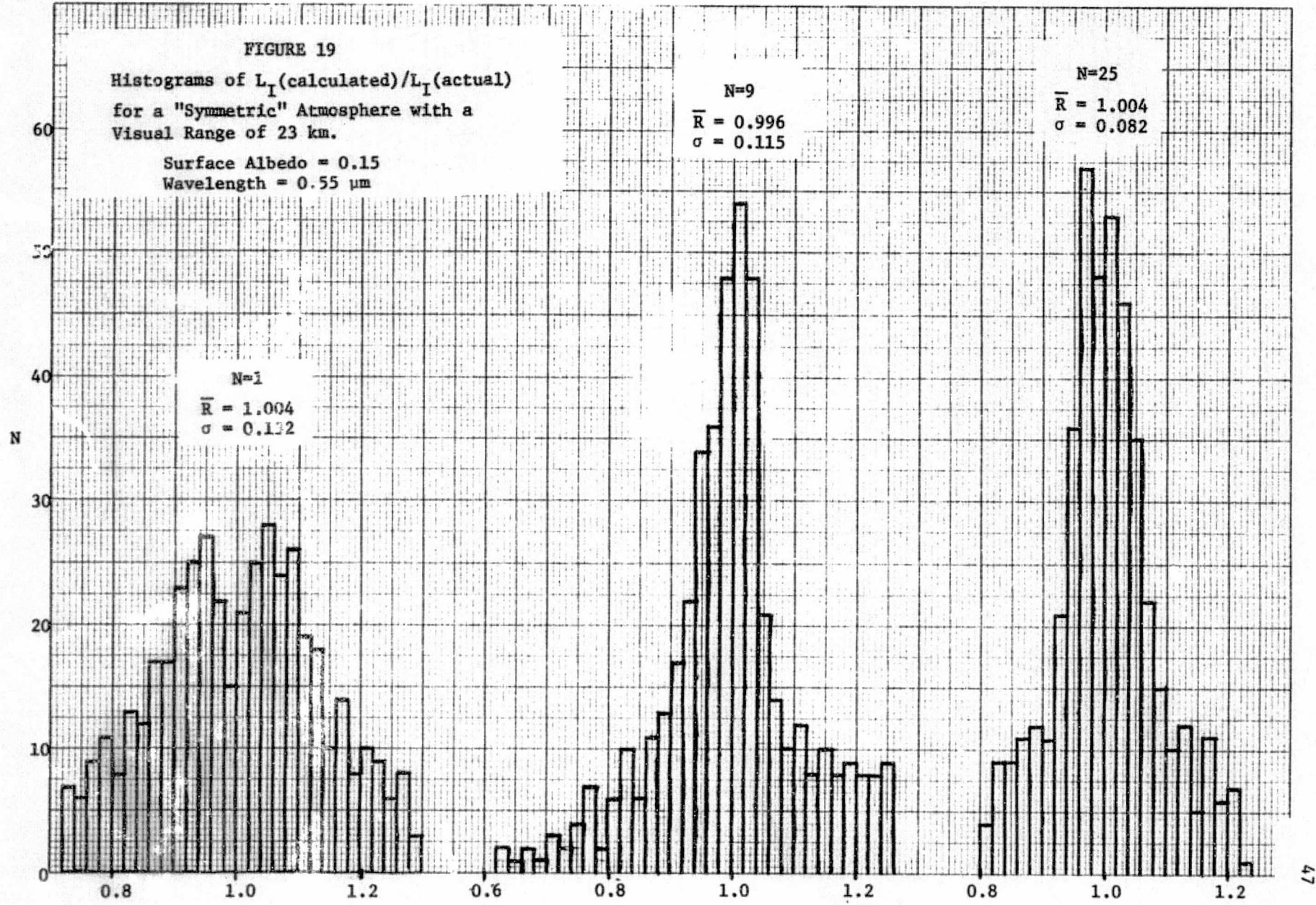


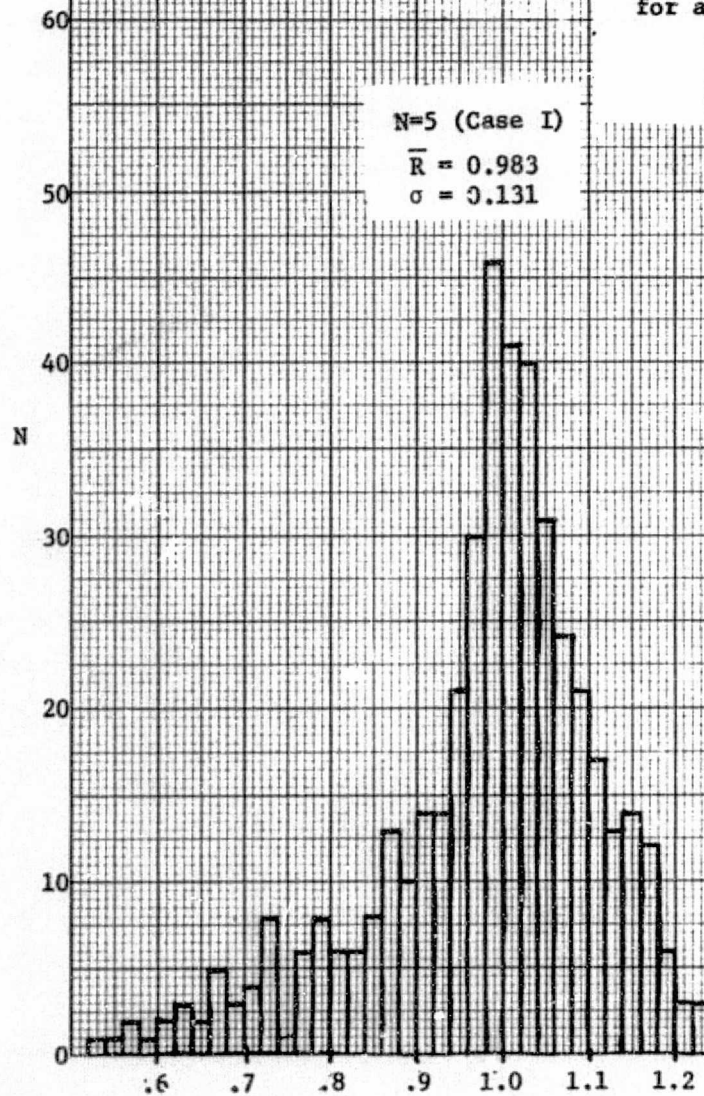
FIGURE 20

Histograms of $L_I(\text{calculated})/L_I(\text{actual})$
for a "Symmetric" Atmosphere.

Visual Range = 23 km
Surface Albedo = 0.15
Wavelength = 0.55 μm

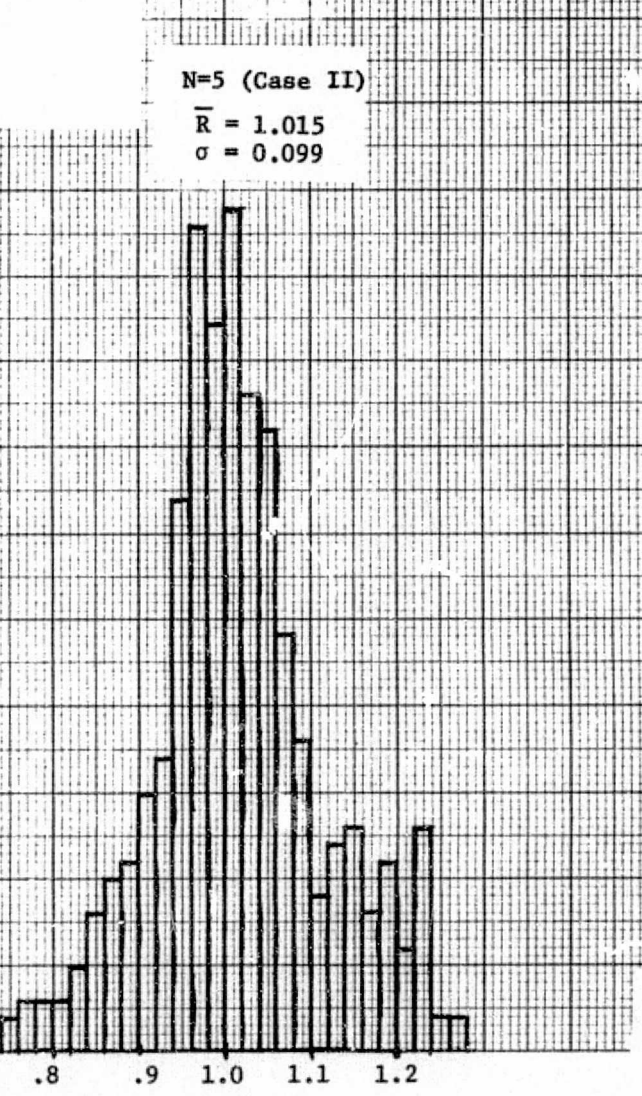
N=5 (Case I)

$$\bar{R} = 0.983$$
$$\sigma = 0.131$$



N=5 (Case II)

$$\bar{R} = 1.015$$
$$\sigma = 0.099$$



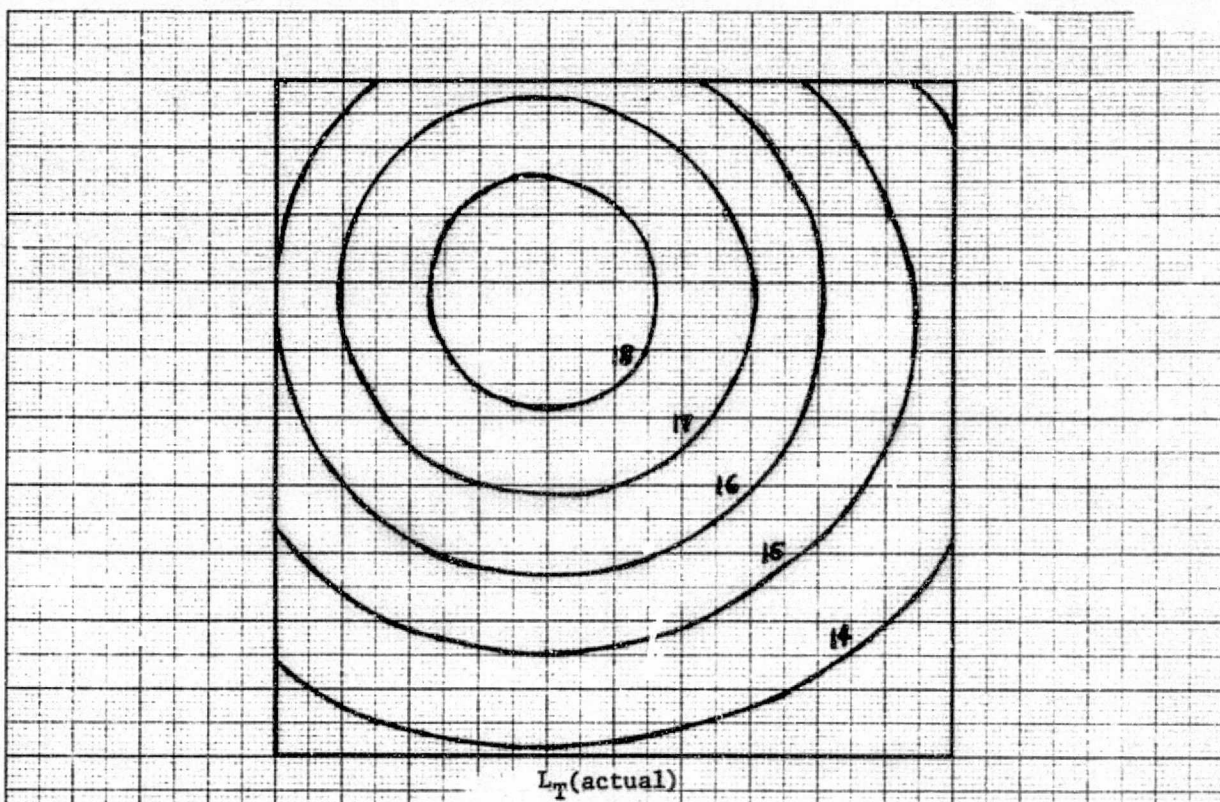


FIGURE 21a. Actual Radiance Surface for
"Asymmetric" Atmosphere
 $V=10 \text{ km}$, $\bar{\rho}=0.15$, $\lambda=0.55 \mu\text{m}$

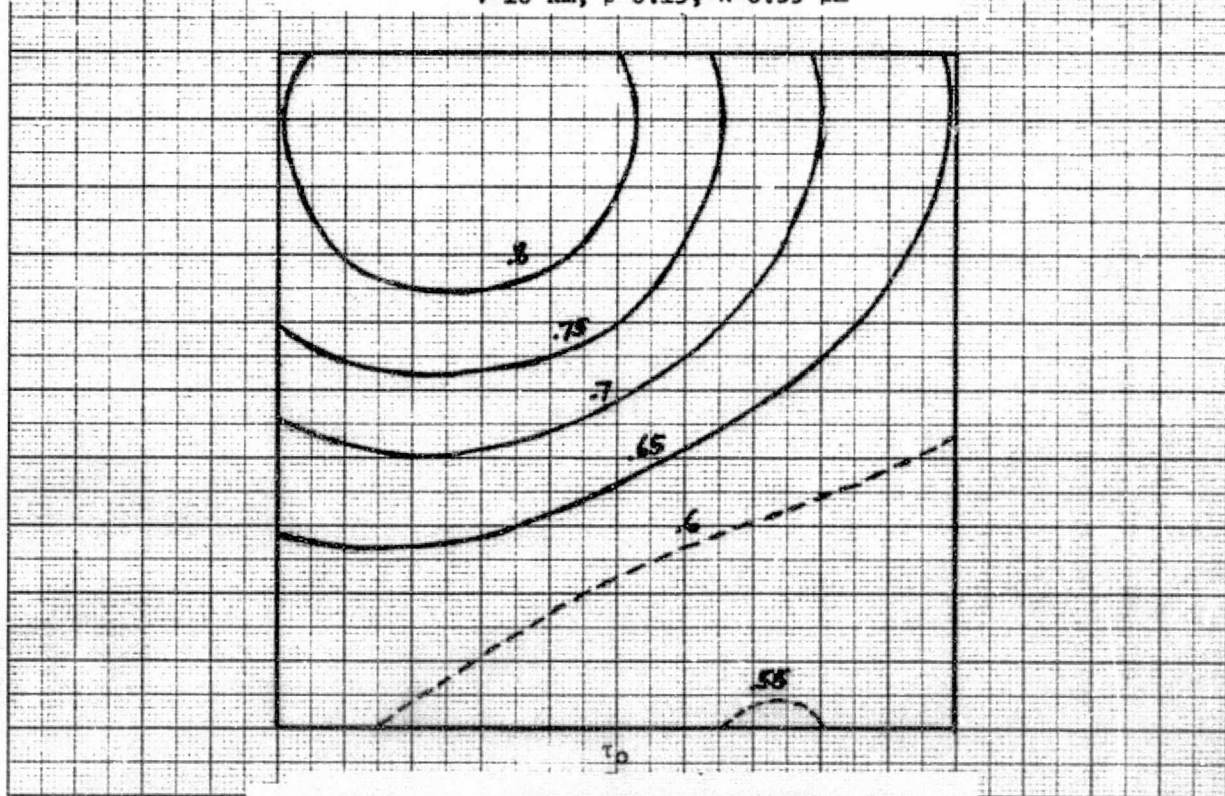
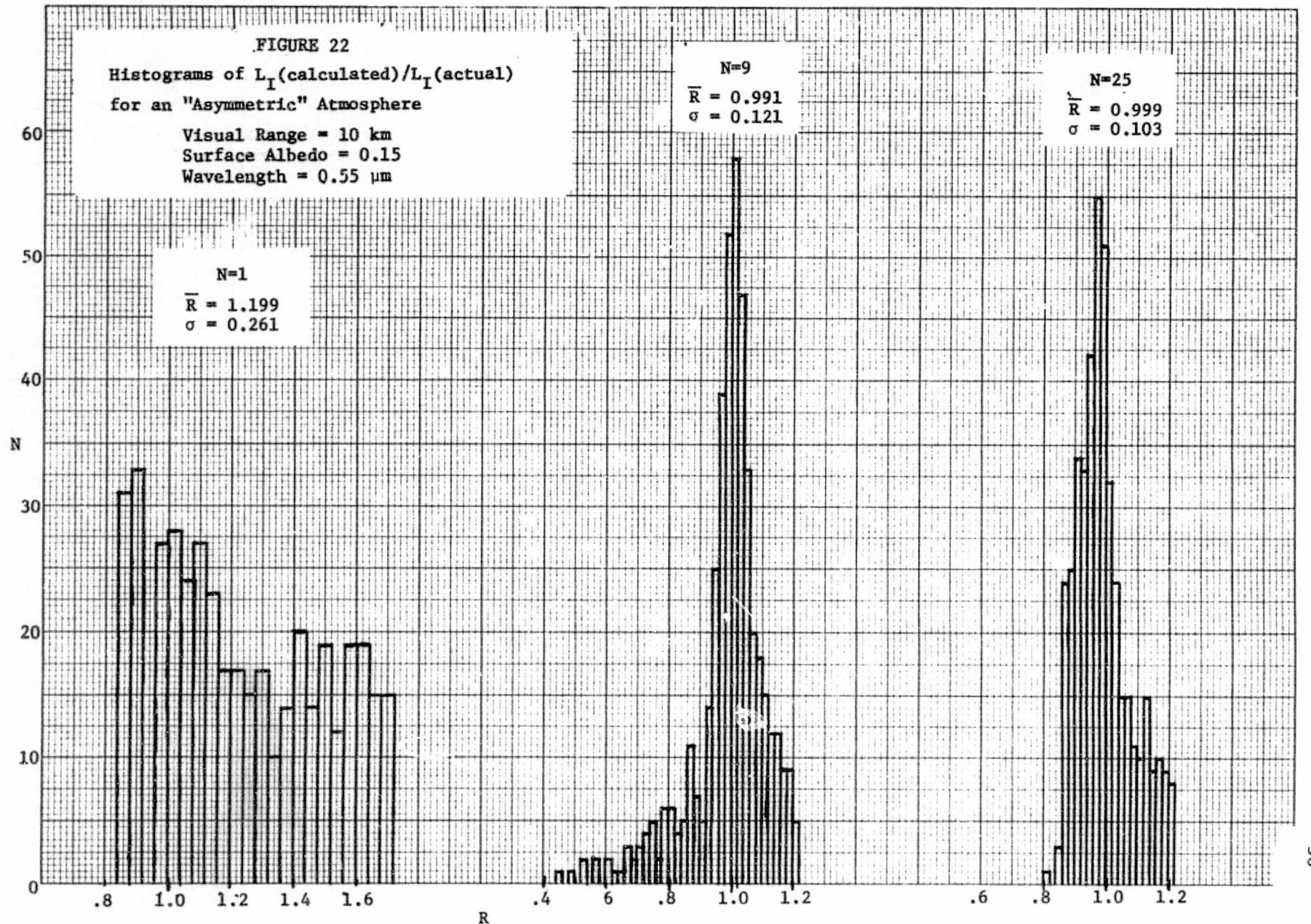


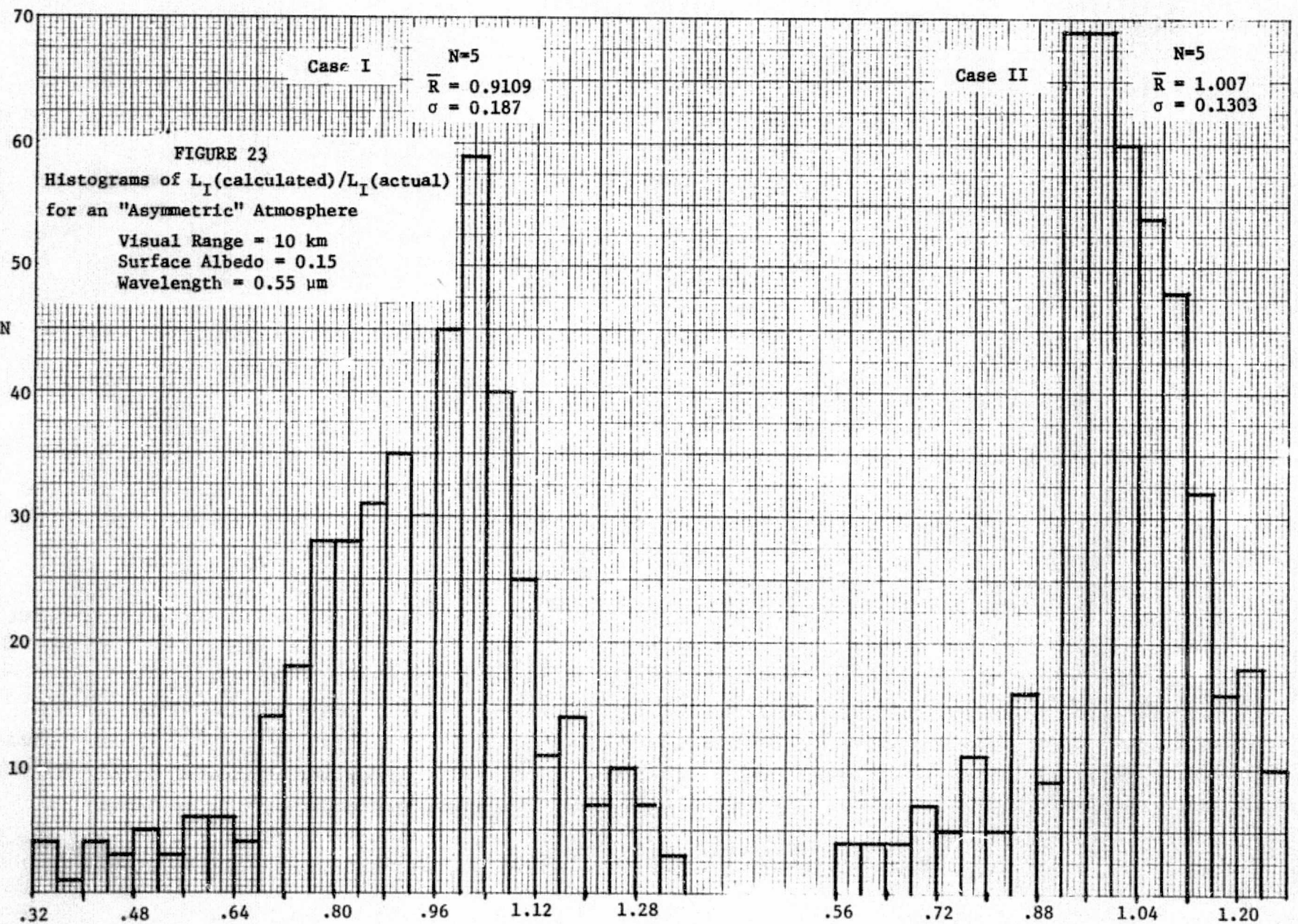
FIGURE 21b. Optical Thickness Surface for
"Asymmetric" Atmosphere
 $V=10 \text{ km}$, $\lambda=0.55 \mu\text{m}$

FIGURE 22

Histograms of $L_I(\text{calculated})/L_I(\text{actual})$
for an "Asymmetric" Atmosphere

Visual Range = 10 km
Surface Albedo = 0.15
Wavelength = 0.55 μm





140

FIGURE 24
Histograms of L_I (calculated)/ L_I (actual)
for an "Asymmetric" Atmosphere

Visual Range = 23 km
 Surface Albedo = 0.15
 Wavelength = 0.55 μm

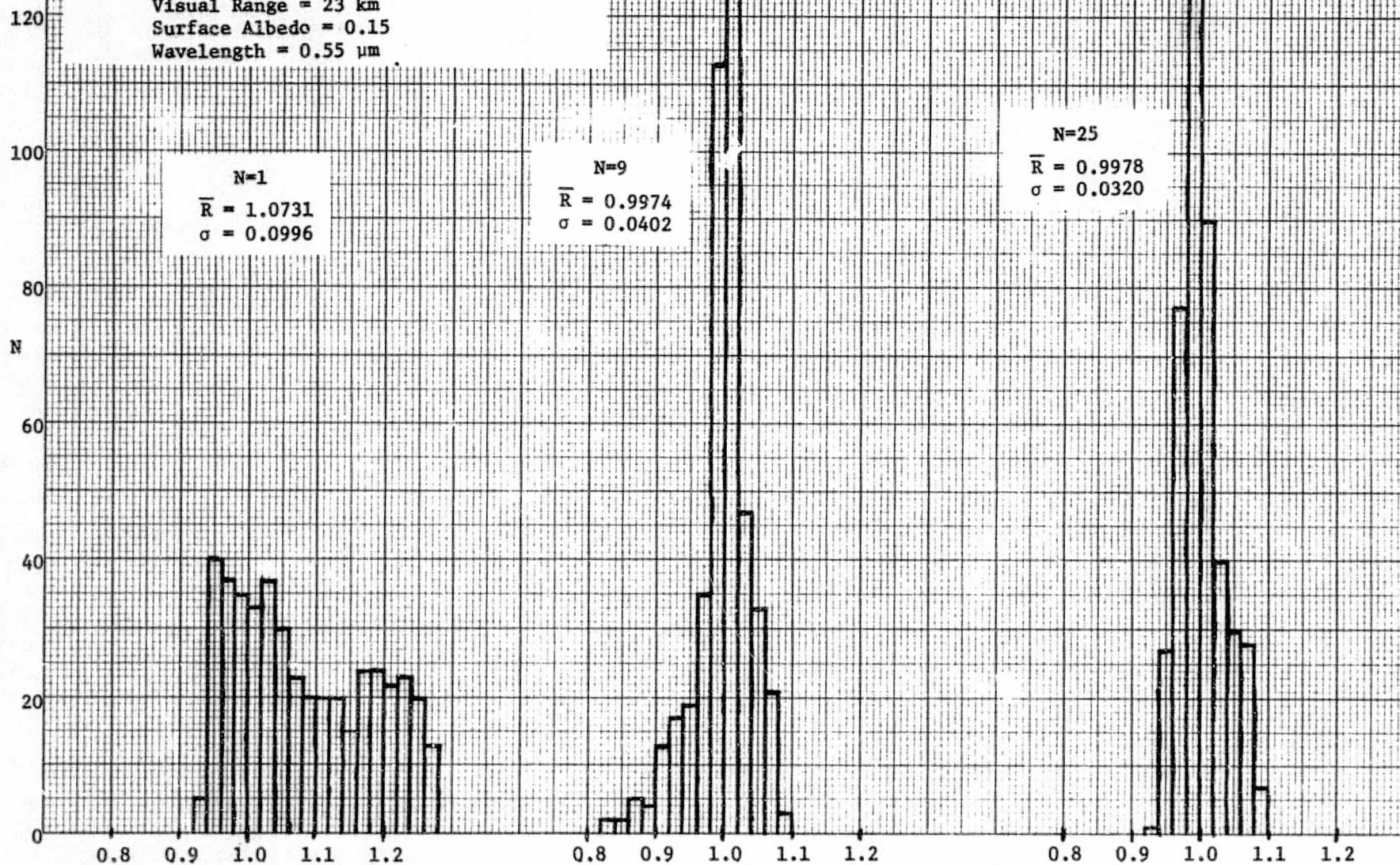
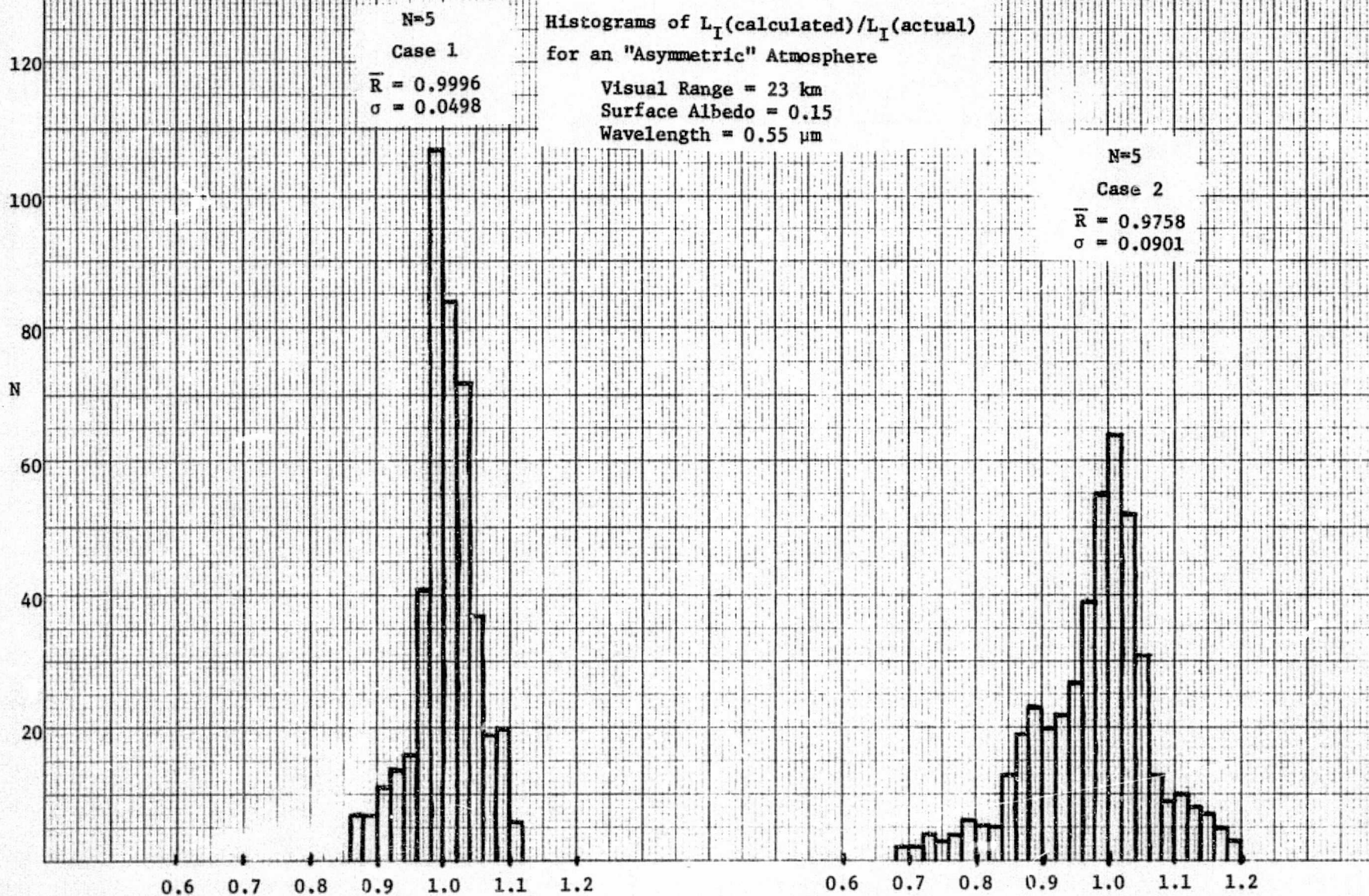


FIGURE 25

Histograms of $L_I(\text{calculated})/L_I(\text{actual})$
for an "Asymmetric" Atmosphere
Visual Range = 23 km
Surface Albedo = 0.15
Wavelength = 0.55 μm



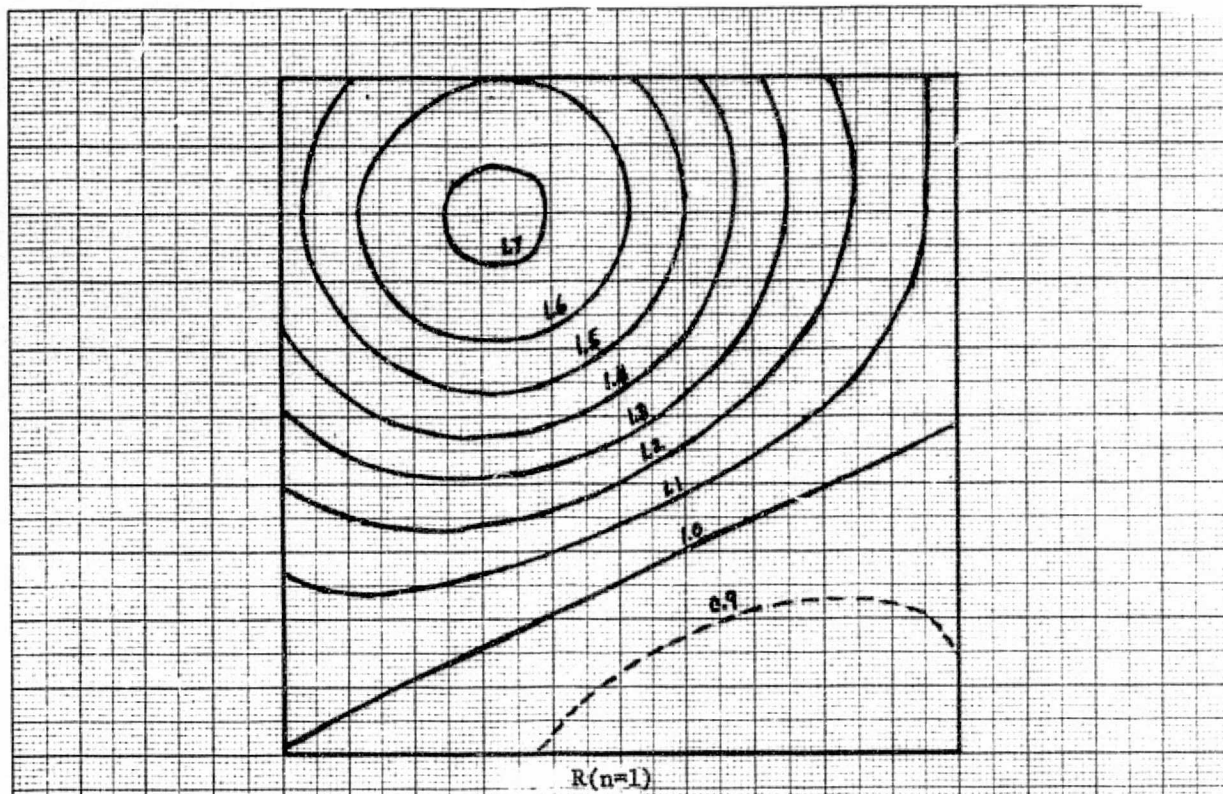


FIGURE 26a. Ratio Surface for "Asymmetric"
Atmosphere with One Sensor
 $V=10 \text{ km}$

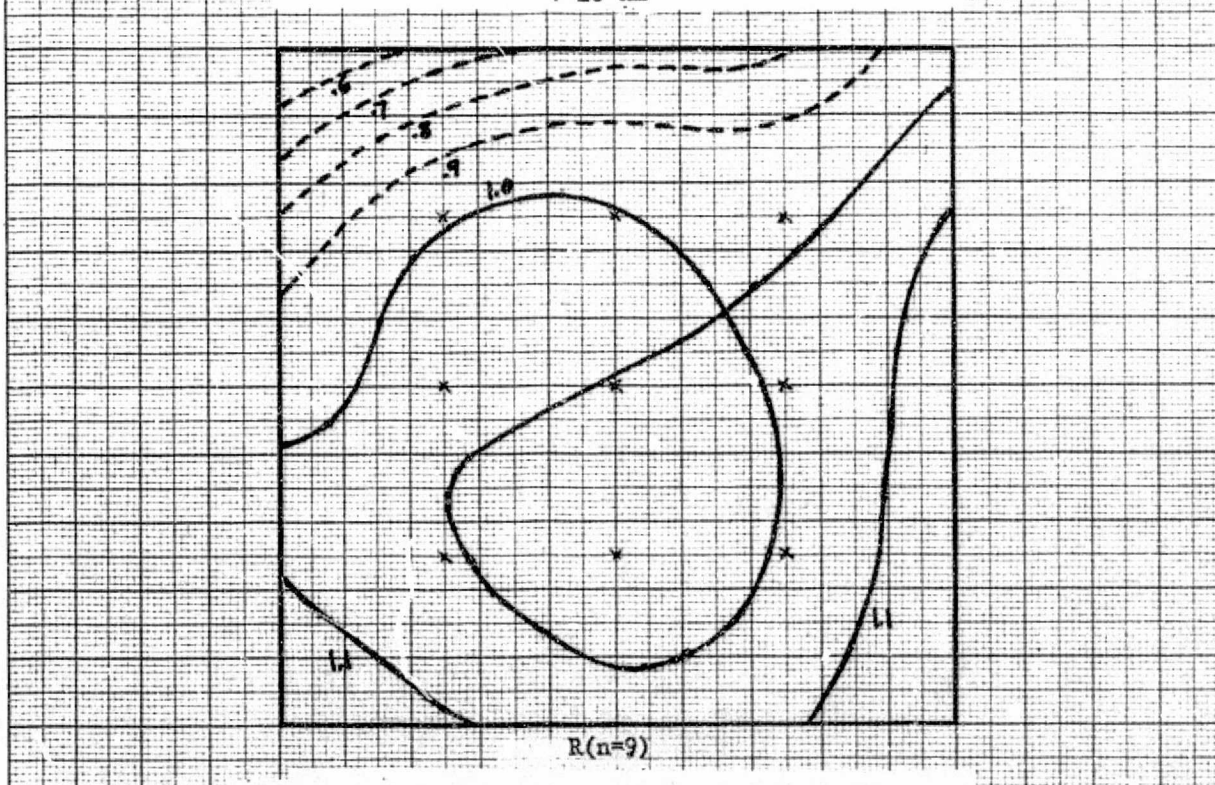


FIGURE 26b. Ratio Surface for "Asymmetric"
Atmosphere with Nine Sensors
 $V=10 \text{ km}$

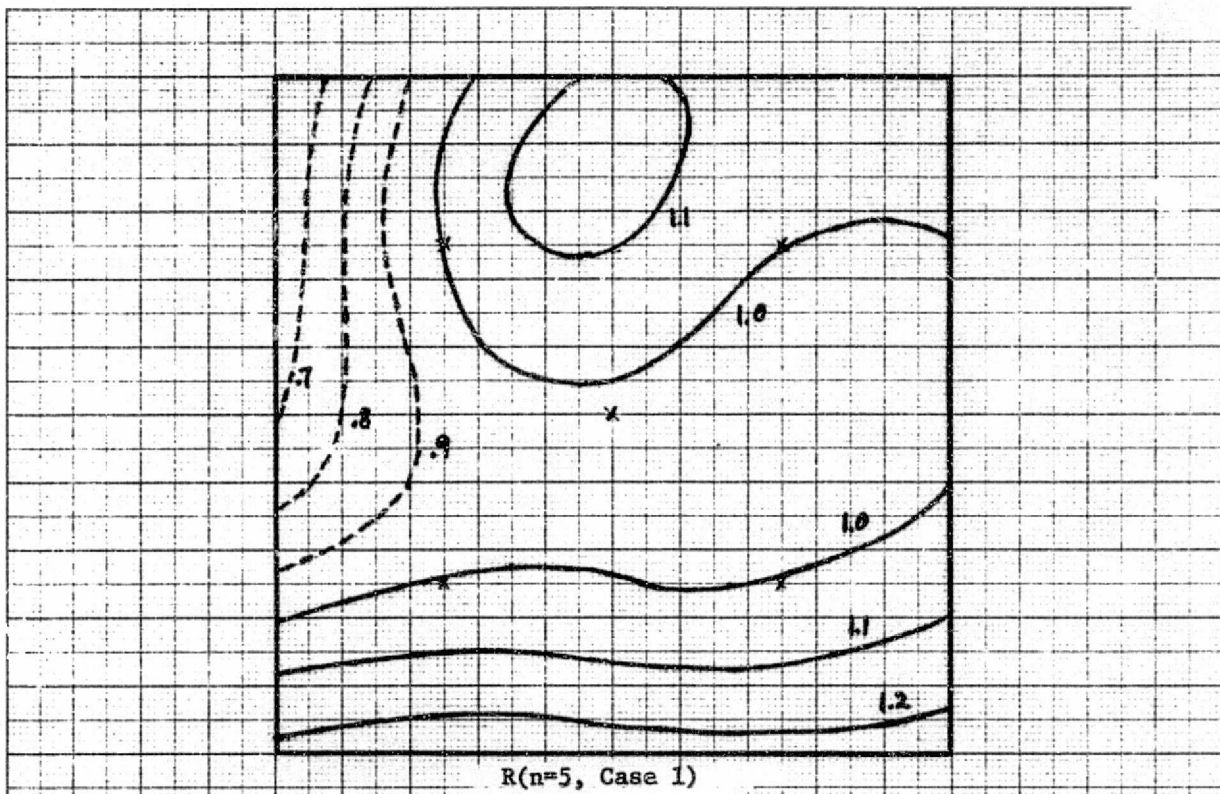


FIGURE 27a. Ratio Surface for "Asymmetric"
Surface with Five Sensors
 $V=10$ km

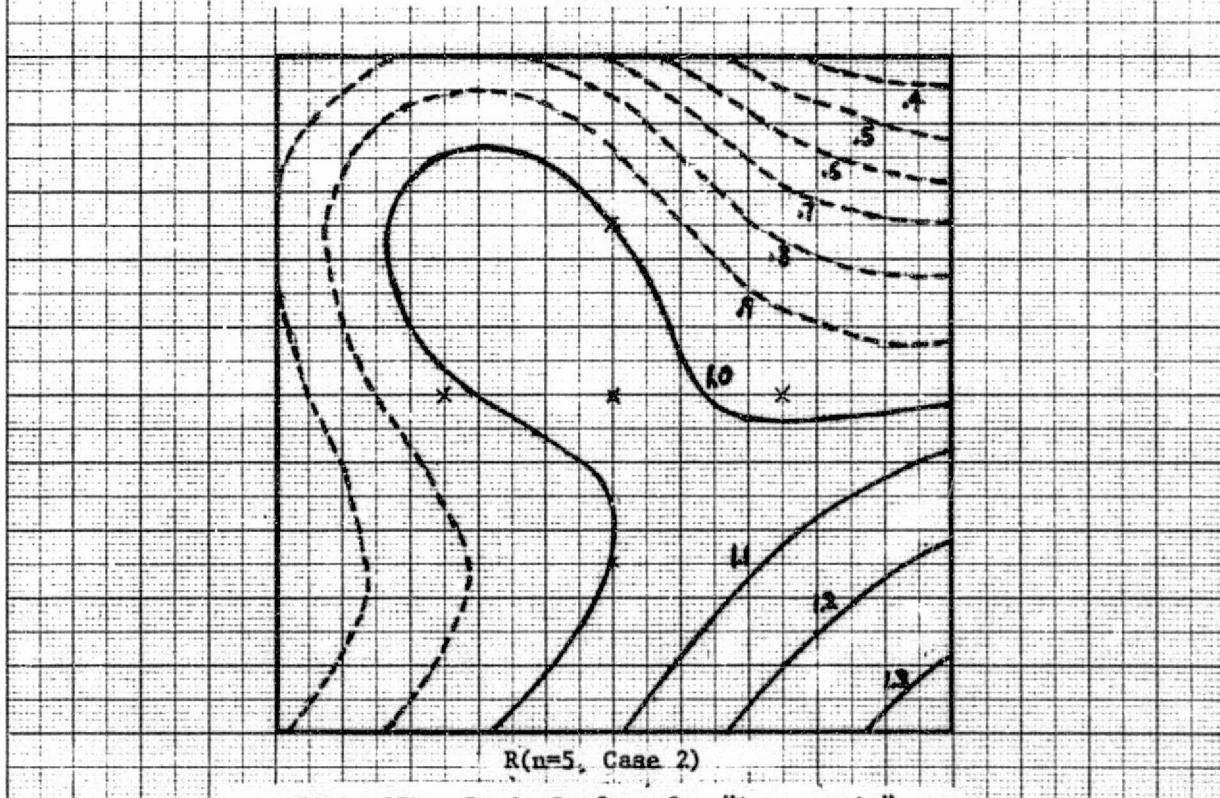


FIGURE 27b. Ratio Surface for "Asymmetric"
Surface with Five Sensors
 $V=10$ km

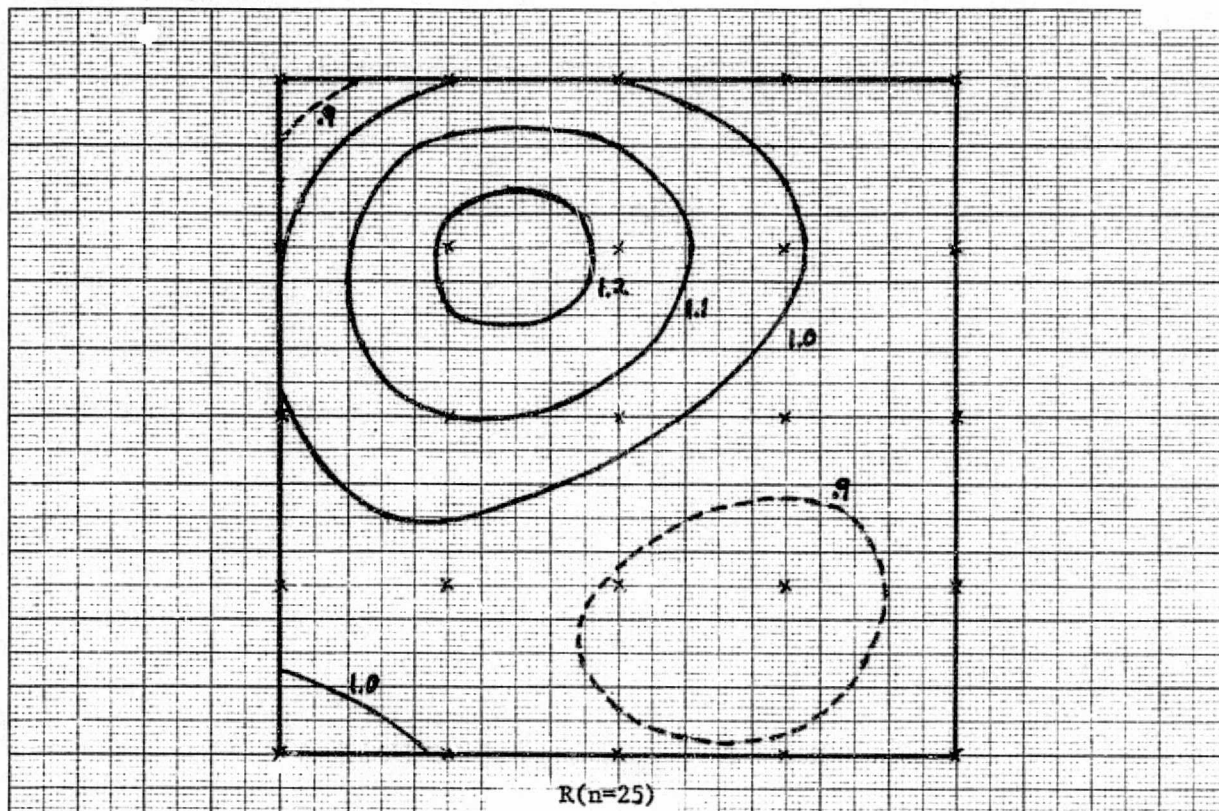


FIGURE 28. Ratio Surface for "Asymmetric"
Surface with 25 Sensors.
 $V=10 \text{ km}$

of symmetry may not be required, however, if we can use higher order regression surfaces. In general, we should be able to improve the contours by using a very high order surface but there remains the problem of using that surface outside the convex region bounded by the sensors.

Also, we need to investigate a spatial variation of the surface albedo along with an atmospheric variation. The change in ω_o , the single-scattering albedo should also be studied.

For rapid computer processing of actual data we need a more efficient method than the evaluation of R and S correction functions for each pixel. Therefore, instead of determining τ_o , $\bar{\rho}$, and ω_o surfaces and then calculating the R and S functions we can determine irradiance, path radiance, and total radiance surfaces by regression analysis using sensor sample points. This should decrease the processing time considerably.

3.5 CLASSIFICATION ACCURACY

In this section we shall determine the classification accuracy for a realistic scene with variable atmospheres. We shall first consider the effect of a horizontally inhomogeneous atmosphere on the classification accuracy when using typical spectral signatures. Actually, there are two effects attributable to the atmosphere which can cause a change in the classification accuracy and they may or may not be separate. If the atmosphere is constant in the horizontal plane then there can only be a mixing of the signatures as a result of surface radiation from elements outside the sensor's field of view being scattered by the atmosphere into the field of view. This effect which we shall call the interference effect will be treated in considerable detail in the next section.

In the more general case of a variable atmosphere the radiance may change throughout the entire scene as a result of the interference effect mentioned above and also because the atmosphere over a given target is quite different from point to point within the scene. For purposes of clarity we shall neglect the interference part of the atmosphere here and consider variations due to horizontal changes in the atmospheric state.

A spatially constant atmosphere produces no change in the spectral transmittance, spectral irradiance, and the spectral path radiance, i.e.,

$$L(x,y,z,\mu,\phi) = L_o(x,y,\mu,\phi) T(z,\mu) + L_p(z,\mu,\phi) \quad (32)$$

where $L_o(x,y,\mu,\phi)$ is the spectral radiance of the target at the surface point (x,y) ; $T(z,\mu)$ is the spectral transmittance from the surface to the altitude z ; and $L_p(z,\mu,\phi)$ is the spectral path radiance at altitude z .

The view angles are $\theta (= \cos^{-1} \mu)$, measured from the nadir, and ϕ , the azimuth angle between the view plane and the solar plane. Thus, if we neglect the atmospheric interference effect then the only effect of a constant atmosphere is to decrease the intrinsic target radiance and increase the path radiance. For a spatially variable atmosphere we have for the sensor radiance

$$L(x, y, z, \mu, \phi) = L_o(x, y, \mu, \phi) T(x, y, z, \mu, \phi) + L_p(x, y, z, \mu, \phi) \quad (33)$$

where the transmittance and path radiance are now dependent upon the position in the plane. The surface target radiance $L_o(x, y, \mu, \phi)$ will vary not only because of the intrinsic change in surface materials with distance but also because the irradiance falling upon the target is different due to the overlying variable atmosphere. For a wide range of atmospheric states, however, the irradiance changes very little and we will assume that it is constant throughout the entire scene.

We shall now consider some specific examples of the effect which variable atmospheres have on classification accuracy. The accuracy of classification can be measured by comparing actual data at a given point in a scene with a standard distribution obtained by generating the means, variances, and covariances of real data for known materials or classes. Real data were obtained from soybean and corn fields in Livingston Co., Illinois for an atmosphere which had an estimated visual range of 23 km. The means and standard deviations were determined and 25 data points were selected at random from the Gaussian distribution for each simulated field in the scene. The field configuration is illustrated in Fig. 29. In field C1 some of the sample points were closer to the mean value of soybeans than for corn and these were classified as soybeans. Most of the points (88%), however were classified as corn.

C1	S1	C2	S2	C3	S3	85.3% C 89.3% S
88%	92%	88%	84%	80%	92%	
S4	C4	S5	C5	S6	C6	90.7% C 89.3% S
88%	96%	96%	84%	84%	92%	
C7	S7	C8	S8	C9	S9	88.0% C 88.0% S
92%	88%	76%	92%	96%	84%	
S10	C10	S11	C11	S12	C12	92.0% C 85.3% S
88%	80%	80%	100%	88%	96%	
C13	S13	C14	S14	C15	S15	85.3% C 85.3% S
88%	84%	84%	92%	84%	80%	
S16	C16	S17	C17	S18	C18	84.0% C 85.3% S
84%	88%	92%	76%	80%	88%	

PATTERN OF SIMULATED CORN AND SOYBEAN FIELDS

Case 1: Uniform atmosphere, $V = 23$ km.
 87.6% of corn and 87.1% of soybeans recognized correctly.

FIGURE 29

The next case simulates a variable atmosphere in which the visual range changes from 23 km at the top of the scene to 13 km at the bottom of the scene, (Fig. 30). Each data point was then altered according to Eq. 33 and new classification accuracies were determined. This amounts to using the top row of fields ($V=23$ km) as training fields in order to determine the signatures. This time the percentage of classification changed slightly throughout the scene and in some cases actually increased. We then used signatures obtained from the entire scene instead of from the top row of fields. The classification accuracy is shown in Fig. 31 where we see little change from the previous case.

We then used an atmosphere in which the visual range changed from 23 km at the top to 8 km at the bottom. The same procedure was used as before and the resulting classification accuracies are shown in Figs. 32 and 33. Here we see a slightly greater change in the percent classification accuracy.

All these results can be summarized by a histogram plot of the number of fields with a given classification accuracy. This is illustrated in Fig. 34 for the three cases considered. It is clear that the distribution peaks more strongly as we go to clearer atmospheres, i.e., the recognition decreases for hazy, variable atmospheres.

It should be realized that no correlation was used in the above analysis, i.e., it was assumed that the soybean and corn fields were statistically independent. Also, a steeper atmospheric gradient could exist in reality and absorption by particulates should be considered. Also, as we shall see in the next section the interference between scenes caused by the scattering of radiation can be significant. This effect has not been included in the above analysis. Although the change in irradiance is small, the corresponding change in classification accuracy if this effect were included could be significant.

C1	S1	C2	S2	C3	S3	85.3% C 90.7% S
88%	92%	88%	84%	80%	96%	
S4	C4	S5	C5	S6	C6	89.3% C 89.3% S
88%	96%	96%	84%	84%	88%	
C7	S7	C8	S8	C9	S9	84.0% C 90.7% S
84%	88%	72%	96%	96%	88%	
S10	C10	S11	C11	S12	C12	92.0% C 86.7% S
88%	80%	84%	100%	88%	96%	
C13	S13	C14	S14	C15	S15	82.7% C 89.3% S
84%	88%	84%	96%	80%	84%	
S16	C16	S17	C17	S18	C18	84.0% C 88.0% S
88%	88%	92%	76%	84%	88%	

PATTERN OF SIMULATED CORN AND SOYBEAN FIELDS

Case 2a: Non-uniform atmosphere, $V = 23 \text{ km}$ (at top) to 13 km (at bottom).
 86.2% of corn and 89.1% of soybeans recognized correctly.
 Signatures obtained from $V = 23 \text{ km}$ data set.

FIGURE 30

C1	S1	C2	S2	C3	S3	88.0% C
92%	92%	88%	84%	84%	96%	90.7% S
S4	C4	S5	C5	S6	C6	90.7% C
88%	96%	96%	84%	84%	92%	89.3% S
C7	S7	C8	S8	C9	S9	86.7% C
88%	88%	76%	96%	96%	80%	88.0% S
S10	C10	S11	C11	S12	C12	92.0% C
88%	80%	80%	100%	88%	96%	85.3% S
C13	S13	C14	S14	C15	S15	84.0% C
84%	88%	84%	92%	84%	80%	86.7% S
S16	C16	S17	C17	S18	C18	84.0% C
88%	88%	92%	76%	80%	88%	86.7% S

PATTERN OF SIMULATED CORN AND SOYBEAN FIELDS

Case 2b: Non-uniform atmosphere, $V = 23 \text{ km}$ (at top) to 13 km (at bottom).
 87.6% of corn and 87.8% of soybeans recognized correctly.
 Signatures obtained from this data set.

FIGURE 31

C1	S1	C2	S2	C3	S3	
88%	92%	88%	84%	80%	96%	85.3% C 90.7% S
S4	C4	S5	C5	S6	C6	
88%	96%	96%	80%	84%	92%	89.3% C 89.3% S
C7	S7	C8	S8	C9	S9	
88%	88%	68%	96%	96%	84%	84.0% C 89.3% S
S10	C10	S11	C11	S12	C12	
92%	76%	84%	100%	92%	96%	90.7% C 89.3% S
C13	S13	C14	S14	C15	S15	
72%	96%	76%	96%	80%	84%	76.0% C 92.0% S
S16	C16	S17	C17	S18	C18	
96%	76%	100%	64%	88%	89%	76.0% C 94.7% S

PATTERN OF SIMULATED CORN AND SOYBEAN FIELDS

Case 3a: Non-uniform atmosphere, $V = 23 \text{ km}$ (at top) to 8 km (at bottom).
 83.6% of corn and 90.9% of soybeans recognized correctly.
 Signatures obtained from $V = 23 \text{ km}$ data set.

FIGURE 32

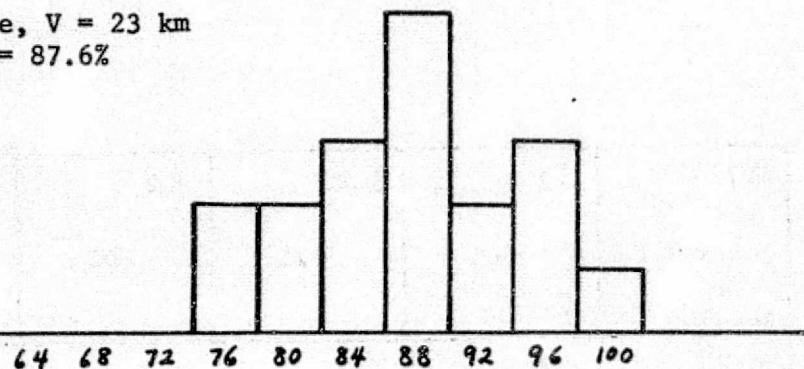
C1	S1	C2	S2	C3	S3	
92%	96%	92%	80%	84%	96%	89.3% C 90.7% S
S4	C4	S5	C5	S6	C6	88.0% C 89.3% S
88%	96%	96%	80%	84%	88%	
C7	S7	C8	S8	C9	S9	88.0% C 88.0% S
88%	88%	80%	96%	96%	80%	
S10	C10	S11	C11	S12	C12	92.0% C 84.0% S
84%	80%	80%	100%	88%	96%	
C13	S13	C14	S14	C15	S15	84.0% C 85.3% S
84%	84%	84%	92%	84%	80%	
S16	C16	S17	C17	S18	C18	84.0% C 89.3% S
92%	88%	92%	76%	84%	88%	

PATTERN OF SIMULATED CORN AND SOYBEAN FIELDS

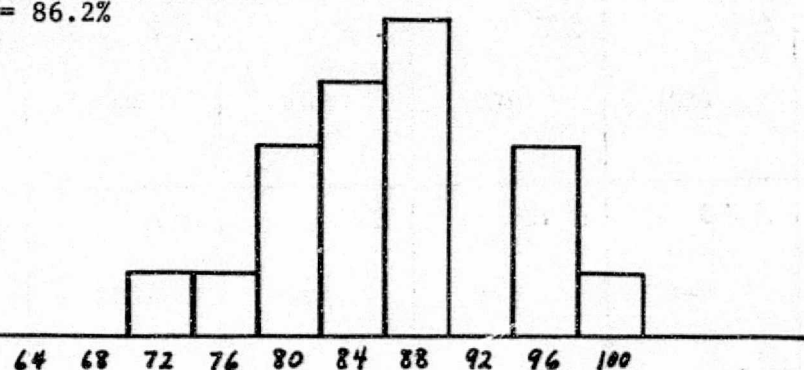
Case 3b: Non-uniform atmosphere, $V = 23 \text{ km (at top) to } 8 \text{ km (at bottom)}$.
 87.6% of corn and 87.8% of soybeans recognized correctly.
 Signatures obtained from this data set.

FIGURE 33

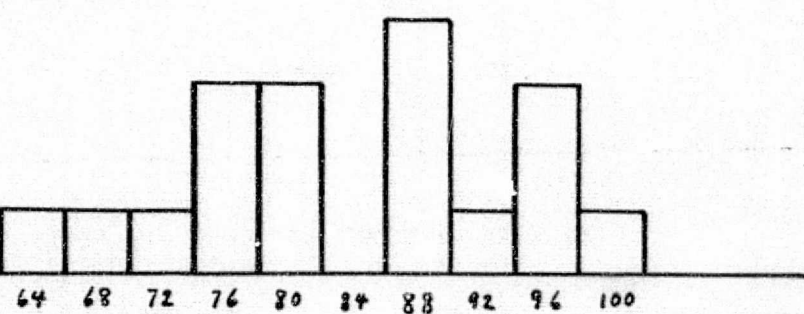
Case 1: Uniform atmosphere, $V = 23$ km
Mean recognition = 87.6%



Case 2: Non-uniform atmosphere, $13 \leq V \leq 23$ km
Mean recognition = 86.2%



Case 3: Non-uniform atmosphere, $8 \leq V \leq 23$ km
Mean recognition = 83.6%



NUMBER OF FIELDS VERSUS CLASSIFICATION ACCURACY

FIGURE 34

TARGET-BACKGROUND INTERACTION

In this section we shall consider an atmospheric effect which under certain circumstances can be more important in multispectral data processing than the spatial variation of the atmosphere treated in the previous section. It has been noted, Nalepka et al. [8], that there is an influence of the background on the target. Such an effect is to be expected, particularly for hazy atmospheric conditions since radiation reflected from surfaces outside of the instantaneous field of view will eventually find its way into the sensor as a result of atmospheric scattering. In this section we are concerned with the quantitative determination of this interaction effect.

4.1 THE GENERAL EQUATION

In a mathematical analysis of a problem as complex as the transfer of radiation through a medium with inhomogeneous boundary conditions it is important that one analyze carefully the mathematical procedures to be used so as to understand the limitations of a model based upon these calculations.

The general equation which is used to describe the spectral radiance at a sensor is

$$L = L_o T + L_p \quad (34)$$

where L_o is the radiance at the target in the direction of the sensor, T is the transmittance between the target and sensor, and L_p is the path

[8] R. F. Nalepka, H. M. Horwitz, N. S. Thomson, Report No. 31650-30-T, Willow Run Laboratories, The University of Michigan, Ann Arbor, 1971.

radiance, which is the result of radiation having been scattered by the atmosphere into the direction of the sensor. In a detailed analysis of path radiance as we shall undertake in this section it is desirable to subdivide this term into additional parts, i.e.,

$$L_p = L_{p_o} + L_{p_t} + L_{p_s} \quad (35)$$

where L_{p_o} is that component which represents all multiply scattered radiation which has never reached the surface, L_{p_t} is the component that represents radiation originating (by reflection) from the target and being scattered by the atmosphere one or more times. The average of this component over the solid angle of the sensor can be considered as a part of the target radiance. Finally, L_{p_s} is the path radiance component arising from radiation originating from the background elements and being scattered one or more times. These components are illustrated in Fig. 35 for the case of single scattering.

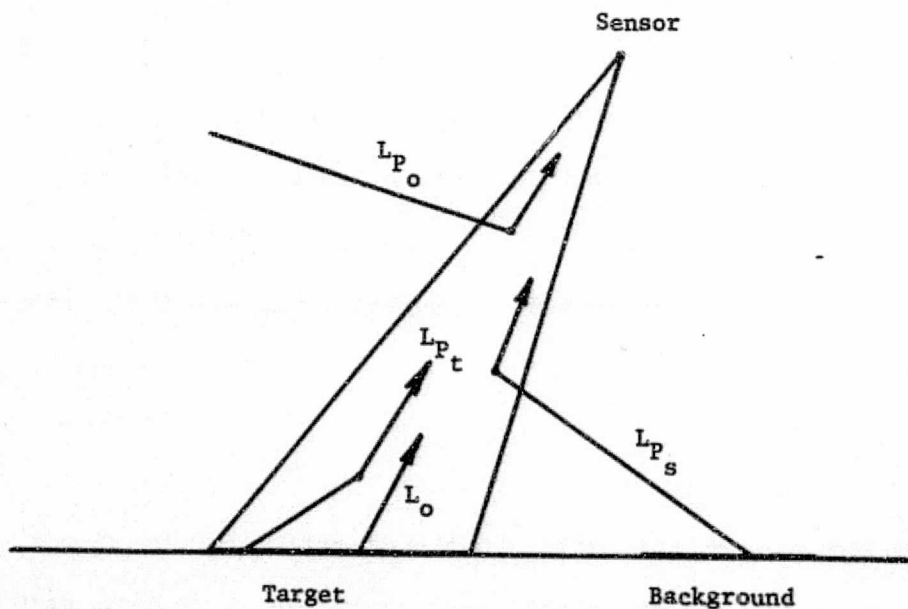


FIGURE 35. RADIANCE COMPONENTS IN A SCATTERING ATMOSPHERE

The radiance at the surface, L_o , is not independent of the atmosphere.

In fact, it depends on the overlying medium in the following way

$$L_o(\hat{\Omega}) = \int \hat{\Omega} \rho(\hat{\Omega}, \hat{\Omega}') \left[L_{\text{solar}}(\hat{\Omega}') + L_{\text{sky}}(\hat{\Omega}') \right] d\hat{\Omega}' \quad (36)$$

where $\rho(\hat{\Omega}, \hat{\Omega}')$ is the bidirectional reflectance of the surface and $L_{\text{solar}}(\hat{\Omega})$ and $L_{\text{sky}}(\hat{\Omega})$ are the solar and sky radiances at the ground. $\hat{\Omega}'$ and $\hat{\Omega}$ are the incoming and outgoing directions of the radiation. If we have a Lambertian (perfectly diffuse) surface then the surface radiance is given by

$$L_o = \frac{\rho}{\pi} E \quad (37)$$

where ρ is the direction independent hemispherical reflectance (albedo) and E is the total downwelling spectral irradiance on the target.

The pure atmospheric path radiance L_p and the irradiance E will be calculated according to the usual radiative-transfer model. The primary dependence of the total radiance L on an inhomogeneous surface arises from path radiance terms L_{p_t} and L_{p_s} . It is the determination of these components which will be the object of our mathematical analysis.

4.2 MULTI-DIMENSIONAL RADIATIVE-TRANSFER

If the atmosphere has spatial variations but has a uniform surface we must have an inhomogeneous equation with inhomogeneous boundary conditions. On the other hand, for a uniform atmosphere and a non-uniform surface we also have an inhomogeneous equation with inhomogeneous boundary conditions. We shall specialize our analysis to consider a time-independent, spatially uniform medium in the horizontal plane bounded by a non-uniform Lambertian surface.

4.2.1 THE TRANSFER EQUATION

We shall consider a transport equation

$$HL(\hat{r}, \hat{\Omega}, t) = Q(\hat{r}, \hat{\Omega}, t) \quad (38)$$

where $L(\hat{r}, \hat{\Omega}, t)$ is the spectral radiance at position \hat{r} with direction $\hat{\Omega}$ at time t and $Q(\hat{r}, \hat{\Omega}, t)$ is the source of radiation. H is a linear Boltzmann operator given by

$$H \equiv \frac{1}{c} \frac{\partial}{\partial t} + \hat{\Omega} \cdot \nabla + \kappa(\hat{r}, \hat{\Omega}) - \frac{\beta(\hat{r}, \hat{\Omega})}{4\pi} \int_{\hat{\Omega}'} p(\hat{r}, \hat{\Omega}, \hat{\Omega}') d\hat{\Omega}' \quad (39)$$

where $\kappa(\hat{r}, \hat{\Omega})$ and $\beta(\hat{r}, \hat{\Omega})$ are the extinction and scattering coefficients and $p(\hat{r}, \hat{\Omega}, \hat{\Omega}')$ is the phase function. We will not go into the details of the interesting symmetry properties of the transport equation but refer the reader to Case and Zweifel [9] for such explanations. If we have time independence and an isotropic, rotationally invariant medium then the radiative-transfer equation is

$$\hat{\Omega} \cdot \nabla L(\hat{r}, \hat{\Omega}) + \kappa(\hat{r})L(\hat{r}, \hat{\Omega}) - \frac{\beta(\hat{r})}{4\pi} \int_{\hat{\Omega}'} p(\hat{r}, \hat{\Omega}, \hat{\Omega}') L(\hat{r}, \hat{\Omega}') d\hat{\Omega}' = Q(\hat{r}, \hat{\Omega}) \quad (40)$$

where $Q(\hat{r}, \hat{\Omega})$ is the distributed source. For a monodirectional point source of unit strength we have

$$Q(\hat{r}, \hat{\Omega}) = \delta(\hat{r} - \hat{r}_o) \delta(\hat{\Omega} - \hat{\Omega}_o) \quad (41)$$

We consider the adjoint equation formed by replacing $\hat{\Omega}$ and $\hat{\Omega}'$ with their time reversed states, i.e.,

$$-\hat{\Omega} \cdot \nabla \tilde{L}(\hat{r}, -\hat{\Omega}) + \kappa(\hat{r}) \tilde{L}(\hat{r}, -\hat{\Omega}) - \frac{\beta(\hat{r})}{4\pi} \int_{\hat{\Omega}'} p(\hat{r}, \hat{\Omega}, \hat{\Omega}') \tilde{L}(\hat{r}, -\hat{\Omega}') d\hat{\Omega}' = \tilde{Q}(\hat{r}, -\hat{\Omega}) \quad (42)$$

where $\tilde{L}(\hat{r}, -\hat{\Omega})$ is the adjoint of $L(\hat{r}, \hat{\Omega})$.

[9] K. M. Case and P. F. Zweifel, Linear Transport Theory, Addison-Wesley Publishing Co., 1967.

4.2.2 GENERAL SOLUTION

The solution of the transport equation can be found by multiplying the transport equation by $\tilde{L}(\hat{r}, -\hat{\Omega})$, the adjoint equation by $L(\hat{r}, \hat{\Omega})$, subtracting and applying Gauss' theorem, i.e.,

$$\int_V \nabla \cdot \hat{U} dV = - \int_A \hat{n}_i \cdot \hat{U} dA \quad (43)$$

where V is a volume, A is the surface area and \hat{n}_i is the unit normal vector.

If we let

$$\tilde{L}(\hat{r}, \hat{\Omega}) = \tilde{G}(\hat{r}, \hat{\Omega}; \hat{r}_o, \hat{\Omega}_o) \quad (44)$$

and

$$\tilde{Q}(\hat{r}, \hat{\Omega}) = \delta(\hat{r} - \hat{r}_o) \delta(\hat{\Omega} - \hat{\Omega}_o) \quad (45)$$

where $\tilde{G}(\hat{r}, \hat{\Omega}; \hat{r}_o, \hat{\Omega}_o)$ is the adjoint Green's function, then using the reciprocity relations for Green's functions we then find the general solution to be the following:

$$\begin{aligned} L(\hat{r}, \hat{\Omega}) &= \int_V \int_{\hat{\Omega}} G(\hat{r}, \hat{\Omega}; \hat{r}', \hat{\Omega}') Q(\hat{r}', \hat{\Omega}') d\hat{r}' d\hat{\Omega}' \\ &+ \int_A \int_{\hat{\Omega}} G(\hat{r}, \hat{\Omega}; \hat{R}', \hat{\Omega}') \hat{n}_i(\hat{R}') \cdot \hat{\Omega}' L(\hat{R}', \hat{\Omega}') dA d\hat{\Omega}' \end{aligned} \quad (46)$$

It should be noted that $Q(\hat{r}, \hat{\Omega})$ is the distributed volume source and $L(\hat{R}, \hat{\Omega})$ is the radiance on the surface. Hence, Eq. (46) is the general solution of the radiative transfer equation of any distribution of sources within or on the boundary of the medium. The main problem then, is to determine the volume and surface Green's functions.

4.2.3 GREEN'S FUNCTION

The radiative-transfer equation that we must solve is the following:

$$\hat{\Omega} \cdot \nabla L(x, y, z, \mu, \phi) + \kappa(z) L(x, y, z, \mu, \phi) - \frac{\beta(z)}{4\pi} \int_0^{2\pi} \int_{-1}^1 p(z, \mu, \phi, \mu', \phi') L(x, y, z, \mu', \phi') d\mu' d\phi' = Q(x, y, z, \mu, \phi) \quad (47)$$

where $\theta (= \cos^{-1} \mu)$ and ϕ are the usual spherical coordinates of polar (or zenith) angle and azimuthal angle respectively. In order to find the solution $L(x, y, z, \mu, \phi)$ for the distributed source $Q(x, y, z, \mu, \phi)$, we must first determine the Green's function which is a solution of the following equation:

$$\hat{\Omega} \cdot \nabla G(x, y, z, \mu, \phi) + \kappa(z) G(x, y, z, \mu, \phi) - \frac{\beta(z)}{4\pi} \int_0^{2\pi} \int_{-1}^1 p(z, \mu, \phi, \mu', \phi') G(x, y, z, \mu', \phi') d\mu' d\phi' = \delta(x - x_o) \delta(y - y_o) \delta(z) \delta(\mu - \mu_o) \delta(\phi - \phi_o) \quad (48)$$

where $(x_o, y_o, 0)$ are the coordinates of the surface source and $\theta_o (= \cos^{-1} \mu_o)$ and ϕ_o are the corresponding angles for the monodirectional source. Since we have homogeneity in the x-y plane we can use the two-dimensional Fourier transform, i.e.,

$$\bar{G}(k, \ell, z, \mu, \phi) = \int_{-\infty}^{\infty} \int_{-\infty}^{\infty} e^{i(kx + \ell y)} G(x, y, z, \mu, \phi) dx dy \quad (49)$$

and an inverse,

$$G(x, y, z, \mu, \phi) = \frac{1}{(2\pi)^2} \int_{-\infty}^{\infty} \int_{-\infty}^{\infty} e^{-i(kx + \ell y)} \bar{G}(k, \ell, z, \mu, \phi) dk d\ell \quad (50)$$

Taking the Fourier transform of Eq. (48) and finding the formal solution we get for the general Green's function transform

$$\begin{aligned}
 \bar{G}(k, \ell, z, \mu, \phi) = & \frac{e^{-[\tau_0 - \tau(z)]/\mu}}{\mu} e^{i[x_0 + \frac{\sqrt{1-\mu^2}}{\mu} z \cos \phi] k} e^{i[y_0 + \frac{\sqrt{1-\mu^2}}{\mu} z \sin \phi] \ell} \delta(\mu - \mu_0) \delta(\phi - \phi_0) \\
 & + \frac{1}{4\pi\mu} \int_0^z \int_0^{2\pi} \int_{-1}^1 \beta(z') e^{-[\tau(z') - \tau(z) - i\lambda(z-z')] / \mu} p(z', \mu, \phi, \mu', \phi') \bar{G}(k, \ell, z, \mu', \phi') d\mu' d\phi' dz'
 \end{aligned} \tag{51}$$

where $\lambda = \sqrt{1-\mu^2} [k \cos \phi + \ell \sin \phi]$.

4.2.4 SINGLE-SCATTERING

Equation (51) is an integral equation for the transformed Green's function. It represents a complete solution with an infinite number of scatterings for a monodirectional point source. Iterating once gives us the single-scattering solution for the transformed Green's function. Taking the inverse transform then gives us the solution, i.e.,

$$\begin{aligned}
 G_s(x, y, z, \mu, \phi; x_0, y_0, \mu_0, \phi_0) = & \frac{1}{4\pi\mu} \int_0^z \beta(z') \frac{p(z', \mu, \phi, \mu_0, \phi_0)}{\mu_0} e^{-[\tau(z') - \tau(z)] / \mu} e^{-[\tau_0 - \tau(z')] / \mu_0} \\
 & x \delta \left[x - x_0 - \frac{\sqrt{1-\mu_0^2}}{\mu_0} z' \cos \phi_0 - \frac{\sqrt{1-\mu^2}}{\mu} (z - z') \cos \phi \right] \delta \left[y - y_0 - \frac{\sqrt{1-\mu_0^2}}{\mu_0} z' \cos \phi_0 \right. \\
 & \left. - \frac{\sqrt{1-\mu^2}}{\mu} (z - z') \sin \phi \right] dz'.
 \end{aligned} \tag{52}$$

The geometry appropriate to Eq. (54) is illustrated in Fig. 36. An observer or sensor is located at point (x, y, z) and receiving direct radiation from the point $(x_s, y_s, 0)$ on the surface. Radiation also emanates from either a target or background point source designated by $(x_o, y_o, 0)$, is attenuated to point (x', y', z') , and is then scattered into the direction (θ, ϕ) and is attenuated to point (x, y, z) .

4.2.5 SURFACE PATH RADIANCE

Since we have no volume source of radiation we consider our only source to be the surface. Hence, the solution is

$$L_{p_s}(x, y, z, \mu, \phi) =$$

$$\int_{x_o} \int_{y_o} \int_0^{2\pi} \int_0^1 G_s(x, y, z, \mu, \phi; x_o, y_o, \mu_o, \phi_o) \mu_o L(x_o, y_o, \mu_o, \phi_o) d\mu_o d\phi_o dx_o dy_o \quad (53)$$

Inserting the singly-scattering Green's function and carrying out the integration over the angular coordinates we find the path radiance arising from the surface to be

$$L_{p_s}(x, y, z, \mu, \phi) = \frac{1}{4\pi\mu} \int_{x_o} \int_{y_o} \int_0^z \mu^{*3} \frac{\delta(z')}{z} p(z', \cos\chi) \\ x e^{-[\tau(z') - \tau(z)]/\mu} e^{-[\tau_o - \tau(z')]}/\mu^* L(x_o, y_o, \mu^*, \phi^*) dz' dx_o dy_o \quad (54)$$

where

$$\mu^* = \sqrt{\left[x - x_o + \frac{\sqrt{1-\mu^2}}{\mu} (z - z') \cos\phi \right]^2 + \left[y - y_o + \frac{\sqrt{1-\mu^2}}{\mu} (z - z') \sin\phi \right]^2 + z'^2} \quad (55)$$

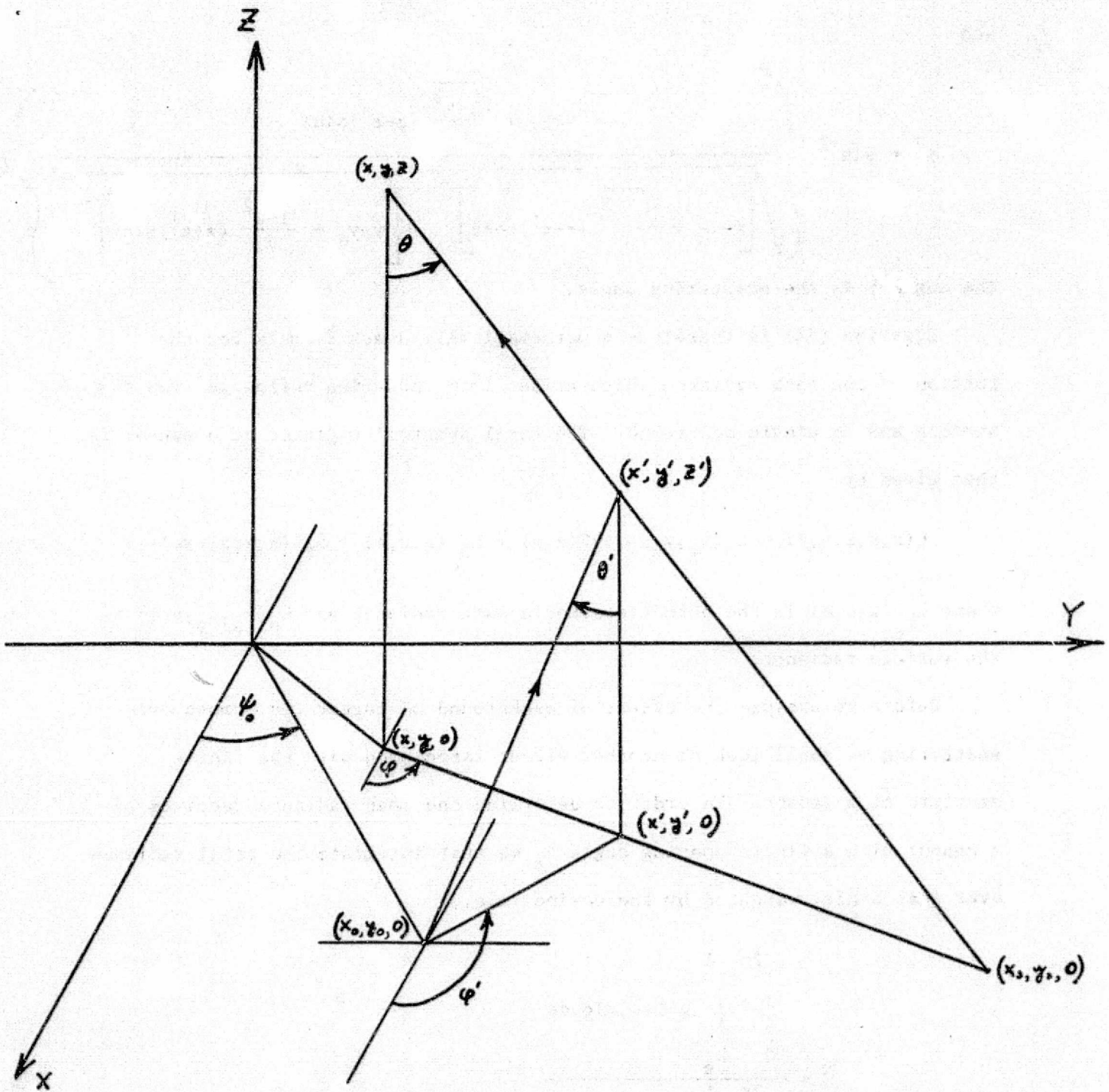


FIGURE 36. GEOMETRY FOR SINGLY SCATTERED SURFACE RADIATION

and

$$\phi^* = \sin^{-1} \left\{ \frac{y - y_o + \frac{\sqrt{1-\mu^2}}{\mu} (z - z') \sin \phi}{\sqrt{\left[x - x_o + \frac{\sqrt{1-\mu^2}}{\mu} (z - z') \cos \phi \right]^2 + \left[y - y_o + \frac{\sqrt{1-\mu^2}}{\mu} (z - z') \sin \phi \right]^2}} \right\} \quad (56)$$

The angle χ is the scattering angle.

Equation (54) is therefore a mathematically exact formula for that portion of the path radiance which arises from radiation reflected from the surface and is single-scattered. The total spectral radiance at a sensor is then given by

$$L(x, y, z, \mu, \phi) = L_o(x_s, y_s, \mu, \phi) T(z, \mu) + L_{p_o}(z, \mu, \phi) + L_{p_s}(x, y, z, \mu, \phi) \quad (57)$$

where $L_{p_o}(z, \mu, \phi)$ is the pure atmospheric path radiance and $L_o(x_s, y_s, \mu, \phi)$ is the surface radiance.

Before we analyze the effect of background on target via atmospheric scattering we shall look at another effect associated with the finite aperture of a sensor. In order to determine the mean radiance received by a sensor with a finite opening angle θ_s we must integrate the total radiance over that angle, weighted by the cosine, i.e.,

$$\bar{L} = \frac{\int_0^{2\pi} \int_{\mu_s}^1 \mu L(\mu, \phi) d\mu d\phi}{\int_0^{2\pi} \int_{\mu_s}^1 \mu d\mu d\phi} \quad (58)$$

The question arises, if θ_s ($=\cos^{-1}\mu_s$) is measured in milliradians how much does $L(\mu, \phi)$ differ from \bar{L} ? If part of the instantaneous field of view lies near a highly reflecting area then it is possible that a significant difference does occur. The various components of interest can be illustrated as in Figure 37.

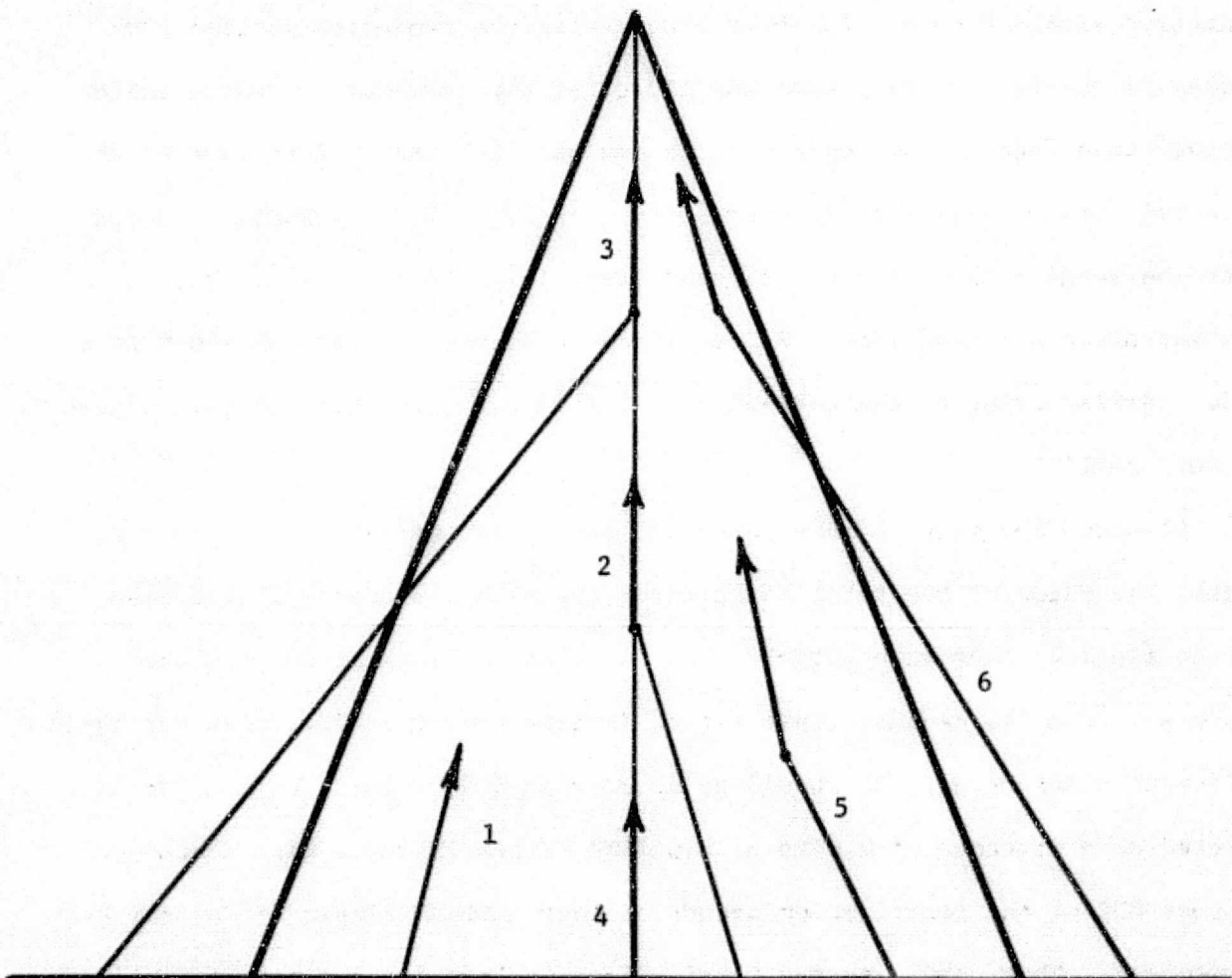
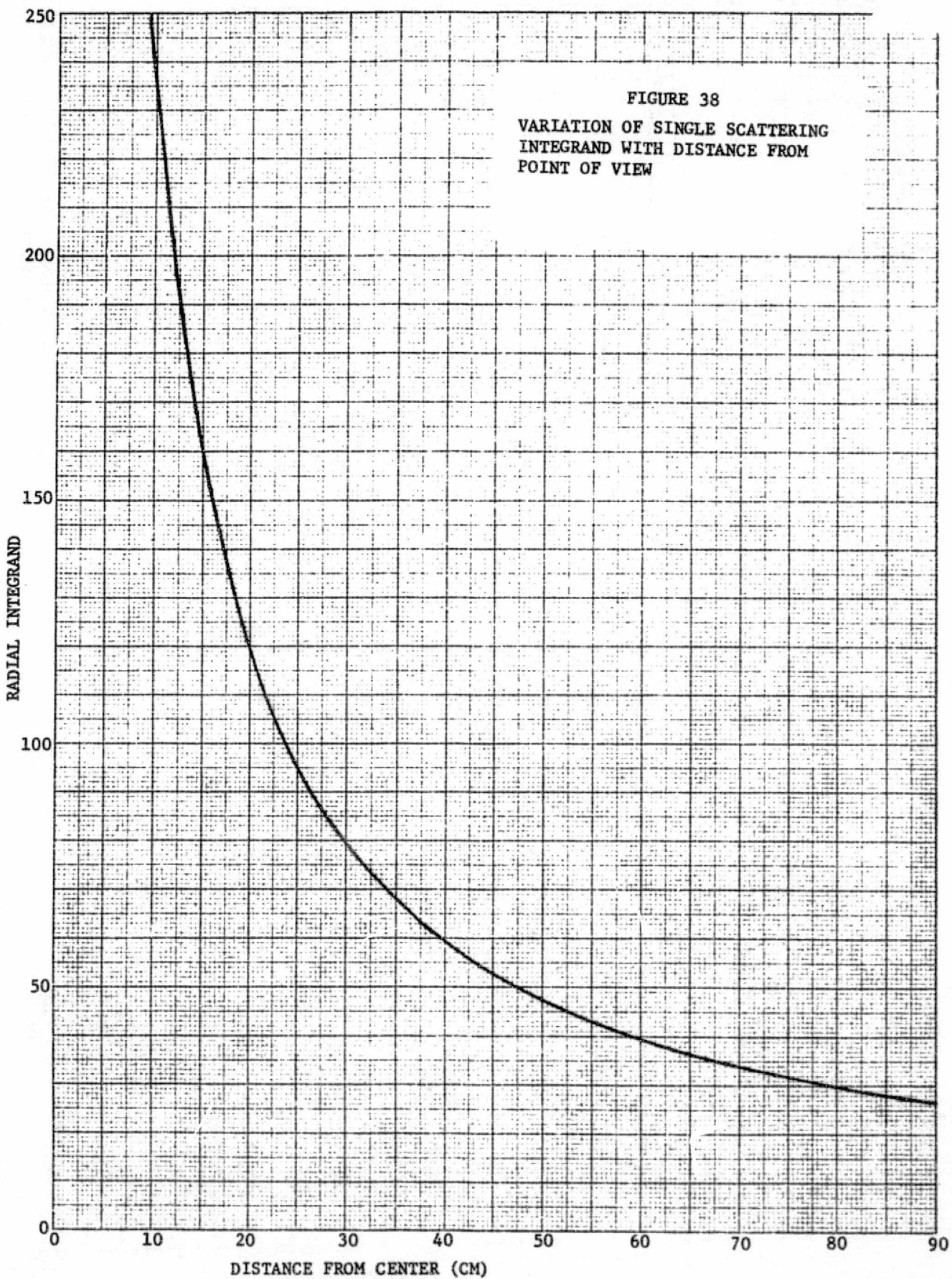


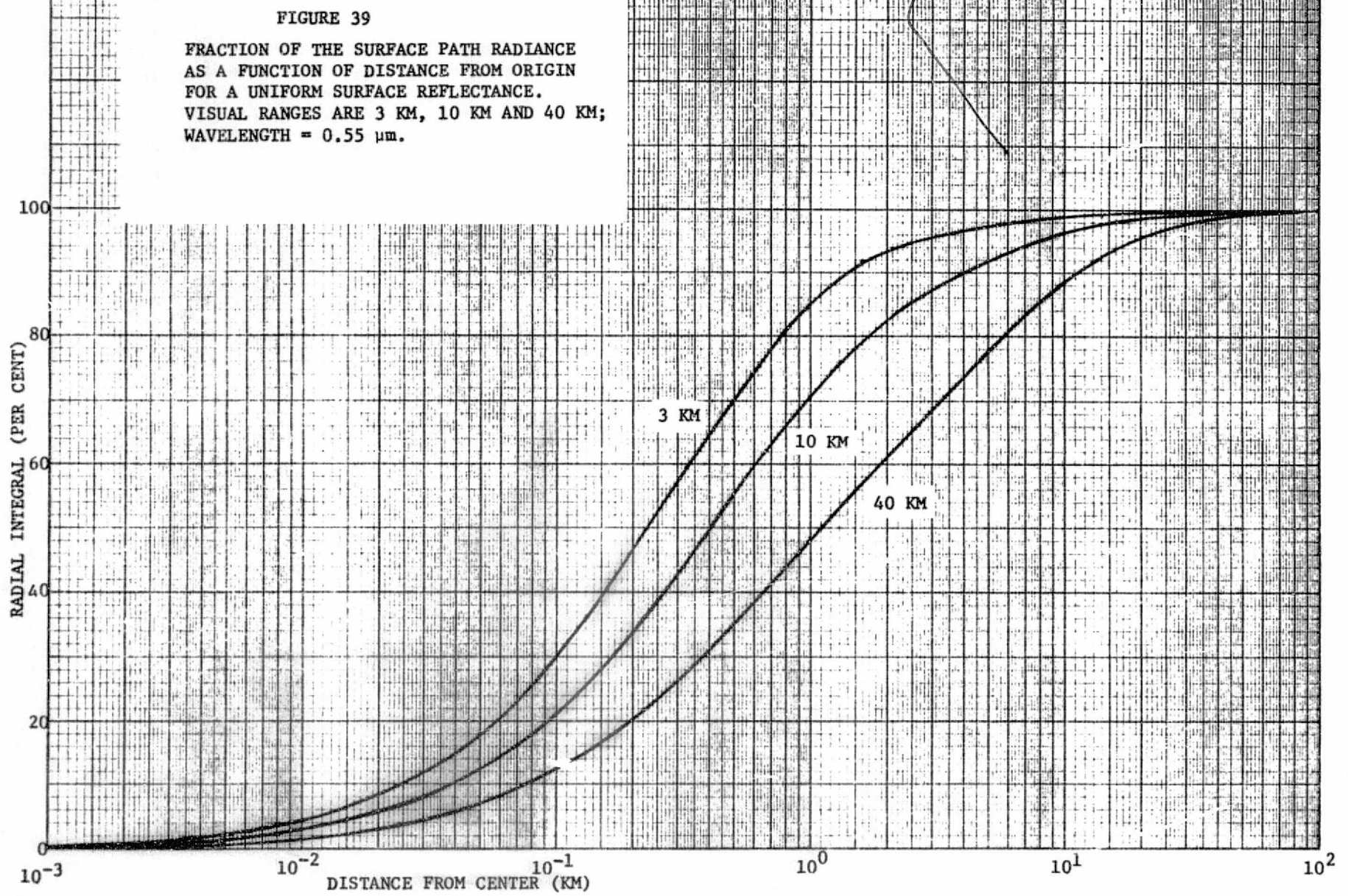
FIGURE 37. RADIANCE COMPONENTS FOR A FINITE APERTURE

In a previous study, Turner [2], it was assumed that all radiation from the surface was scattered along the direct ray from the center of a target to the sensor. This corresponds to components 1, 2, and 3 in Fig. (37). The first component is the directly attenuated radiation from the surface, the second is the singly-scattered radiation from the target, and the third is the singly-scattered radiation from the background. Likewise components 4, 5, and 6 are the corresponding components for radiation being singly-scattered within a cone. For hazy atmospheres the radiation is strongly peaked in the forward direction and therefore the radiance decreases quite rapidly as a function of angle. If we evaluate the radial integrand of the path radiance we find that it decreases as in Fig. 38. It should be noted that the largest part of the integrand lies within 80 cm or so of the instantaneous point of view. Hence, for a resolution element of ~80 m on a side, corresponding to the LANDSAT field of view we see that the edge effect is very small.

Although the value of the integrand decreases rapidly with increasing angle, the value of the total integral or the path radiance will increase due to the fact that more surface area is being included as the distance increases from the center. This effect is illustrated in Fig. (39) for three different atmospheres. It should be noted that 60% of the contribution is reached at a distance of 0.8 km or ten LANDSAT pixels for a hazy atmosphere whereas 60% of the contribution occurs at four LANDSAT pixels for a very hazy atmosphere. Thus, although the total effect is less for a clear atmosphere than for a hazy atmosphere it is necessary to go out to greater distances to obtain the same percentage contribution. This is due to the fact that the

[2] R. E. Turner, Radiative Transfer in Real Atmospheres, Report No. 190100-24-T, Environmental Research Institute of Michigan, Ann Arbor, 1974.





probability for scattering is less for a clear atmosphere but the probability that the radiation is scattered at a large angle is greater because of the smaller degree of anisotropy in the single-scattering phase function. This effect is illustrated in Fig. 40. Hence, the total effect of a background

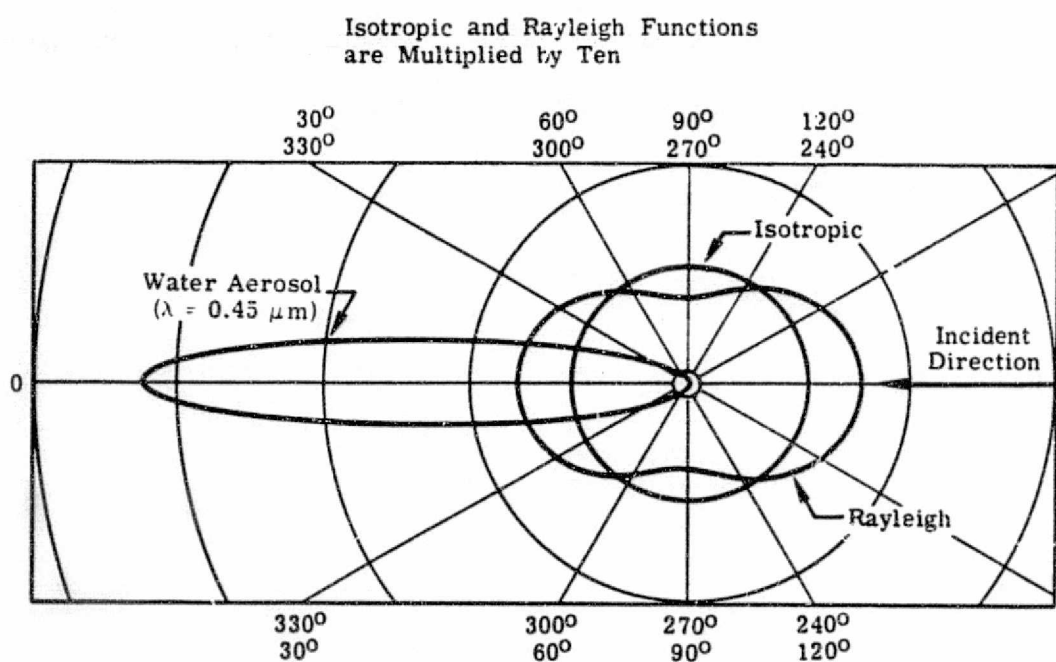


FIGURE 40 ANGULAR DEPENDENCE OF SINGLE-SCATTERING PHASE FUNCTIONS IN ANY AZIMUTHAL PLANE

is important and we should now consider a more realistic surface pattern characteristic of agricultural areas.

4.3 SIMULATION OF SATELLITE DATA

We shall now consider surface conditions which are more realistic than those used in Section 3. There we assumed a uniform surface with a background all composed of the same material. In this section we apply the mathematical

techniques of Green's functions in order to simulate satellite multispectral data appropriate to extended agricultural areas.

4.3.1 REFLECTANCE PATTERNS

Using the mathematical methods of the preceding section we can calculate the singly-scattered radiance from any complex pattern of reflectance elements. For computational simplicity, however, we shall consider a simple checkerboard pattern of square fields with the target being the center square. The radiance in a vertical direction at space altitudes is given by

$$L(x_f, y_f, \phi) = L_o(x_f, y_f, \phi) T + L_{P_o}(x_f, y_f, \phi) + L_{P_s}(x_f, y_f, \phi) \quad (59)$$

where (x_f, y_f) is a point within the target square. For homogeneous atmospheres

$$L_{P_o}(x_f, y_f, \phi) = L_{P_o}(\phi). \quad (60)$$

The surface path radiance, L_{P_s} is

$$L_{P_s}(x_f, y_f, \phi) = \int_{x_o} \int_{y_o} F(x_f, y_f, \phi, x_o, y_o) dx_o dy_o \quad (61)$$

where we must integrate over the entire surface, (x_o, y_o) being any point on the surface. The quantity $F(x_f, y_f, \phi, x_o, y_o)$ is given by

$$F(x_f, y_f, \phi, x_o, y_o) = \frac{1}{4\pi} \int_0^\infty \frac{\beta(z')}{z'^2} p(z', \phi, \mu^*, \phi^*) \mu^{*3} x e^{-[\tau(z') - \tau(z)]} e^{-[\tau_o - \tau(z')]/\mu^*} L_o(x_o, y_o, \mu^*, \phi^*) dz' \quad (62)$$

where

$$\mu^* = \frac{z'}{\sqrt{(x_f - x_o)^2 + (y_f - y_o)^2 + z'^2}} \quad (63)$$

$$\phi^* = \sin^{-1} \left\{ \frac{y_f - y_o}{\sqrt{(x_f - x_o)^2 + (y_f - y_o)^2 + z'^2}} \right\} \quad (64)$$

In the case of Lambertian surfaces

$$L_o = \frac{\rho_{ij} \mu_s E}{\pi} \quad (65)$$

where ρ_{ij} is the reflectance of the (i,j) square, μ_s is the cosine of the solar zenith angle, and E is the irradiance. The surface path radiance is therefore given by

$$L_p(\phi) = \sum_{i=1}^N \sum_{j=1}^N \rho_{ij} I_{ij} \quad (66)$$

when I_{ij} is the integral over the (i,j) square. It should be noted that the integrals I_{ij} are independent of reflectance so that the lengthy computations for these integrals need only be done once for a specific set of wavelengths, atmospheric states, and field sizes. Any number of reflectance patterns may then be considered by multiplying each ρ_{ij} by each I_{ij} . If we look at the origin of coordinates, i.e., at the center of the target square, then by symmetry

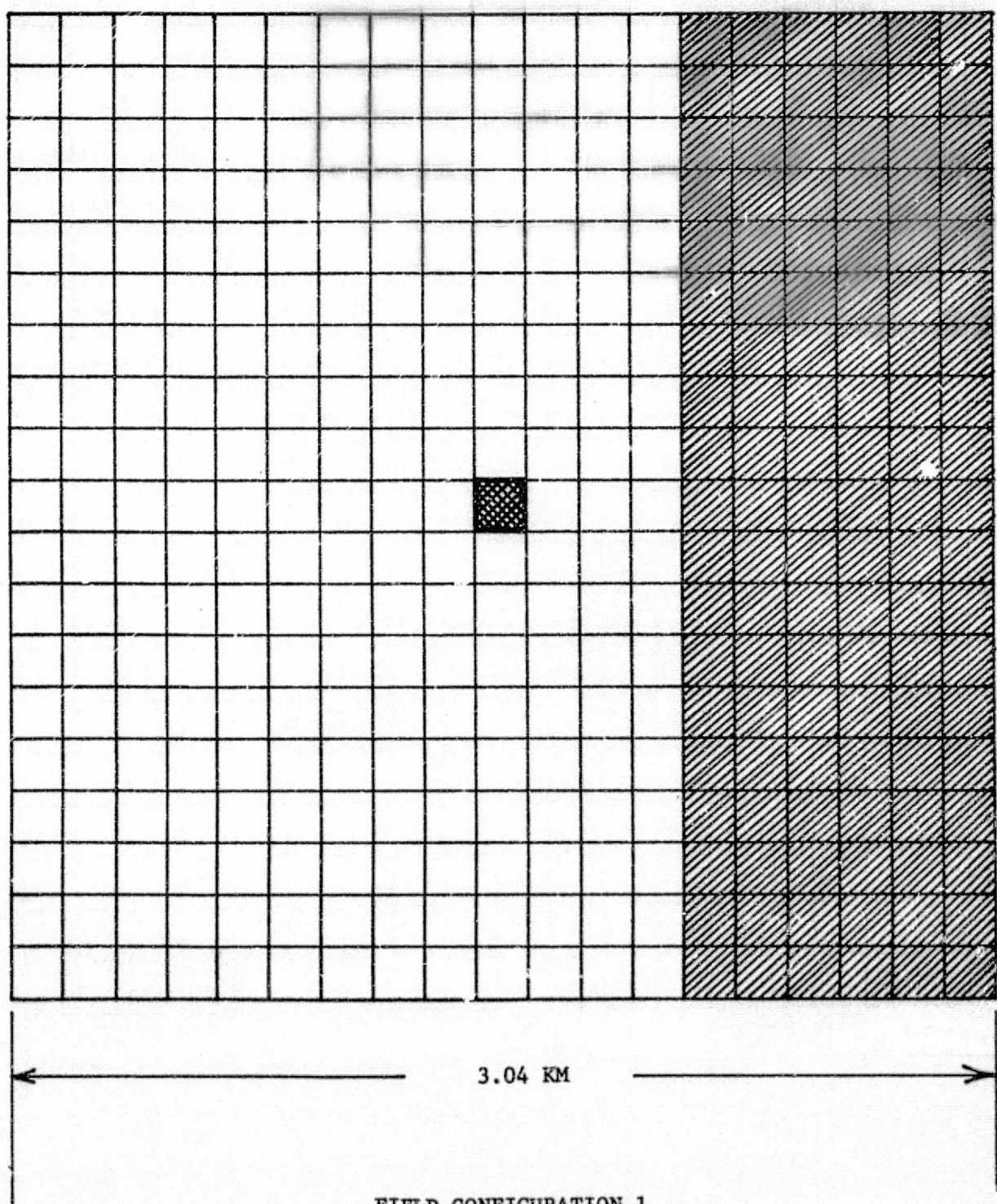
$$L_p = \rho_{oo} I_{oo} + [\rho_{i,j} + \rho_{j,i} + \rho_{i,-j} + \rho_{-j,i} + \rho_{-i,-j} + \rho_{-j,-i} - (\rho_{i,j} + \rho_{i,-j} + \rho_{-i,j} + \rho_{-i,-j}) (\delta_{ij} + \delta_{oj} + \delta_{oi} - \delta_{ci} \delta_{oj})] I_{ij} \quad (67)$$

where the δ_{ij} are Kronecker deltas and ρ_{00} is the reflectance of the target.

It should be noted that only $(N-1)(N+5)/8$ integrations need be performed for an N by N grid.

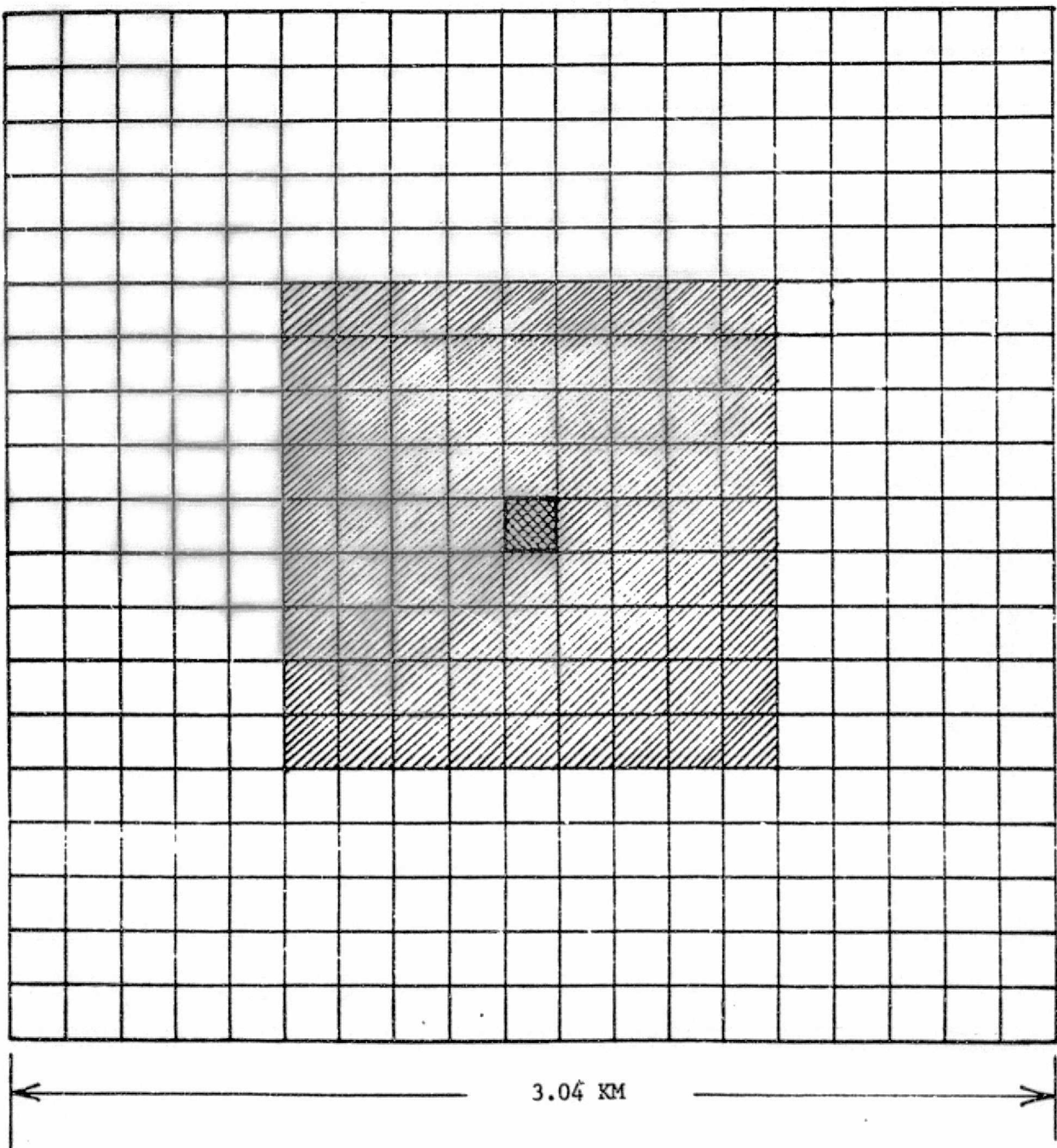
We considered three atmospheric states characterized by visual ranges of 3 km, 10 km, and 40 km corresponding to very hazy, hazy, and relatively clear conditions respectively. The wavelengths chosen are those corresponding to the centers of the four ERTS channels, i.e., 0.55 μm , 0.65 μm , 0.75 μm , and 0.95 μm . It is assumed that the sensor is looking in the nadir direction from space at fields in the midwestern part of the United States on 24 June 1975. The atmosphere is uniform over the extended area and contains no absorbing particulates. We chose, for computational convenience, a 19 by 19 grid, i.e., 361 square fields, each 2 pixels or 160 m on a side. Thus, each field contains 4 resolution elements. Configuration 1 is depicted in Fig. 41. We consider a target in the center of the grid and a variable background. A new reflectance is imagined as moving in from the right, column-by-column until it completely overtakes the original background. Configuration 2 is depicted in Fig. 42. Here we consider a new background which is expanding outward from the target field, ring-by-ring until the original background is completely overtaken. Any configuration is possible but we shall consider these two examples.

First, we analyze a black target and a variable black-white background. Figure 43 illustrates the variation in the ratio of the surface path radiance to the pure atmospheric path radiance as a white cover advances over the scene. It is assumed, however, that the target is always black. It should be noted that there is a very large increase only after the white cover passes the target and then approaches an asymptotic value. Figure 44 illustrates the spectral variation of the same ratio. It is almost linear with



FIELD CONFIGURATION 1

FIGURE 41



FIELD CONFIGURATION 2

FIGURE 42

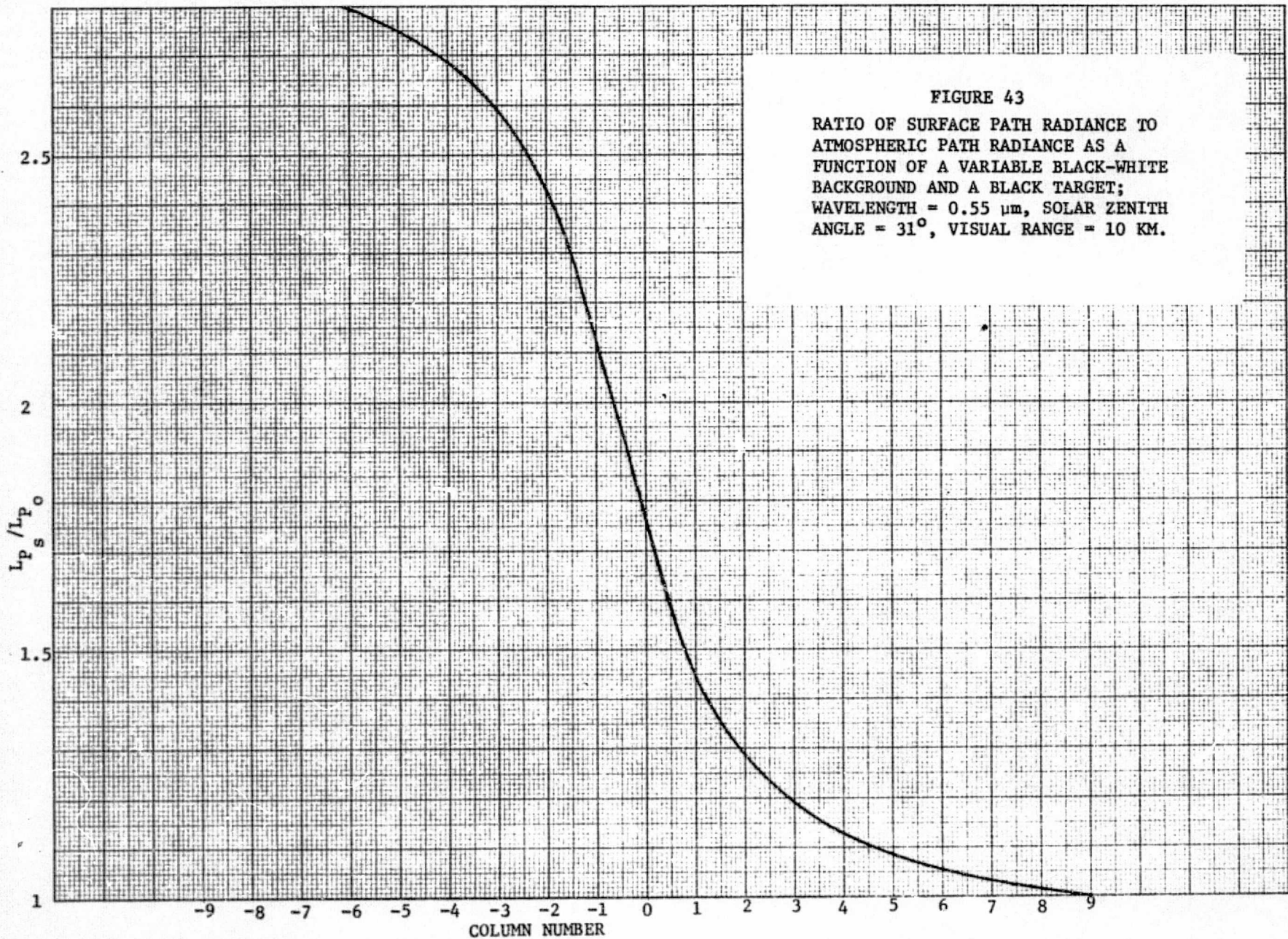
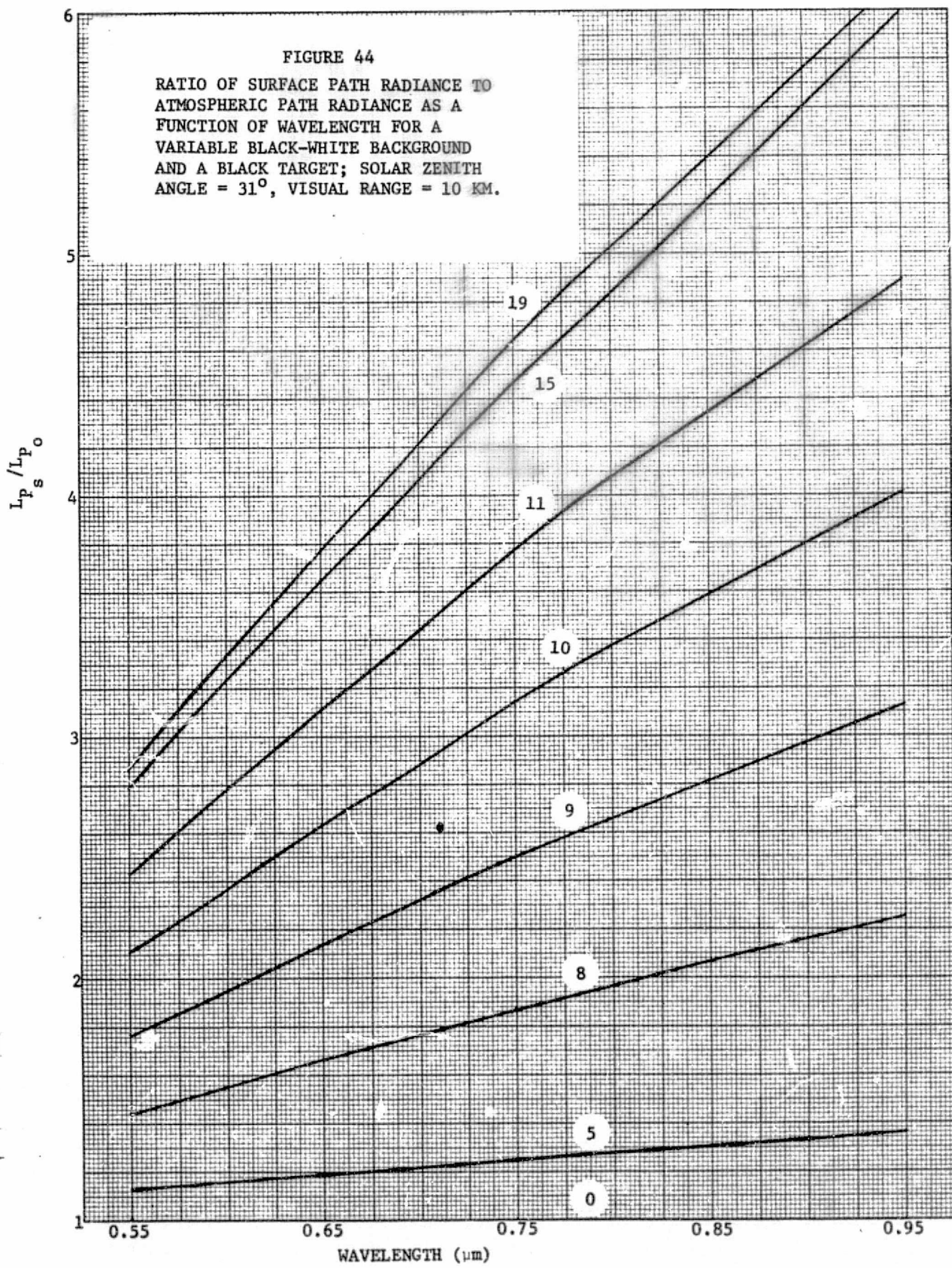


FIGURE 43

RATIO OF SURFACE PATH RADIANCE TO
ATMOSPHERIC PATH RADIANCE AS A
FUNCTION OF A VARIABLE BLACK-WHITE
BACKGROUND AND A BLACK TARGET;
WAVELENGTH = $0.55 \mu\text{m}$, SOLAR ZENITH
ANGLE = 31° , VISUAL RANGE = 10 KM.



wavelength but the slope of the curves is quite different depending on the amount of white background.

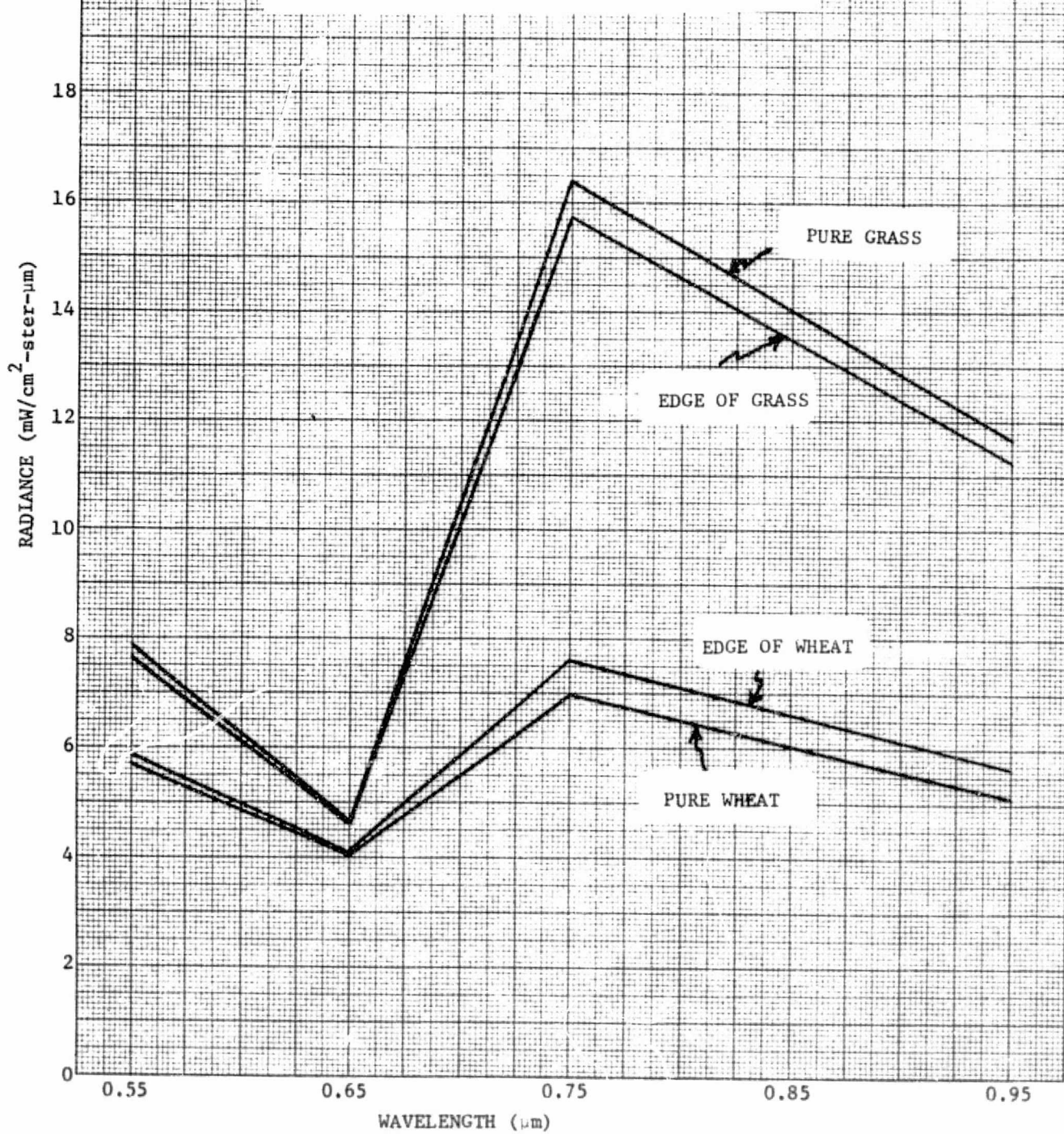
Second, we shall consider the same configuration only this time we have a variable wheat-grass background where reflectances for healthy, mature wheat and grass were used. This would simulate a scan across a wheat-grass boundary. Figure 45 illustrates the effect. Pure wheat means that the entire scene is wheat. Edge of wheat means that we are looking at a wheat field target with one half of the scene covered by wheat and the other half by grass. As we cross over the boundary to the grass one can see that a large change occurs due to the dominance of the radiance from the target itself. Then as we progress further into the grass region the radiance changes slightly.

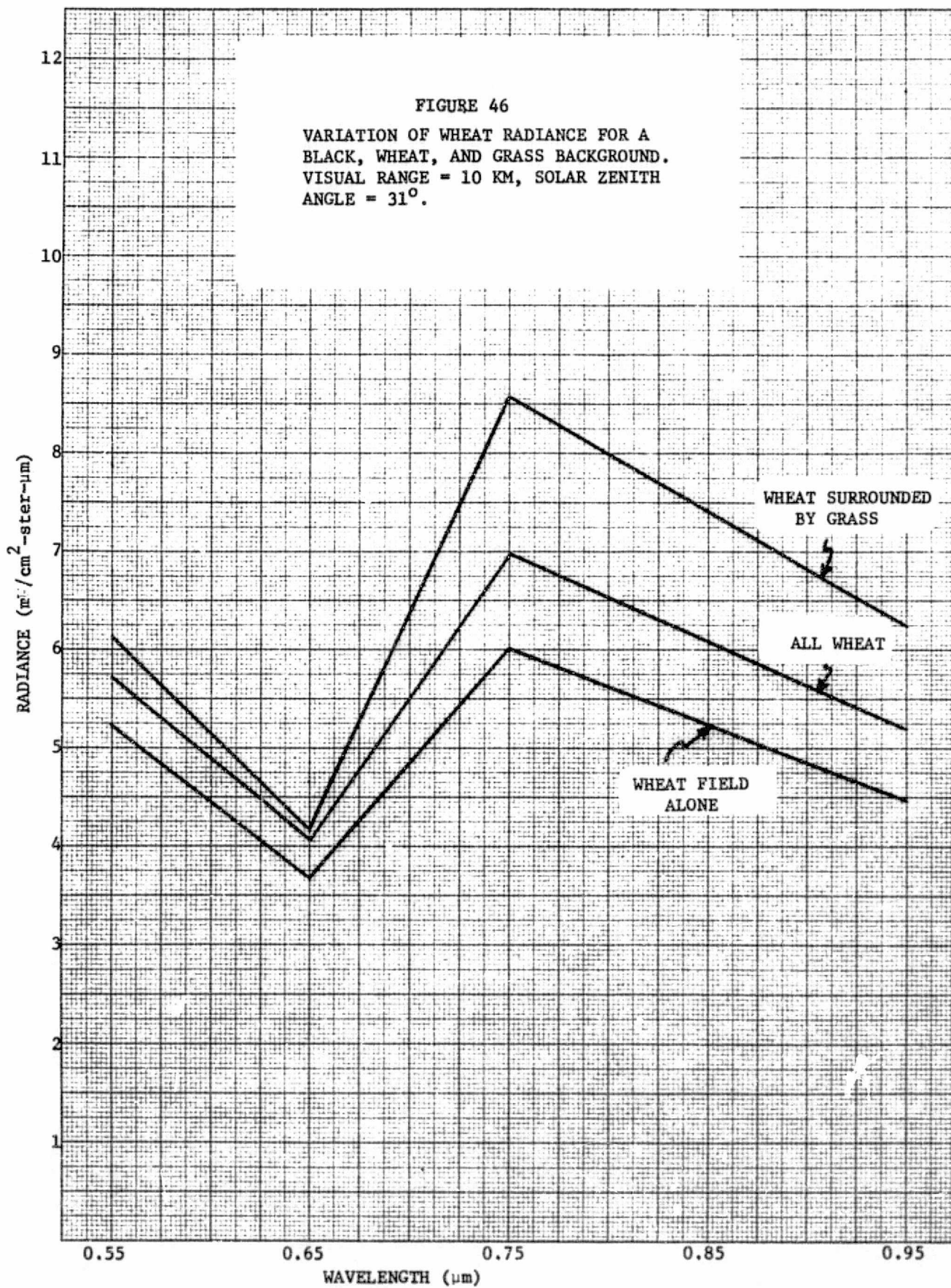
Third, we consider a wheat target being surrounded by rings of grass. Figure 46 depicts the variation in the spectral radiance in this situation. We have a wheat field surrounded by a black background. Then we have an all wheat scene which clearly illustrates the magnitude of the background interference. It should be noted that this represents about 90% of the radiance possible, i.e., an infinite plane of wheat would raise the values by 10%. The third curve represents a wheat field surrounded by a total grass scene. The percentage change is significant but this will have to be translated into actual signatures before classification accuracies can be determined.

Fourth, it is perhaps more useful to consider the per cent change in radiance from one configuration to another. Let us imagine a wheat target surrounded by a grass background. Figure 47 shows that there is about a 25% change in channel 3. Now, if we have a wheat target and the next ring of elements (fields) is also wheat with the rest of the surface being grass, then the change is only ~17% in channel 3. It continues to decrease, of course, as we add more wheat to the area surrounding the target.

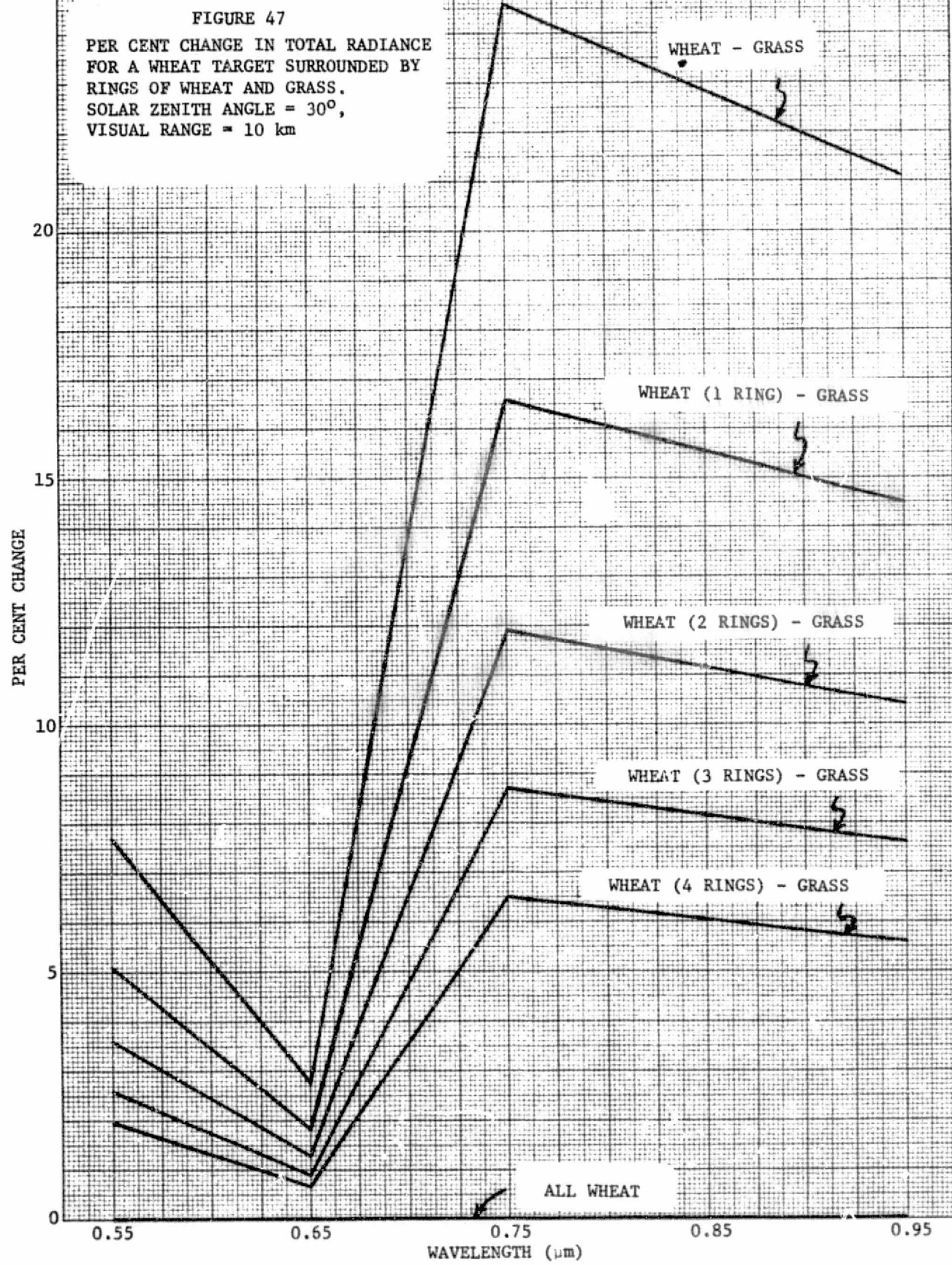
FIGURE 45

TOTAL SPECTRAL RADIANCE AS A FUNCTION
OF A VARIABLE WHEAT-GRASS BACKGROUND
FOR A WHEAT TARGET AND A GRASS TARGET,
VISUAL RANGE = 10 KM, SOLAR ZENITH
ANGLE = 31°.





25



How much does the per cent change vary as a function of sun angle? This is illustrated in Fig. 48 for four solar zenith angles. There seems to be a maximum effect in the range $\theta_0 \sim 30^\circ - 60^\circ$, which is also the range of sun angles for which most data are collected.

In order to see the simultaneous change in total radiance and surface path radiance we can plot one versus the other for all four channels. This is depicted in Fig. 49. We go from an all wheat area to a wheat field surrounded by grass. The length of the displacement depends upon visual range; the greater the visual range, the smaller the line segment. Thus, for no atmosphere the line segment is zero.

The greater the reflectance of the background relative to the target, the greater is the change in total radiance. Thus, for a dark target such as soil or loam the change can be quite large. This is shown in Fig. 50 for soil being surrounded by various amounts of grass. A corresponding L_T vs. L_{P_s} plot is depicted in Fig. 51.

In order to see the per cent change for various materials we can analyze wheat targets with grass backgrounds, soil targets with grass backgrounds, and diseased wheat targets with a wheat background. This dramatic effect is illustrated in Fig. 52.

What is the effect of different atmospheric states on the radiance values? In Fig. 53 we consider soil targets with various backgrounds. As is to be expected, the change increases with increasing turbidity, or decreasing visual range.

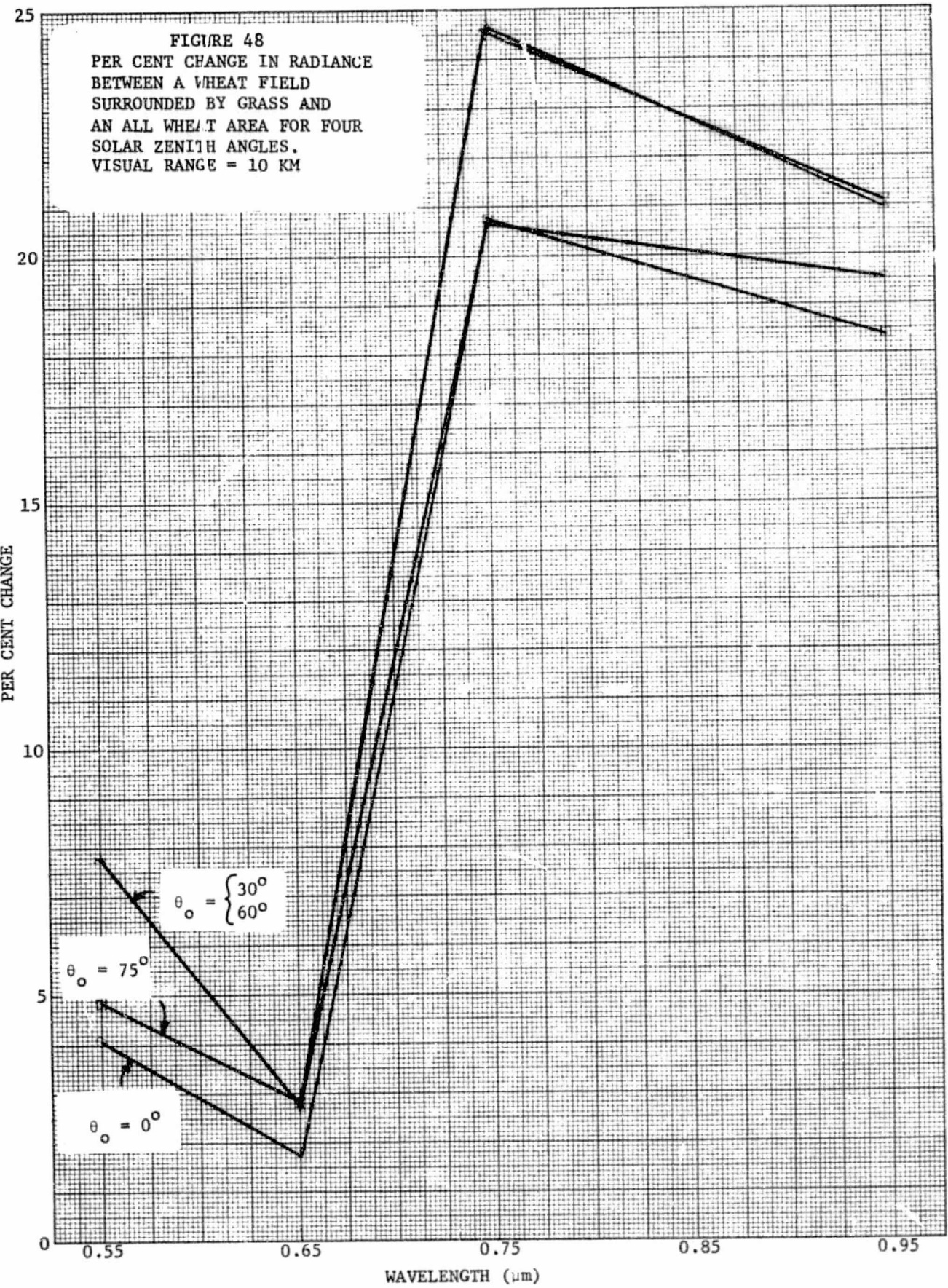
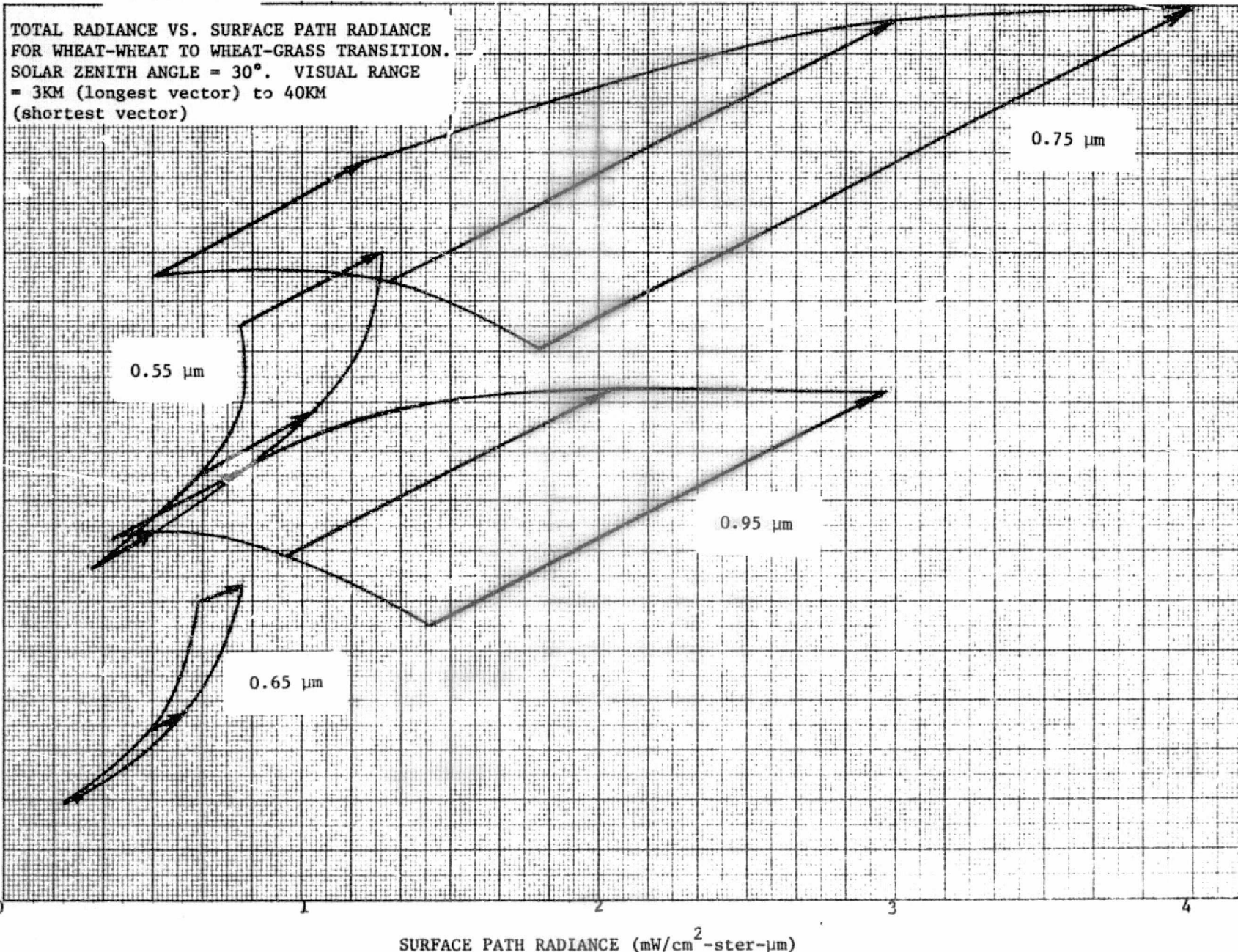
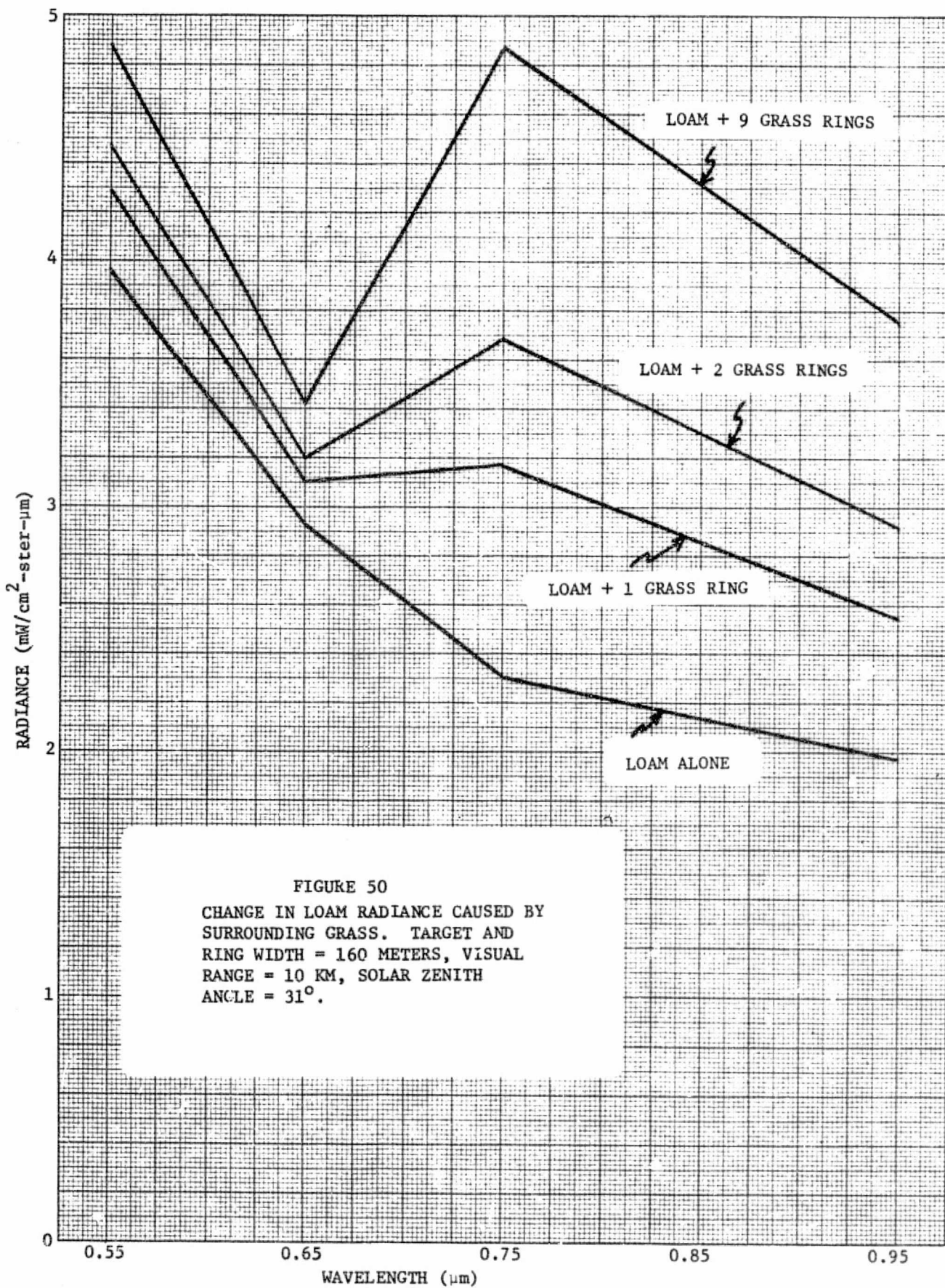
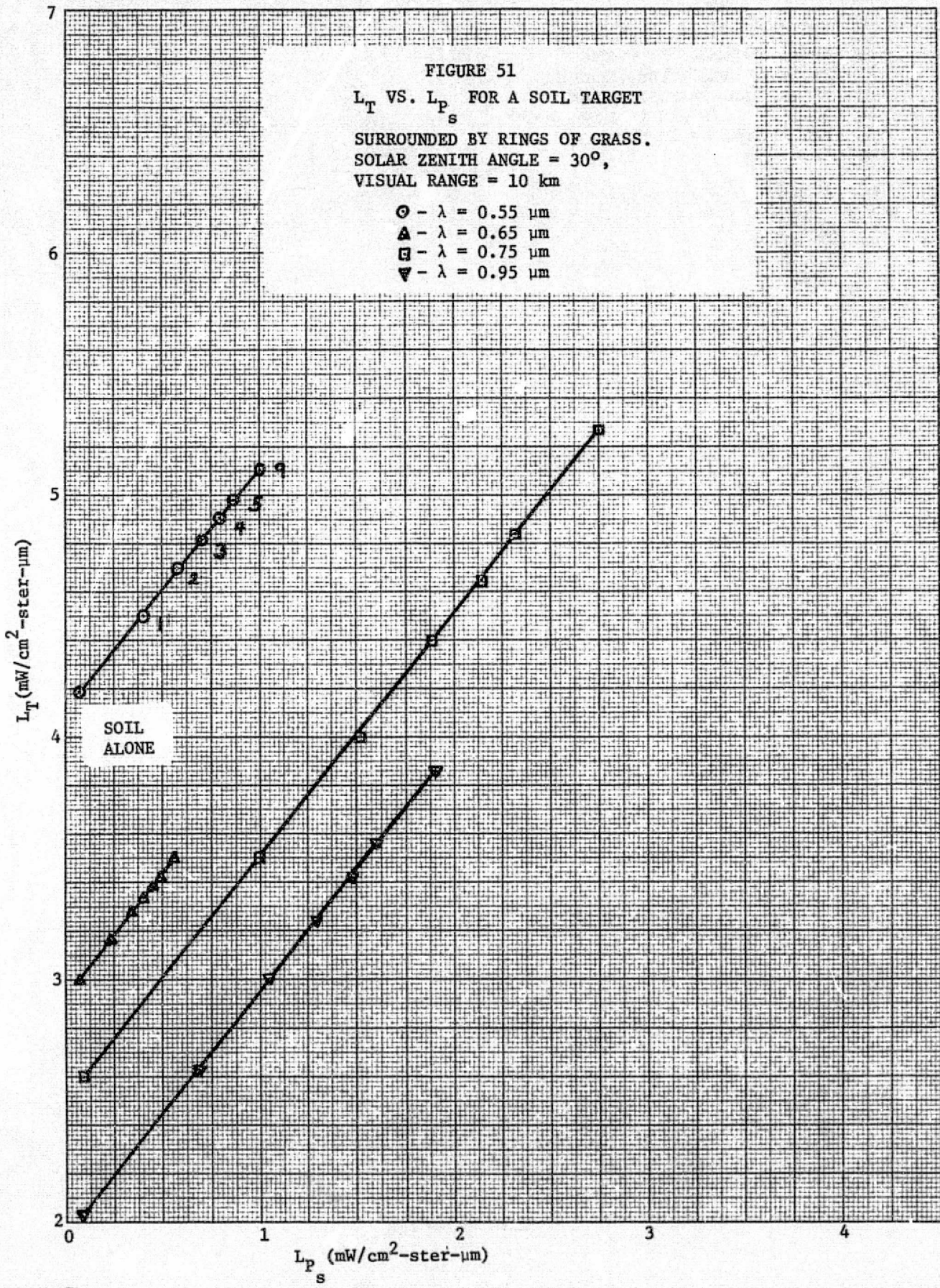
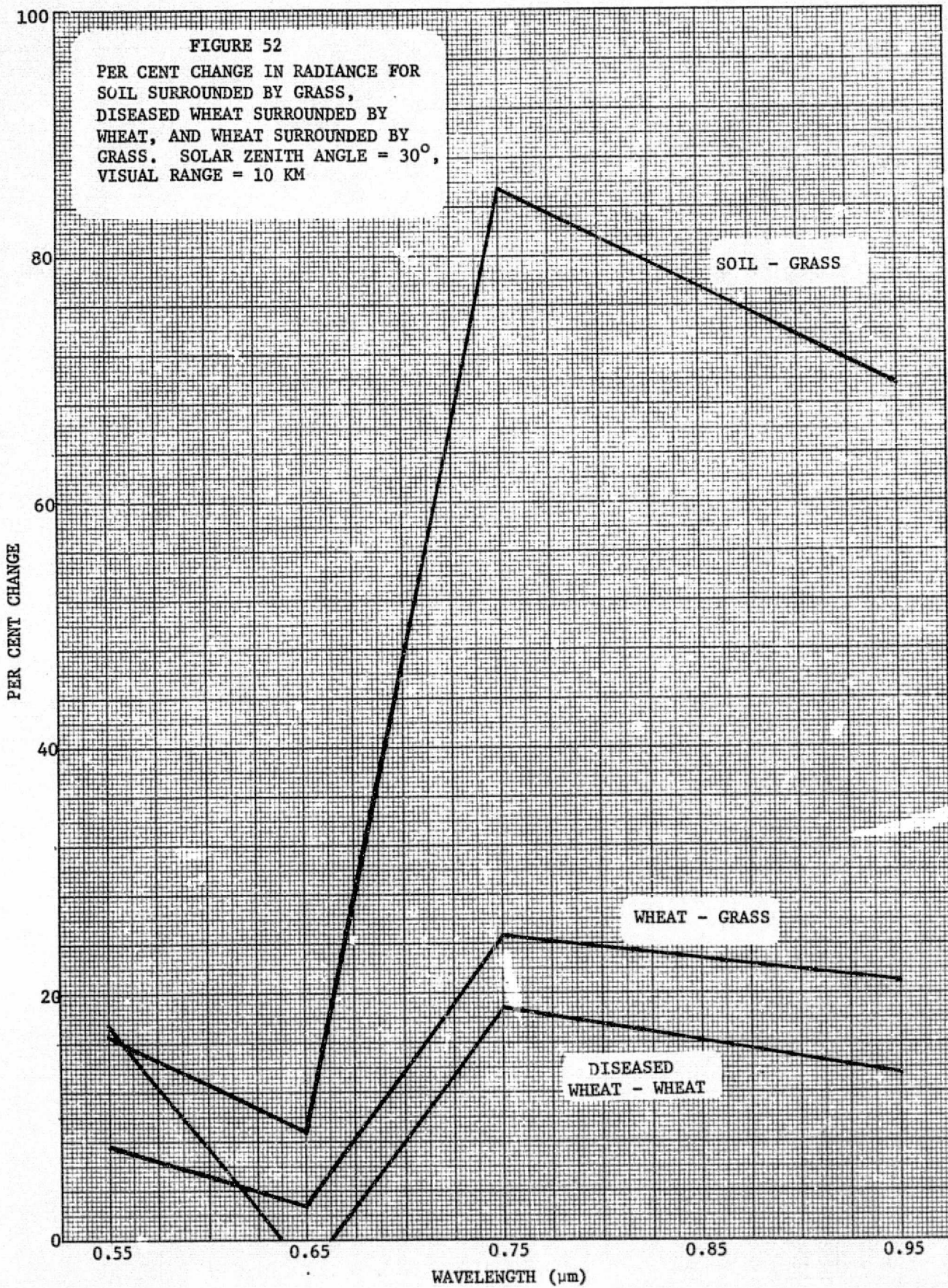


FIGURE 49









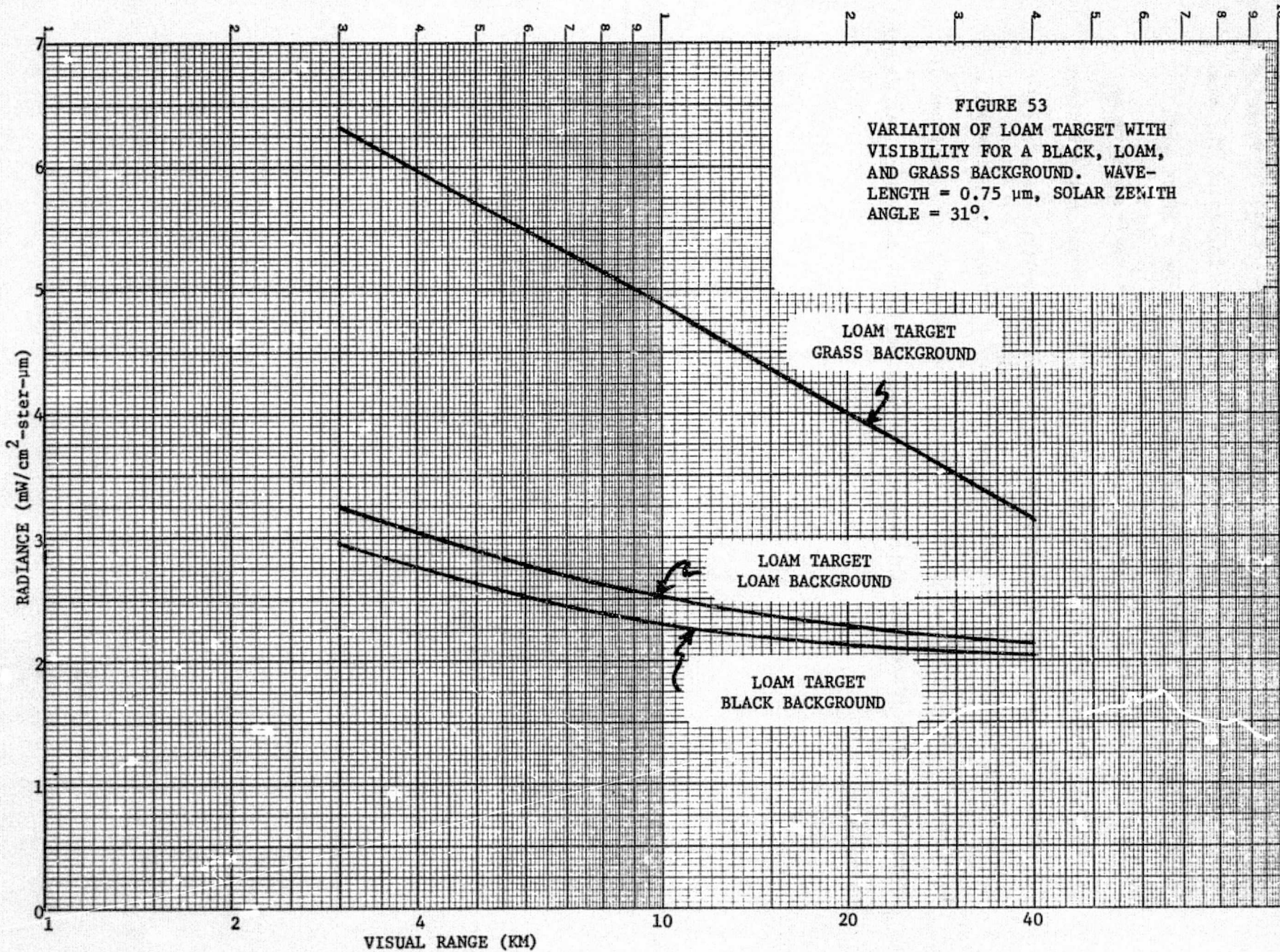
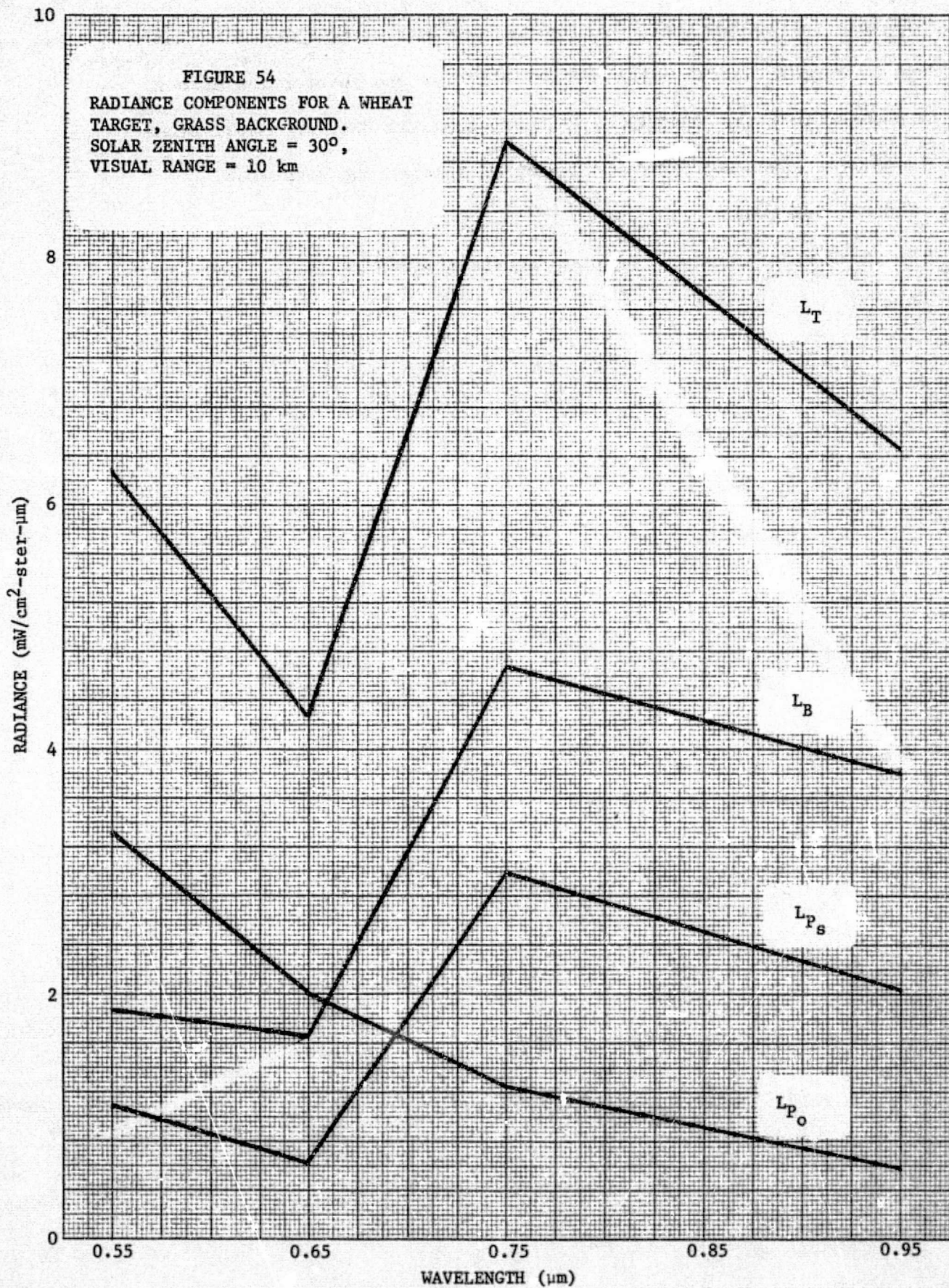


FIGURE 53

VARIATION OF LOAM TARGET WITH
VISIBILITY FOR A BLACK, LOAM,
AND GRASS BACKGROUND. WAVE-
LENGTH = $0.75 \mu\text{m}$, SOLAR ZENITH
ANGLE = 31° .

Finally, we should consider the various components which make up the total radiance. Figure 54 illustrates the spectral variation of the beam radiance L_B , the pure atmospheric path radiance L_{P_o} , the surface path radiance L_{P_s} , and the total radiance L_T . Although the dominant term is the beam radiance, the surface path radiance is by no means insignificant. For shorter wavelengths or smaller visual ranges the multiply scattered surface path radiance can be expected to increase. Thus, the background can certainly alter the total radiance. The pure atmospheric path radiance is independent of surface conditions and decreases monotonically with increasing wavelength.



INTERACTION CORRECTION ALGORITHM

In this section we shall develop mathematical techniques which can be used to correct actual multispectral data for the interaction effect. It is assumed that the atmosphere is homogeneous in the horizontal plane but the flat surface may have any degree of spatial inhomogeneity.

5.1 GENERAL SURFACES

We shall first consider general, non-Lambertian surfaces. The general equation is

$$L(\vec{r}, \hat{\Omega}) = L_o(\vec{r}_s, \hat{\Omega})T(\vec{r}, \hat{\Omega}) + L_{P_o}(\vec{r}, \hat{\Omega}) + L_{P_s}(\vec{r}, \hat{\Omega}) \quad (68)$$

For homogeneous atmospheres

$$T(\vec{r}, \hat{\Omega}) = T(z, \hat{\Omega}) \quad (69)$$

$$L_{P_o}(\vec{r}, \hat{\Omega}) = L_{P_o}(z, \hat{\Omega}) \quad (70)$$

Thus,

$$L(\vec{r}_p, z, \hat{\Omega}) = L_o(\vec{r}_s, \hat{\Omega})T(z, \hat{\Omega}) + L_{P_o}(z, \hat{\Omega}) + L_{P_s}(\vec{r}_p, z, \hat{\Omega}) \quad (71)$$

where the vectors \vec{r}_p and \vec{r}_s are illustrated in Fig. (55). Now, the singly-scattered path radiance is given by

$$L_{P_s}(\vec{r}_p, z, \hat{\Omega}) = \int \int \hat{n} \cdot \hat{\Omega}_o G(\vec{r}_p, z, \hat{\Omega}; \vec{r}_o, \hat{\Omega}_o) L_o(\vec{r}_o, \hat{\Omega}_o) d\vec{r}_o d\hat{\Omega}_o \quad (72)$$

Taking the Fourier transform of Eq. (71) leads to the following equation:

$$\begin{aligned} \bar{L}(\vec{k}, z, \hat{\Omega}) &= T(z, \hat{\Omega}) e^{-ik \cdot \vec{r}} \bar{L}_o(\vec{k}, \hat{\Omega}) \\ &+ (2\pi)^2 \delta(\vec{k}) L_{P_o}(z, \hat{\Omega}) + \bar{L}_{P_s}(\vec{k}, z, \hat{\Omega}) \end{aligned} \quad (73)$$

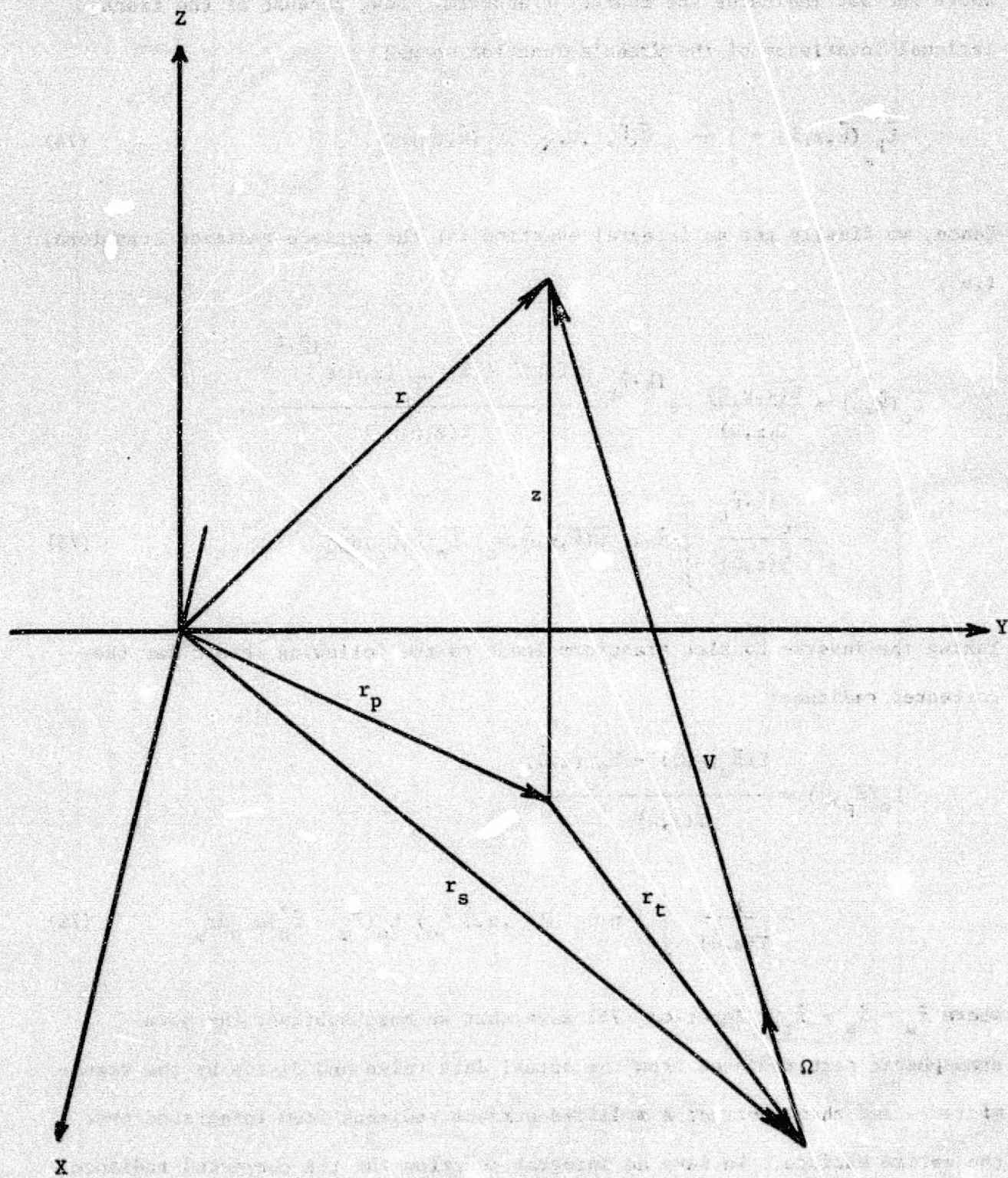


FIGURE 55. GEOMETRY FOR CORRECTION ALGORITHM.
Sensor Location at r .
Ground Observation Point at r_s .

where the bar indicates the Fourier transform. Now, because of the translational invariance of the Green's function we get

$$\bar{L}_P_s(\vec{k}, z, \hat{\Omega}) = \int \hat{n} \cdot \hat{\Omega}_o \bar{G}(\vec{k}, z, \hat{\Omega}, \hat{\Omega}_o) \bar{L}_o(\vec{k}, \hat{\Omega}_o) d\hat{\Omega}_o \quad (74)$$

Hence, we finally get an integral equation for the surface radiance transform, i.e.,

$$\begin{aligned} \bar{L}_o(\vec{k}, \hat{\Omega}) &= \frac{\bar{L}(\vec{k}, z, \hat{\Omega})}{T(z, \hat{\Omega})} e^{i\vec{k} \cdot \vec{r}_t} - \frac{(2\pi)^2 \delta(\vec{k}) L_P_o(z, \hat{\Omega}) e^{i\vec{k} \cdot \vec{r}_t}}{T(z, \hat{\Omega})} \\ &- \frac{e^{i\vec{k} \cdot \vec{r}_t}}{T(z, \hat{\Omega})} \int \hat{n} \cdot \hat{\Omega}_o \bar{G}(\vec{k}, z, \hat{\Omega}, \hat{\Omega}_o) \bar{L}_o(\vec{k}, \hat{\Omega}_o) d\hat{\Omega}_o \end{aligned} \quad (75)$$

Taking the inverse Fourier transform leads to the following result for the corrected radiance:

$$\begin{aligned} L_o(\vec{r}_p, \hat{\Omega}) &= \frac{L(\vec{r}_u, z, \hat{\Omega}) - L_P_o(z, \hat{\Omega})}{T(z, \hat{\Omega})} \\ &- \frac{1}{T(z, \hat{\Omega})} \int \int \hat{n} \cdot \hat{\Omega}_o G(\vec{r}_u, z, \hat{\Omega}, \hat{\Omega}_o) L_o(\vec{r}_u - \vec{r}'_u) d\hat{\Omega}_o d\vec{r}'_u \end{aligned} \quad (76)$$

where $\vec{r}_u = \vec{r}_p - \vec{r}_t$. Equation (76) says that we must subtract the pure atmospheric path radiance from the actual data value and divide by the transmittance and then subtract a modified surface radiance from integrated over the entire surface. We have an integral equation for the corrected radiance $L(\vec{r}, \hat{\Omega})$ which can be solved in various ways. In particular, if we use the

single-scattering Green's function in Eq. (76) then a definite (but complicated) analytical result can be found for the corrected radiance.

5.2 LAMBERTIAN SURFACES

If we assume a perfectly diffuse (Lambertian) surface considerable simplification occurs in the mathematical method. Equation (76) then becomes

$$\begin{aligned} \bar{L}_o(\vec{k}) &= \frac{\bar{L}(\vec{k}, z, \hat{\Omega})}{T(z, \hat{\Omega})} e^{i\vec{k} \cdot \vec{r}_t} - \frac{(2\pi)^2 \delta(\vec{k}) L_p(z, \hat{\Omega}) e^{i\vec{k} \cdot \vec{r}_t}}{T(z, \hat{\Omega})} \\ &- \frac{e^{i\vec{k} \cdot \vec{r}_t} \bar{g}(\vec{k}, z) \bar{L}_o(\vec{k})}{T(z, \hat{\Omega})} \end{aligned} \quad (77)$$

where $\bar{g}(\vec{k}, z)$ is the transform of an isotropic Green's function integrated over a hemisphere. Equation (77) can therefore be solved for $\bar{L}_o(\vec{k})$, i.e.,

$$\bar{L}_o(\vec{k}) = \frac{\left[\bar{L}(\vec{k}, z, \hat{\Omega}) - (2\pi)^2 \delta(\vec{k}) L_p(z, \hat{\Omega}) \right] e^{i\vec{k} \cdot \vec{r}_t}}{T(z, \hat{\Omega}) + \bar{g}(\vec{k}, z) e^{i\vec{k} \cdot \vec{r}_t}} \quad (78)$$

Thus, knowing the surface pattern and the optical thickness or visibility conditions one can find the transmittance, pure atmospheric path radiance, and the Green's function. Inverting the above transform then gives us the surface radiance free of the interaction effects. The general algorithm is illustrated in Fig. (56).

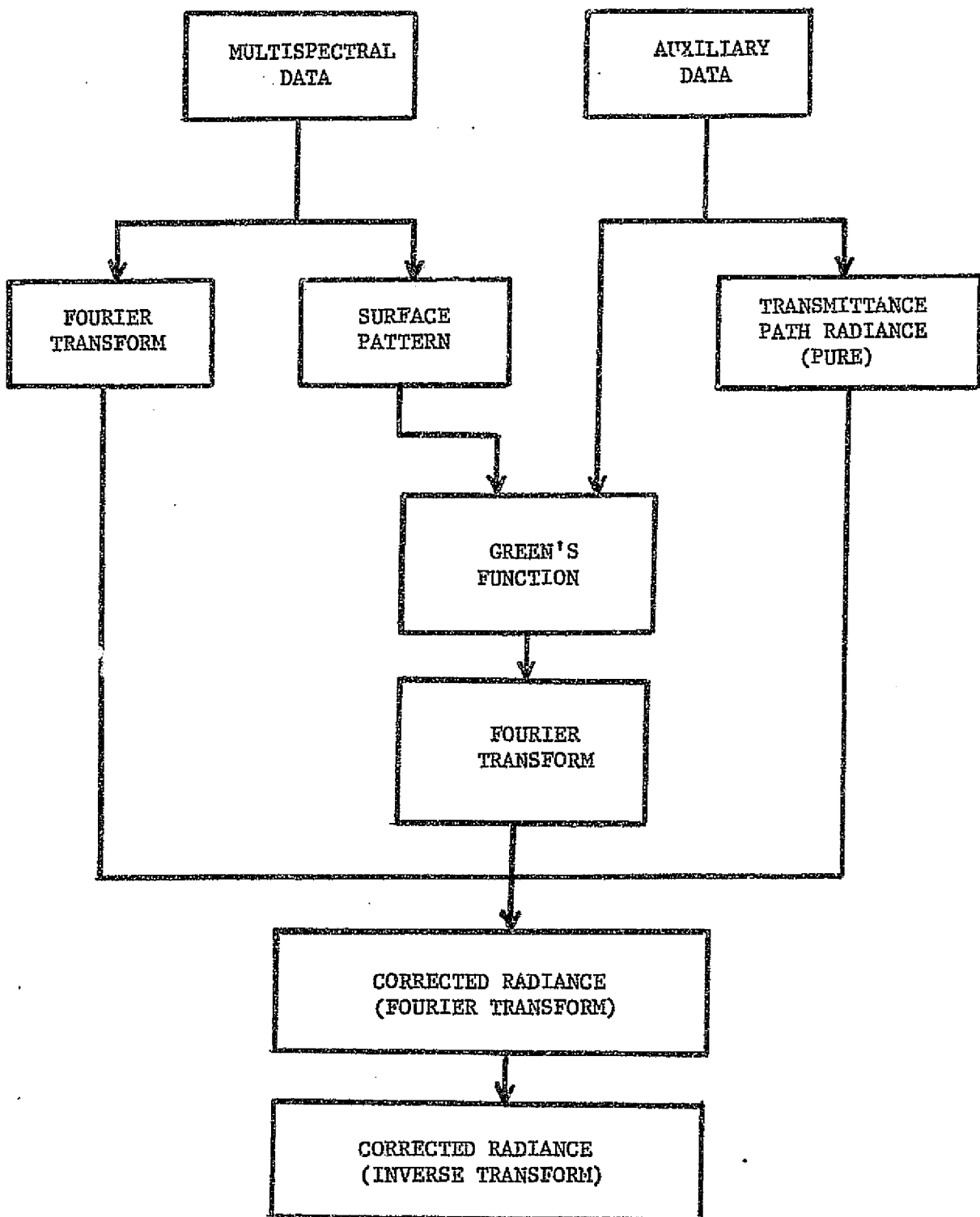


FIGURE 56. ALGORITHM FOR CORRECTION OF MULTISPECTRAL DATA
FOR ATMOSPHERIC INTERACTION EFFECTS

CONCLUSIONS AND RECOMMENDATIONS

In the current analysis we have analyzed two atmospheric effects, the spatial variations in the atmosphere and the target-background interaction. Of all possible atmospheric variations these will cause the greatest change in classification accuracy.

The relationship between the various radiometric quantities which we considered in some detail is useful for the determination of atmospheric and environmental parameters which, in turn, are used in an atmospheric correction algorithm. Thus, a measurement of irradiance or sky radiance along with transmittance will allow certain parameters to be estimated. For variable atmospheres it is necessary to perform several measurements at selected points in a scene. As we have seen in the simulation analysis, the greater the number of auxiliary measurement sites the better is the agreement between actual and calculated radiances.

In the classification problem we showed that rather severe atmospheric optical thickness gradients are needed in order to realize a significant change in the per cent classification accuracy. It should be realized however, that no correlation was assumed between classes and hence the soybean and corn fields were statistically independent. Also, no absorption was included in the simulations made. If remote sensing data are collected over a large area or near an urban complex then there could very well be large spatial changes in the absorptive part of the optical thickness. At first, it seems that strong gradients in the optical thickness surface are unrealistic, but that is not the case if absorption is included. Also, it

was assumed throughout that there was no interference arising between fields as a result of atmospheric scattering. As was learned in the next section such a neglect can affect classification accuracy. Hence, we conclude that if multispectral data are collected over small, homogeneous regions away from sources of pollution and in very clear atmospheres then the classification accuracy is not greatly affected by atmospheric changes. It should be realized, however, that these are severe restrictions. A not inconsiderable amount of remote sensing data collection is performed under adverse weather conditions. Also, it is becoming increasingly more difficult to find extended areas which are completely free of aerosol absorption. Thus, in order to extend the capability of remote sensing to a wider range of atmospheric conditions it seems appropriate that the atmospheric correction procedures outlined in Section 1 be implemented on actual data.

Only in recent years has the effect of surface albedo been realized to be of importance in multispectral data analysis. It has generally been assumed that spectral signatures are essentially determined by the target material. Background albedo was recognized as being of some importance in the estimation of the magnitude of path radiance but no real quantitative analysis was done, especially for various surface patterns of fields. As a result of the work done in the current study we are now able to analyze the effect of varying target-background geometry on the spectral radiance characteristics of a target material. We can consider fields of any size and simulate any complex pattern. We have found that the background changes the irradiance on the target by a very small amount, much less than the effect of background on path radiance. The current analysis makes use of few approximations. The integration is done numerically with realistic

anisotropic phase functions and for vertical changes in the atmosphere. This means that, as far as the surface path radiance is concerned, we have an exact formulation for a realistic, vertically inhomogeneous atmosphere.

The results of the calculations clearly indicate a sizable change in the radiance from targets of standard materials such as wheat, soil, and grass when various background materials are present. It should also be pointed out that the effects presented here are in a sense minimal since we cannot integrate over an infinite surface. They do represent, however, most of the effect due to single scattering, i.e., the effects are perhaps fifty to ninety per cent of the full value. Most of the simulations considered were for a 10 km visual range but it is apparent from the graphs that even for high visibilities the effect can be important. Hence, we conclude that if remote sensing is performed without taking into consideration the geometry and type of background elements then a false determination of the signature may result. This is especially true for highly variable contiguous fields.

For the variable atmospheric problem we recommend that additional variable surfaces be considered, i.e., those which portray a larger amount of absorption. Also, non-linear optical thickness gradients in the horizontal plane should be used which are more indicative of variable atmospheric conditions near urban areas. In addition, the atmospheric correction algorithm outlined in Section 2 should be used on real data with known atmospheric variability.

Although much has been learned in the target-background interaction problem there are a number of things which should be done to improve the accuracy. First, we used mean values of reflectance for the various fields. Most of these data, however are for the leaves of plants rather than for the crops themselves. Thus, the current model should be interfaced with a reflectance model for the materials used. The mathematical procedures developed herein are versatile enough to include the bidirectional reflectance of any material. The interesting goniometric properties associated with some crops could then induce changes in the present results, which could be either larger or smaller than are indicated by assuming Lambertian surfaces.

It would be interesting to include the interaction effect with the variable atmosphere and to see the total change in classification accuracy. In any case, for a uniform or non-uniform atmosphere the classification analysis procedures should be carried out for a complex pattern of interacting fields. This simulation can be done with the present analytical techniques.

Finally, the inverse problem should be analyzed, i.e., the implementation of the interaction correction algorithm outlined in Section 5.

Including all of these effects, i.e., performing correction analysis followed by classification procedures should result in a significantly improved classification accuracy of multispectral data.

REFERENCES

1. H. Koschmieder, Beitr. Phys. freien Atm., Vol. 12, 19, 24 pp. 33-53, 171-181
2. R. E. Turner, Radiative Transfer in Real Atmospheres, Report No. 190100-24-T, Environmental Research Institute of Michigan, Ann Arbor, 1974.
3. L. Elterman, Vertical-Attenuation Model with Eight Surface Meteorological Ranges 2 to 13 Kilometers, Report No. AFCRL-70-0200, Air Force Cambridge Research Laboratories, Office of Aerospace Research, Bedford, Mass., 1970.
4. D. Deirmendjian, Electromagnetic Scattering on Spherical Polydispersions, Elsevier, New York, 1969, p. 78.
5. R. E. Turner, W. A. Malila, R. F. Nalepka, F. J. Thomson, Influence of the Atmosphere on Remotely Sensed Data, Proceedings of Society of Photo-Optical Instrumentation Engineers, 1975.
6. R.E. Turner & M.M. Spencer, Atmospheric Model for Correction of Spacecraft Data, Proceedings of the 8th International Conference on Remote Sensing of Environment, Center for Remote Sensing Information & Analysis, Willow Run Laboratories of the Institute of Science and Technology, The University of Michigan, 1972.
7. R. Horvath, M. Spencer, and R. Turner, Atmospheric Correction and Simulation of Space Acquired Remote Sensor Data: 0.4 - 1.0 μm Spectral Range, Report No. 10657-5-F, Willow Run Laboratories of the Institute of Science and Technology, The University of Michigan, 1972.
8. R.F. Nalepka, H.M. Horwitz, N.S. Thomson, Report No. 31650-30-T, Willow Run Laboratories, The University of Michigan, Ann Arbor, 1971.
9. K.M. Case and P.F. Zweifel, The Linear Transport Theory, Addison - Wesley Publishing Co., 1967.